Ab initio description of skyrmion detection with tunnel junctions

Ab initio Beschreibung der Skyrmion-Detektion mit Tunnelkontakten

DISSERTATION

submitted for the degree of

Doctor rerum naturalium
Doktor der Naturwissenschaften

by
Jonas Friedrich Schäfer-Richarz

Supervisor: Prof. Dr. Christian Heiliger
Institut für Theoretische Physik

JUSTUS-LIEBIG-
UNIVERSITÄT
GIESSEN

Justus-Liebig-Universität Gießen

Gießen, December 2025

Abstract

In this work, I use the Korringa–Kohn–Rostoker (KKR) method to analyze the possibility of using magnetic tunnel junctions (MTJ) to detect magnetic skyrmions. Usually, these junctions require a magnetic reference layer and then show the well-known tunneling magnetoresistance effect (TMR). However, under the right conditions, the non-collinear magnetic structure of skyrmions can lead to a significant increase in conductance through a tunnel junction even without a magnetic reference layer. While a large part of the overall change in conductance can be attributed to the disturbance of quantum well states (QWS) in the iron monolayer hosting the skyrmion, the majority of the effect, including the increase, is due to the scattering of electronic states from the lead at the skyrmion. This is an interesting situation which demonstrates that scattering does not necessarily reduce conductance, but can also increase conductance drastically if coherent transport is blocked by the symmetry of the electronic states in the ferromagnetic case. The combination of vanadium as lead material with a MgO barrier was identified as a material combination where coherent transport in the collinear ferromagnetic base structure is suppressed, but can be enhanced by scattering of electronic states.

Beyond that, I show that the presence of a skyrmion in a tunnel barrier not only alters the conductance but also changes the Seebeck coefficient. It turns out that the absolute value of the Seebeck coefficient tends to be reduced by the skyrmion. Since antiferromagnetic skyrmions offer several advantages over ferromagnetic skyrmions but are much harder to handle and detect than their ferromagnetic counterparts, I investigate how useful the proposed effect might be for the detection of antiferromagnetic skyrmions. The results indicate that the electronic transport is, in principle, also sensitive to antiferromagnetic non-collinear structures. Finally, I take a brief excursion into the topic of the TMR effect, which requires a magnetic reference layer but can potentially be used to distinguish between different types of non-collinear structures by doing multiple measurements with low spatial resolution.

Zusammenfassung

In dieser Arbeit untersuche ich mithilfe der Korringa–Kohn–Rostoker (KKR) Methode, inwiefern sich magnetische Tunnelbarrieren zur Detektion von magnetischen Skyrmionen eignen. Normalerweise benötigen solche Tunnelbarrieren eine zweite magnetische Referenzschicht und weisen dann den wohlbekannten magnetischen Tunnelwiderstand (TMR) auf. Allerdings kann unter geeigneten Bedingungen die nicht-kollineare magnetische Struktur von Skyrmionen, auch ohne magnetische Referenzschicht, zu einer signifikanten Vergrößerung der Leitfähigkeit durch die Tunnelbarriere führen. Ein großer Teil des Gesamteffekts lässt sich auf die Störung von Quantentopfzuständen in der Eisen-Monolage zurückführen, in der sich das Skyrmion befindet. Der Hauptteil des Effekts, einschließlich des überraschenden Anstiegs der Leitfähigkeit, wird jedoch durch die Streuung von Elektronen an der Skyrmionstruktur verursacht. Dies ist eine sehr interessante Situation, die aufzeigt, dass Streuung nicht notwendigerweise die Leitfähigkeit verringert, sondern sie auch drastisch erhöhen kann, sofern kohärenter elektrischer Transport im ferromagnetischen Fall durch die Symmetrie der elektronischen Zustände blockiert wird. Insbesondere kann die Kombination von Vanadium als Material für die elektrische Zuleitung zusammen mit einer MgO-Barriere als Materialkombination identifiziert werden, bei der kohärenter elektrischer Transport in der kollinearen ferromagnetischen Struktur unterdrückt ist, aber durch Streuung der elektronischen Zustände erhöht werden kann. Darüber hinaus zeige ich, dass das Vorhandensein eines Skyrmions in einer Tunnelbarriere nicht nur den elektrischen Widerstand, sondern auch den Seebeck-Koeffizienten verändern kann. Es zeigt sich, dass der absolute Wert des Seebeck-Koeffizienten dazu tendiert, kleiner zu werden, wenn ein Skyrmion anwesend ist. Weil antiferromagnetische Skyrmionen eine Reihe von wichtigen Vorteilen gegenüber ferromagnetischen Skyrmionen aufweisen, aber wesentlich schwieriger zu handhaben und zu detektieren sind, untersuche ich ebenfalls, inwiefern sich der vorhergesagte Effekt zur Detektion von antiferomagnetischen Skyrmionen eignen könnte. Das Ergebnis der Analyse lässt darauf schließen, dass der elektrische Transport durch Tunnelbarrieren grundsätzlich auch sensitiv auf antiferromagnetische nicht-kollineare Strukturen reagieren kann. Schließlich zeige ich, dass der magnetische Tunnelwiderstand mit magnetischer Referenzschicht grundsätzlich nutzbar sein könnte, um verschiedene Typen von nicht-kollinearen Strukturen zu unterscheiden, wobei zwar mehrere Messungen nötig sind, aber dafür keine hohe räumliche Auflösung erforderlich ist.

Contents

Chapter 1

Introduction

Since the development of magnetoresistance based read heads [1] for hard drives, it has become clear that spin based electronics or spintronics [2] provides many opportunities for new technologies. Spintronics is not only about the additional degree of freedom, but also introduces entirely new concepts and possibilities.

One large research field within spintronics is skyrmionics [3], which focuses on using magnetic skyrmions [4, 5, 6, 7] as information carriers. Skyrmions are topologically stabilized magnetic swirls that can be created, moved, destroyed, and detected electrically. They can be rather small and stable at the same time, but the combination of all of these properties in one system remains challenging. A simple proposed concept from the field of skyrmionics is the racetrack memory [8], which consists of a long tape where information bits are physically represented and stored as skyrmions. A similar concept already existed earlier for domain walls [9] and magnetic bubbles [10], but skyrmions can be manipulated with much greater efficiency [11, 12].

Other proposed concepts suggest an even wider range of possible skyrmion applications [13]. For example, it has been shown [14] that it could be possible to construct logic gates, including `AND` and `OR` gates, that directly process skyrmions, potentially enabling energy efficient spin logic devices. Further possibilities for skyrmion based computing include neuromorphic computing devices [15, 16] and quantum bits for quantum computing [17, 18]. Beyond that, there are concepts where skyrmions are not just used as data bits. For example, it was shown [19] that skyrmions might be used in very sensitive microwave detectors.

Almost all proposed applications for Skyrmions require a detection method. While several solutions already exist, each has its drawbacks. Tunnel magnetoresistance (TMR) [20, 21, 22] is well explored and has been experimentally demonstrated as suitable for skyrmion detection [23, 24], but the required magnetic reference layer might disturb the dynamics of the skyrmion in a device. Tunneling anisotropic magnetoresistance (TAMR) [25], on the other hand, does not require a reference electrode, but the effect is typically rather small which makes it harder to apply. Another approach exploits the topological hall effect (THE) [26, 27], caused by emergent magnetic fields of skyrmions, leading to a measurable Hall voltage in the skyrmion plane that allows to detect single skyrmions. While it seems favorable to use this 'topological' effect which can unambiguously identify topological skyrmions, Kimbell et al. [28] explained that detecting THE does not verify a topologically non-trivial spin texture[1]. Besides that the achieved THE signals are still weak [30, 31, 32, 33].

This work focuses on the detection of skyrmions using the tunneling non-collinear magnetoresistance effect (TNCMR), which arises in tunnel junctions similarly to the TAMR but is caused by the continuous change of the magnetization direction. A practical advantage of this approach is that the tunnel junction setup required for this technique can be manufactured with industrial standard methods [34].

Based on the calculations in this work, a very large TNCMR effect can be predicted for a V/Fe/MgO/Cu system, which can largely be explained by the scattering of electrons due to the translational symmetry-breaking magnetic structure of the skyrmion (explained in section 3.3). The subsequent chapters aim to deepen the understanding of the nature of the scattering effect by analyzing its dependence on the barrier width, skyrmion size, and whether other types of symmetry-breaking disturbances, such a phonons or chemical impurities (section 3.5), can lead to a scattering-enhanced conductance increase. Following this, the nature of the quantum well states (QWS) in the iron layer is investigated (section 3.6), as they provide another significant contribution to the overall TNCMR effect. Interestingly, it turns out that one of the two QWS peaks in the density of states only provides a contribution to the transmission due to its disturbance through spin-orbit coupling. This transmission peak is, therefore, very sensitive to the magnetization direction and contributes significantly to the TAMR effect in this material system as well. Similarly, Hanneken et al. [35] and Crum et al. [36] predicted a non-collinear magnetoresistance (NCMR) or tunnelling spin-mixing magnetoresistance (TXMR) effect, which is caused by electron density changes due to spin mixing and measurable with scanning tunneling microscope (STM) tips. However, requiring an STM makes this method impractical for industrially manufactured devices. Additionally, the effect described in this work cannot be explained based on electron density changes, but instead makes use of the symmetry-filtering property of the MgO tunnel layer. Thus, we chose the name tunneling non-collinear magnetoresistance effect (TNCMR) over NCMR to emphasize the significance of the tunneling aspect. We avoided the term spin-mixing because it refers to changes of the local density of states due to spin-mixing, which is not the primary origin of the effect we describe.

---

[1] The bimeron [29] is an exception from this restriction.

The tunneling non-collinear magneto Seebeck effect (TNCMS) describes the change of a voltage drop through a magnetic tunnel junction generated by a temperature gradient in the presence of non-collinear magnetic structures. It is another way to measure changes of the energy dependent transmission and is mostly dependent on the derivative by energy of the transmission [37], in contrast to the TNCMR effect, which depends on its absolute value. This possibility is analyzed in chapter 4, where I show that the presence of a skyrmion indeed influences the Seebeck coefficient. Essentially, I can show that the absolute value of the Seebeck coefficient is decreased by the skyrmion for most energies because the skyrmion tends to blur peaks in the energy dependent transmission.

Besides the above considerations on conventional skyrmions, it is worth noting that skyrmions have some drawbacks which make applications difficult. For example, magnetic impurities can lead to the pinning of skyrmions [38], meaning that if a skyrmion is meant to be moved along a racetrack, it can get stuck at any one of these impurities. Another issue is that when a skyrmion is moved along a racetrack using currents, it experiences a Magnus force perpendicular to the movement direction. It can lead to the destruction of skyrmions when they are pushed against the side of the racetrack. This effect is called the skyrmion Hall effect (SkHE) [39], and it is the counterpart of THE. Antiferromagnetic skyrmions do not experience the skyrmion Hall effect, have faster and more efficient dynamics [40], lack unwanted long range interactions via stray fields [41], and are less prone to pinning by impurities [42], making them promising candidates for applications [43]. However, just like antiferromagnetic skyrmions are not affected by the SkHE, they also cannot be detected using the THE. Since they usually have no net magnetization, they also cannot be detected through TMR. This brings the focus back to other detection mechanisms beyond TMR and THE, where TNCMR offers a promising alternative for detecting antiferromagnetic non-collinear structures. The suitability of TNCMR for detecting antiferromagnetic skyrmions is explored in chapter 5. To provide an appropriate antiferromagnetic [44] model system for a hypothetical antiferromagnetic skyrmion for the calculation, I replaced the Fe layer with a manganese layer grown on top of a silver monolayer. My calculations on this model system show that both TNCMR and TNCMS can, in principle, lead to significant signals for antiferromagnetic skyrmion detection.

While TNCMR and TNCMS might detect non-collinear spin structures, it is difficult to use them to recognize the topological nature of the detected structure. Recently, it was demonstrated [45] that a spin-orbit coupling enabled chiral spin-mixing magnetoresistance effect (C-XMR) can distinguish between topological structures that differ only in their helicity by the resulting resistance through a tunnel junction. However, this approach is not feasible if the sensor does not provide a good spatial resolution, i.e. if STM tips are not used, and if the considered magnetic structures are not well known. To address this issue, I propose a setup in chapter 6 that aims to probe the topological nature of unknown spin structures by utilizing the TMR signal from multiple magnetic tunnel junctions (MTJs) with different magnetization directions of their reference electrodes. When a topologically non-trivial spin textures passes through the proposed arrangement of MTJs, the same signal is expected from all MTJs. All other spin textures, however, are expected to lead to different signals from the MTJs, allowing for differentiating between the two cases.

Finally, I conclude in chapter 7 with a discussion of the practical applicability of the results and possible pathways for further research.

Chapter 2

Theory

In this chapter, I introduce the theoretical foundations and the tools based on them that I used in this work to gain deeper insight into the physical nature of electronic transport in tunnel junctions, including complex spin textures. Beyond that, I provide more physical background information necessary for a qualitative understanding of the nature of electronic transport in tunnel junctions and the formation of complex spin textures like skyrmions.

2.1 Density functional theory

In order to accurately describe the quantum mechanical behaviour of the considered materials, density functional theory (DFT) [46, 47] has proven to be a valuable tool. In principle, if we want to understand the physics of any material, we have to solve the Schrödinger equation for the many-body system of N_e electrons and N_k nuclei. While the exact wavefunction of the full many-body system is practically impossible to solve, within DFT, the ground state of any given Hamiltonian is uniquely described by its electron density. The many-body wave function is no longer required. Instead, similarly to the Hartree-Fock method, the interacting many-body system can be reduced to an effective single-particle system, which tremendously reduces the computational complexity. The ground-state orbitals ϕ_j of this effective system satisfy the Kohn-Sham [48] equation

$$(-\frac{1}{2}\nabla^2 + V_{\text{eff}}(\vec{r}) - \epsilon_j)\phi_j(\vec{r}) = 0 \tag{2.1}$$

$$\Leftrightarrow \hat{H}\left|\phi_j\right\rangle = \epsilon_j \left|\phi_j\right\rangle , \tag{2.2}$$

they minimize the total energy, and they reproduce the electron density of the real many-body system. The electron density

$$n(\vec{r}) = \sum_{j=1}^{N_e} |\phi_j(\vec{r})|^2 \tag{2.3}$$

is used to calculate the effective potential V_{eff} :

$$V_{\text{eff}}(\vec{r}) = V_{ek}(\vec{r}) + V_{ee}(\vec{r}) + V_{\text{xc}}(\vec{r}). \tag{2.4}$$

It is composed of three terms. First the electrostatic potential due to the positive electric point charges of the atomic nuclei

$$V_{ek}(\vec{r}) = -\sum_{n}^{N_k} \frac{2Z_k}{|\vec{r} - \vec{R}_k|} \tag{2.5}$$

which are described as point charges sitting at static positions. This assumption is called the Born-Oppenheimer approximation [49] and is justified by the fact that the lighter electrons move much faster than the heavy nuclei. The second term describes the electrostatic potential due to the negative distributed electric charge of the electrons

$$V_{ee}(\vec{r}) = \int \frac{n(\vec{r'})}{|\vec{r} - \vec{r'}|} \mathrm{d}\vec{r'}. \tag{2.6}$$

In total the first two parts of the potential form the Hartree potential [50]

$$V_{\text{Hartree}}(\vec{r}) = V_{ek}(\vec{r}) + V_{ee}(\vec{r}). \tag{2.7}$$

All other many-body contributions that go beyond the Hartree method are summarized in the exchange-correlation potential V_{xc}. Contributions to V_{xc} which originate from the exchange symmetry of the electrons being identical particles, which are covered within the Hartree-Fock method [51, 52, 53], are called exchange energy. The very complex rest that the Hartree-Fock model misses from the exact solution is summarized under the name correlation energy [48]. The main drawback of DFT is the fact that while the exchange-correlation potential V_{xc}, as a functional of the electron density, is proven to exist, its exact form is unknown. This is why approximative functionals like local density approximation (LDA) [54, 55, 56, 57] or generalized gradient approximation (GGA) [58, 59, 60] have to be used for calculations.

2.2 The KKR method

Most DFT based methods directly calculate the Kohn-Sham orbitals ϕ from the potential and use these to further compute the electron density. In contrast, the KKR [61, 62, 63, 64, 65, 66] method makes use of the Green function of the Kohn-Sham equation. The Green function [67, 68] for the Kohn-Sham system is defined as:

$$\hat{G}(z) = (z\hat{I} - \hat{H})^{-1}. \tag{2.8}$$

Where $z = E \pm i\eta$ is the complex energy. The Green function operator can be projected onto real space:

$$G(\vec{r}, \vec{r}'; z) = \langle \vec{r} | \hat{G}(z) | \vec{r}' \rangle \tag{2.9}$$

Two limits are defined:

$$\lim_{|\eta| \to 0} \hat{G}(E \pm i\eta) = \begin{cases} G^{+}(E)\ ; & \text{retarded Green function (outgoing waves)} \\ G^{-}(E)\ ; & \text{advanced Green function (incoming waves)} \end{cases} \tag{2.10}$$

Using the Green function, the expectation value of any hermitian operator $\hat{A}$ is accessible:

$$\langle \hat{A} \rangle = -\frac{1}{\pi} \int_{-\infty}^{E_F} \mathrm{d}E \ \mathrm{Im}\mathrm{Tr}[\hat{A}\hat{G}(E)] \tag{2.11}$$

2.2.1 Dyson equation

Following [69], let us assume we have a system with the Hamiltonian $\hat{H} = \hat{H}_0 + \hat{V}$, and the Green function of $\hat{H}_0$ shall already be known. Then we can write down both Green functions

$$\hat{G}_0^{\pm}(E) = \lim_{\eta \to 0^{+}} \frac{\hat{I}}{E \pm i\eta - \hat{H}_0} \tag{2.12}$$

and

$$\hat{G}^{\pm}(E) = \lim_{\eta \to 0^{+}} \frac{\hat{I}}{E \pm i\eta - \hat{H}} \Rightarrow (\hat{G}^{\pm}(E))^{-1} = (\hat{G}_0^{\pm}(E))^{-1} - \hat{V} \tag{2.13}$$

.

By inverting both equations, we can easily prove

$$\Rightarrow (\hat{G}^{\pm}(E))^{-1} = (\hat{G}_0^{\pm}(E))^{-1} - \hat{V}, \tag{2.14}$$

which again can then be rewritten as

$$\Rightarrow \hat{G}^{\pm}(E) = \hat{G}_0^{\pm}(E) + \hat{G}^{\pm}(E)\hat{V}\hat{G}_0^{\pm}(E). \tag{2.15}$$

The equation (2.15) is usually referred to as the Dyson equation. For the next steps, it is helpful to expand this expression for $\hat{G}$ into an infinite chain by repeatedly substituting the expression for $\hat{G}$ in itself, which leads to

$$\Rightarrow \hat{G}(E) = \hat{G}_0(E) + \hat{G}_0(E)\hat{V}\hat{G}_0(E) + \hat{G}_0(E)\hat{V}\hat{G}_0(E)\hat{V}\hat{G}_0(E) + \ldots \tag{2.16}$$

In the next step, we define the transfer operator $\hat{T}$ as

$$\hat{T}(E) = \hat{V} + \hat{V}\hat{G}_0(E)\hat{V} + \hat{V}\hat{G}_0(E)\hat{V}\hat{G}_0(E)\hat{V} + \ldots \tag{2.17}$$

This allows us to write down a few equivalent and commonly used expressions:

$$\begin{align}
\hat{G}(E) &= \hat{G}_0(E) + \hat{G}_0(E)\hat{T}(E)\hat{G}_0(E) \tag{2.18}\\
\Leftrightarrow \hat{T}(E) &= \hat{V} + \hat{V}\hat{G}_0(E)\hat{T}(E) \tag{2.19}\\
\Leftrightarrow \hat{T}(E) &= \hat{V} + \hat{T}(E)\hat{G}_0(E)\hat{V} \tag{2.20}\\
\Leftrightarrow \hat{T}(E)\hat{G}_0(E) &= \hat{V}\hat{G}(E) \tag{2.21}\\
\Leftrightarrow \hat{G}_0(E)\hat{T}(E) &= \hat{G}(E)\hat{V} \tag{2.22}
\end{align}$$

2.2.2 Lippmann-Schwinger equation

Now, we want to take a look at the eigenfunctions of both systems

$$(z\hat{I} - \hat{H})\psi(E) = 0 \text{ and } (z\hat{I} - \hat{H}_0)\psi_0(E) = 0. \tag{2.23}$$

By defining the difference between both eigenfunctions

$$\psi(E) = \psi_0(E) + \delta\psi(E), \tag{2.24}$$

we can prove

$$\begin{align}
(z\hat{I} - \hat{H})\psi(E) &= 0 \tag{2.25}\\
\Rightarrow (z\hat{I} - \hat{H}_0 - \hat{V})(\psi_0(E) + \delta\psi(E)) &= 0 \tag{2.26}\\
\Rightarrow \underbrace{(z\hat{I} - \hat{H}_0)\psi_0(E)}_{=0} + (z\hat{I} - \hat{H}_0)\delta\psi(E) &= \hat{V}\psi_0(E) + \hat{V}\delta\psi(E) \tag{2.27}\\
\Rightarrow \delta\psi(E) &= \hat{G}_0\hat{V}\psi(E), \tag{2.28}
\end{align}$$

leading to the Lippmann-Schwinger equation [70]

$$\Rightarrow \psi(E) = \psi_0(E) + \hat{G}_0\hat{V}\psi(E). \tag{2.29}$$

When we expand this equation by repeatedly substituting it in itself, we find that

$$\begin{aligned}\psi(E) &= \psi_0(E) + \hat{G}_0\hat{V}(\psi_0(E) + \hat{G}_0\hat{V}\psi(E))\\ &= \psi_0(E) + \hat{G}_0\hat{V}\psi_0(E) + \hat{G}_0\hat{V}\hat{G}_0\hat{V}(\psi_0(E) + \hat{G}_0\hat{V}\psi(E))\\ &= \psi_0(E) + \hat{G}_0\hat{V}\psi_0(E) + \hat{G}_0\hat{V}\hat{G}_0\hat{V}\psi_0(E) + \hat{G}_0\hat{V}\hat{G}_0\hat{V}\hat{G}_0\hat{V}\psi(E)\\ &= \psi_0(E) + \hat{G}_0\underbrace{(\hat{V} + \hat{V}\hat{G}_0\hat{V} + \hat{V}\hat{G}_0\hat{V}\hat{G}_0\hat{V} + \dots)}_{=\hat{T}}\psi_0(E)\end{aligned}$$

$$\Rightarrow \psi(E) = \psi_0(E) + \hat{G}_0\hat{T}\psi_0(E). \tag{2.30}$$

So we can prove

$$\delta\psi(E) = \hat{G}_0\hat{T}\psi_0(E). \tag{2.31}$$

Now we have two expressions 2.31 and 2.28 for $\delta\psi(E)$. By setting both equations equal, we can derive

$$\delta\psi(E) = \delta\psi(E) \tag{2.32}$$

$$\Leftrightarrow \hat{G}_0\hat{T}\psi_0(E) = \hat{G}_0\hat{V}\psi(E) \tag{2.33}$$

$$\Leftrightarrow \hat{T}\psi_0(E) = \hat{V}\psi(E) \tag{2.34}$$

2.2.3 Decomposition of space into atomic regions

One important idea behind the KKR method is the decomposition of the crystal potential into many single atom-centered potentials. A common approximation is the muffin-tin approximation (MT) [71], where all these atom-centered potentials are assumed to be spherically symmetric and non-overlapping, with the potential in the gaps is set to a constant value. In contrast, the similar atomic-sphere approximation (ASA) [72] allows the spherical potentials to overlap but ensures that the total volume of the spheres matches the total crystal volume. The following derivation is based on the MT approximation.

For MT potentials we have:

$$V_{eff}(\vec{r}) = \sum_n V_n(\vec{r}_n) \text{ with: } \vec{r}_n = \vec{r} - \vec{R}_n \tag{2.35}$$

$$V_n(\vec{r}_n) = \begin{cases} V_{Atom}(|\vec{r}_n|) & \text{if } |\vec{r}_n| \leq R_{MT} \\ 0 & \text{if } |\vec{r}_n| > R_{MT} \end{cases} \tag{2.36}$$

Inserting this potential into equation 2.8 leads to

$$[E + \frac{1}{2}\nabla^2 - V_n(\vec{r})]G(\vec{R}^n + \vec{r}, \vec{R}^{n'} + \vec{r}'; E) = \delta_{n,n'}\delta(\vec{r} - \vec{r}'). \tag{2.37}$$

The Green function to a constant zero potential is analytically known:

$$G_0(\vec{r}, \vec{r}'; E) = -\frac{1}{4\pi}\frac{e^{i|\vec{r}-\vec{r}'|\sqrt{E}}}{|\vec{r} - \vec{r}'|} \tag{2.38}$$

Then the Dyson equation allows us to calculate G from G_0.

2.2.4 Single-scatterer

Instead of directly solving the Dyson equation for the entire system at once, in the KKR method we first solve the Dyson equation for each isolated atom individually. For this step, we need to express the Green function of the free electron system in terms of spherical harmonics as

$$G_0(\vec{r}, \vec{r}'; E) = \sum_L Y_L(\vec{r}) g_l^0(r, r'; E) Y_L(\vec{r}')^* \tag{2.39}$$

$$\text{with } g_l^0(r, r'; E) = -i\sqrt{E} j_l(\sqrt{E} r_<) h_l(\sqrt{E} r_>). \tag{2.40}$$

Here, $h_l = j_l + i n_l$, with h_l being the Hankel function, n_l the Neumann function, and j_l the Bessel function, while Y_L are the spherical harmonics. L is a combined index of l and m. We distinguish between the larger and smaller norm of the two vectors $\vec{r}'$ and $\vec{r}$ by defining $r_< = \min(r, r')$ and $r_> = \max(r, r')$. Note that j_l and h_l are the solutions of the Schrödinger equation in empty space. For any spherical potential the solution of the Kohn-Sham equation can be decomposed into a spherical $Y_L(\vec{r})$ and a radial $R_l(r; E)$ part. For the radial part

$$\left[-\frac{\partial^2}{\partial r^2} + \frac{l(l+1)}{r^2} + V(r) - E\right] R_l(r; E) = 0 \tag{2.41}$$

holds. This equation is easy to solve numerically. Applying the Lippmann-Schwinger equation 2.29 to the radial solution, by associating $\psi_0 \rightarrow j_l(\sqrt{E} r)$ and $\psi \rightarrow R_l(r'; E)$, leads to:

$$R_l(r; E) = j_l(\sqrt{E} r) + \int_0^{R_{MT}} g_l^0(r, r'; E) V(r') R_l(r'; E) r'^2 \mathrm{d}r' \tag{2.42}$$

If $r > R_{MT}$ we can write

$$R_l(r;E) = j_l(\sqrt{E}r) - ih_l(\sqrt{E}r)\sqrt{E}\int_0^{R_{MT}} j_l(\sqrt{E}r')V(r')R_l(r';E)r'^2\mathrm{d}r'. \tag{2.43}$$

Following [69, 73], by projecting the transfer operator $\hat{t}$ onto the basis of j_l, we can write

$$\begin{aligned} t_l &:= \langle j_l|\hat{t}|j_l\rangle && (2.44)\\ &= \langle j_l|\hat{V}|R_l\rangle && (2.45)\\ &= \int_0^{R_{MT}} j_l(\sqrt{E}r')V(r')R_l(r';E)r'^2\mathrm{d}r', && (2.46)\end{aligned}$$

where we use relation 2.34 to get from step 2.44 to step 2.45. This allows us to simplify equation 2.43 to

$$\Rightarrow R_l(r;E) = j_l(\sqrt{E}r) - i\sqrt{E}t_l(E)h_l(\sqrt{E}r) \text{ for } r \geq R_{MT}. \tag{2.47}$$

Besides the regular scattering solution $R_l(r;E)$ with $\lim_{r\to 0} R_l(r;E) = 0$ we also get an irregular solution $H_l(r;E)$ with $\lim_{r\to 0} H_l(r;E) = \infty$. The Green function of the single scatterer g_S has the form

$$g_S(r',r;E) = \sqrt{E}\sum_L H_l(r_>;E)R_l(r_<;E)Y_L(\vec{r})Y_L(\vec{r}')^*. \tag{2.48}$$

It thus has a similar structure as the Green function of the free electron system 2.39. We just need to replace $h \to H$, and $j \to R$. In the full-potential KKR [74, 75] even non-spherical contributions can be included in a similar fashion.

2.2.5 Multi-scatterer

At this step, we have only obtained the Green function for a single isolated atom in empty space, but we can also see that $g_S(\vec{r}_n', \vec{r}_n; E)$ is an inhomogeneous solution of the linear differential equation (2.37) for $n = n'$. The remaining part of the Green function of the crystal has to describe the scattering between the individual atoms and only needs to solve the homogeneous part of equation (2.37), i.e., with the right-hand side being 0. The complete solution to equation (2.37) is then the sum of both solutions. This separation of the atomic potentials and the crystal structure is one of the key features of the KKR method.

To describe the full Green function, we can use the solutions of the single scatterer as a basis set

$$G(\vec{r}_n, \vec{r}_{n'}; E) = \delta_{nn'} g_S(\vec{r}_n, \vec{r}_{n'}; E) + \sum_{LL'} R^n_L(\vec{r}_n; E) G^{nn'}_{LL'}(E) R^{n'}_{L'}(\vec{r}_{n'}; E)^\times. \tag{2.49}$$

Where we simplified the notation by combining the spherical harmonics and the radial functions to

$$f_L(\vec{r}; E) = f_l(r; E) Y_L(\vec{r}) \tag{2.50}$$

and

$$f_L(\vec{r}; E)^\times = f_l(r; E) Y_L(\vec{r})^*. \tag{2.51}$$

The Dyson equation for this ansatz leads to the algebraic Dyson equation

$$G^{nn'}_{LL'}(E) = g^{0,nn'}_{LL'}(E) + \sum_{L'',n''} g^{0,nn''}_{LL''}(E) t^{n''}_{l''}(E) G^{n''n'}_{L''L'}(E) \tag{2.52}$$

for the relationship between the structure constants of the full Green function $G^{nn'}_{LL'}(E)$ and the structure constants $g^{0,nn'}_{LL'}$ of the reference system, which are also called structural Green functions. For details of this part of the derivation and the expressions for $g^{0,nn'}_{LL'}$, I want to refer to [73].

Now, we want to rewrite it to see how it is actually solved in practice and to prepare for the treatment of two-dimensional systems. To make it more compact we can rewrite equation 2.52 for the structural Green function by hiding the indices as

$$G = G^0 + G^0 t G. \tag{2.53}$$

By reinserting this expression for G on the right side of itself, we can expand the equation to

$$G = G^0 + G^0 t G^0 + G^0 t G^0 t G^0 t + \ldots \tag{2.54}$$

and by defining the scattering path operator τ analogously to the transfer operator in equation 2.18 as

$$\tau = t + t G^0 t + t G^0 t G^0 t + \ldots \tag{2.55}$$

we can write

$$G = G^0 + G^0 \tau G^0. \tag{2.56}$$

And just as we expanded equation 2.52 to equation 2.54, we can take equation 2.55 and extract

$$\tau = t + tG^0\tau. \tag{2.57}$$

When we solve this equation for τ we get

$$\tau = (t^{-1} - G^0)^{-1}. \tag{2.58}$$

And we can prove that the expression

$$G = -t^{-1} + (t^{-1}\tau t^{-1}), \tag{2.59}$$

is correct, because inserting the expanded expression for τ from equation 2.55 into equation 2.59 leads to

$$G = -t^{-1} + (t^{-1}(t + tG^0t + tG^0tG^0t + \dots)t^{-1}) = G^0 + G^0tG^0 + G^0tG^0tG^0t + \dots, \tag{2.60}$$

which we already know as equation 2.54.

2.2.6 In the periodic lattice

Up to now, the index n runs over all atoms in the entire system. Since we want to treat infinite lattices, we need to exploit the periodicity of the crystal lattice and switch to reciprocal space. We redefine the indices, so that n stands for a position on the lattice and the new atomic index μ refers to individual atoms within one unit cell. When we apply the Fourier transform to the structure constants we get

$$\overset{\mu\mu'}{G^{nn'}_{LL'}}(E) = \frac{\Omega}{(2\pi)^3}\int_{\Omega_{BZ}} \mathrm{d}^3k\; e^{-i\vec{k}\vec{R}_{nn'}} G^{\mu\mu'}_{LL'}(\vec{k}; E) \tag{2.61}$$

and

$$G^{\mu\mu'}_{LL'}(\vec{k}; E) = \sum_n e^{+i\vec{k}\vec{R}_{nn'}} \overset{\mu\mu'}{G^{nn'}_{LL'}}(E). \tag{2.62}$$

This leads to

$$G^{\mu\mu'}_{LL'}(\vec{k}; E) = g^{0,\mu\mu'}_{LL'}(\vec{k}; E) + \sum_{\mu''L''} g^{0,\mu\mu''}_{LL''}(\vec{k}; E)t^{\mu''}_{L''}(E)G^{\mu''\mu'}_{L''L'}(\vec{k}; E). \tag{2.63}$$

Equation 2.62 is independent of n', because the sum is infinite, and due to the translational invariance of the lattice, the dependence of $\overset{\mu\mu'}{G^{nn'}_{LL'}}(E)$ on n and n' comes down to a dependence on the difference between the lattice vectors $\vec{R}_{nn'} = \vec{R}_n - \vec{R}_{n'}$.

2.2.7 Screened KKR

A major shortcoming of the previously explained KKR method, as derived using free electrons as reference system, is that the Green function of the free electron system $g^{0,nn'}_{LL'}(E)$ has a long range and decays very slowly with increasing distance between atoms n and n'. This means practically solving the Dyson equation 2.52 in this case requires a computationally demanding Ewald summation. However, it was shown [76, 77, 78] that this issue can be circumvented by introducing an artificial repulsive reference potential V_R with the corresponding Green function G_R. Following [79], we start with equation 2.53 and solve for G leading to

$$G = (I - G_0 t)^{-1} G_0 \tag{2.64}$$

and the equivalent equation for any reference potential V_R

$$G_R = (I - G_0 t_R)^{-1} G_0. \tag{2.65}$$

By inverting both sides of the equation, we can write

$$G^{-1} = G_0^{-1}(I - G_0 t) = G_0^{-1} - t \tag{2.66}$$

and

$$G_R^{-1} = G_0^{-1} - t_R \Rightarrow G_0^{-1} = G_R^{-1} + t_R. \tag{2.67}$$

By inserting the expression for G_0^{-1} from equation 2.67 into equation 2.66, we get

$$G^{-1} = G_R^{-1} + t_R - t = G_R^{-1} - \Delta t, \tag{2.68}$$

with

$$\Delta t = t - t_R. \tag{2.69}$$

So like equation 2.64, we can write

$$G = (I - G_R \Delta t)^{-1} G_R. \tag{2.70}$$

We can also rewrite equations 2.58 and 2.59 using the scattering path operator and defining the KKR matrix M, resulting in

$$\tau_\Delta^{-1} = M = ((\Delta t)^{-1} - G_R) \tag{2.71}$$

and

$$G = -(\Delta t)^{-1} + ((\Delta t)^{-1}\tau_{\Delta}(\Delta t)^{-1}). \tag{2.72}$$

Note that the derivation involves no assumptions regarding the reference potential. In the screened KKR the reference potential V^R is typically zero in the regions between the muffin-tin spheres and a very high constant value inside of the muffin-tin spheres. Given that the arrangement of muffin-tin spheres is sufficiently dense, the reference system has no electronic states in the relevant energy range, and the Green function G_R has a short range. To obtain the structural Green function of the physical system $G^{nn'}_{LL'}(E)$, we first calculate the structural reference Green function $G^{R,nn'}(E)$ by solving the Dyson equation for the reference system in real space

$$G^{R,nn'}_{LL'}(E) = g^{0,nn'}_{LL'}(E) + \sum_{L'',n''} g^{0,nn''}_{LL''}(E)t^{R,n''}_{l''}(E)G^{R,n''n'}_{L''L'}(E). \tag{2.73}$$

Then in a second step, we fourier transform the structure constants of the reference system $G^{R,nn'}_{LL'}(E)$ to $G^{R,\mu\mu'}_{LL'}(\vec{k};E)$ and calculate $t^{n''}_{l''}(E)$ of the physical system. Then we can calculate the fourier transformed scattering path operator of the physical system $\tau^{\mu\mu'}_{LL'}(\vec{k};E)$ by inverting

$$M^{\mu\mu'}_{LL'}(\vec{k};E) = (\Delta t^{\mu'}_{l'}(E))^{-1}\delta_{LL'}\delta_{\mu\mu'} - G^{R,\mu\mu'}_{LL'}(\vec{k};E), \tag{2.74}$$

which is sparse for large systems because of the screening reference system. The difference of t-matrices

$$\Delta t^{\mu'}_{l'}(E) = t^{\mu'}_{l'}(E) - t^{R,\mu'}_{l'}(E) \tag{2.75}$$

follows from 2.69. In actual calculations, for large physical systems, the overwhelming majority of the computational effort is spent on inverting the KKR matrix M, which can be done much more efficiently when M is sparse. As the last step we just need to evaluate equation 2.72 to obtain $G^{\mu\mu'}_{LL'}(\vec{k};E)$. By solving equation 2.73 in real space and 2.74 in reciprocal space, they are both much easier to solve than the direct step using only the free electrons as reference system. Since the reference potential leads to a screening between the atoms and tightly coupled equations regarding range, this method is typically referred to as screened KKR or tight-binding KKR. Besides leading to less computational effort, the screening potential V^R also allows embedding [80] two-dimensional, one-dimensional, or even point-like structures (impurities) into the three-dimensional base structure without the need for supercells. Later in this work, we will use this technique for layered i.e. two-dimensional systems.

2.2.8 Calculating the electron density

An important intermediate step in DFT calculations is calculating the electron density $n(\vec{r})$. From equation 2.11, we already know how to calculate the expectation value of any hermitian operator once the Green function $G(E)$ is known. By setting $\hat{A} \to \hat{I}$, the density of states can be calculated in this way as well:

$$n(\vec{r}) = -\frac{1}{\pi} \int_{-\infty}^{E_F} \mathrm{d}E \; \mathrm{Im} G^{+}(\vec{r}, \vec{r}; E) \tag{2.76}$$

However, we need to acknowledge that at finite energies not all states are occupied. To obtain the actual electron density, we need to multiply the integrand with the Fermi-Dirac distribution

$$f(E, E_{\mathrm{F}}, T) = \frac{1}{e^{\frac{E-E_{\mathrm{F}}}{k_{\mathrm{B}}T}} + 1}, \tag{2.77}$$

which has its so-called Matsubara poles [81] at

$$z_n = E_{\mathrm{F}} + i\pi(2n-1)k_{\mathrm{B}}T, \tag{2.78}$$

for all $n \in \mathbb{Z}$. While density functional theory is originally formulated for zero temperature, the above approach, known as finite-temperature DFT, is justified by [82, 83]. The naive straightforward approach to calculate the electron density would be to numerically evaluate the integral in expression 2.76 exactly as it is written along the $\mathrm{Im}(z) = 0$ real axis. However, since the valence electronic states are directly linked to poles of the Green function at $\mathrm{Im}(z) = 0$, the Green function, and therefore the integrand $n(E)$, has a very rough structure close to the real axis. As described by Wildberger et al. [83], it is numerically much easier to utilize the residue theorem, which allows us to integrate along a different energy path further away from the poles on the real axis. The integral path starts at a bottom energy E_{B} between the core states, which are easier to treat separately, and the valence states. From this point, the first part of the integrating path moves perpendicular away from the real axis up to $z = N k_{\mathrm{B}} T$, if we want to encircle N Matsubara poles. From there, the second part of the integrating path follows parallel to the real axis up to the Fermi energy. Instead of turning back to the real axis, the third part of the integrating path continues to higher E, where the integrand vanishes due to the suppressing influence of the Fermi-Dirac distribution. This eventually leads to the same result as if we had taken an integration path back to the real axis. By following the described paths with relatively few energy sampling points and after evaluating circled residues corresponding to the Matsubara poles, we achieve an accurate result for the electron density $n(\vec{r})$.

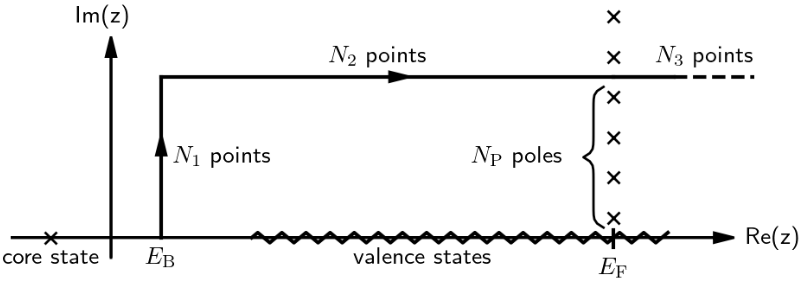

Figure 2.1: The integration path used to calculate the electron density. The exact locations of the Matsubara poles and typical locations of poles and branch cuts of the Green function due to electronic states are sketched as well. The numbers of energy mesh sampling points are denoted for later reference.

2.2.9 Self-consistent cycle

It is, in general, not possible to directly compute a Green function for a system where the corresponding charge density leads to a Kohn-Sham potential that agrees with the Green function through the Kohn-Sham equation. However, what we can do is to start with an initial potential guess and then repeat the following cycle [66]:

1. Start with an initial potential guess V^{in}.
2. Calculate the single-scatterer properties $R_{LL'}$ and $t_{LL'}$ for the current V^{in} .
3. Solve the Dyson equation and integrate over the Brillouin zone to get $G_{LL'}(E)$.
4. Compute the Green function in real space $G(\vec{r}, \vec{r}'; E)$ with $\vec{r}' = \vec{r}$.
5. Integrate $G(\vec{r}, \vec{r}; E)$ over the energy to obtain the valence electron density.
6. Compute the core states with their corresponding charge densities.
7. Add both densities to the total electron density, solve the Poisson equation, and add the exchange-correlation potential to get the new potential V^{out} .
8. We are done if the difference between V^{out} and V^{in} is small enough. Otherwise, use V^{out} as V^{in} and repeat starting from step 2. In practice, a composition of previous potentials is used to compute the new V^{in} potential.

This means that by starting with a potential guess, we repeat the cycle until self-consistency is eventually achieved. The final result is a potential, electron density, and Green function G that satisfy the Kohn-Sham equations for that particular atomic arrangement.

2.2.10 2D Systems

The previously explained method is very useful for describing 3D crystals with potentially large unit cells, but it cannot accurately describe 2D systems like graphene or magnetic tunnel junctions, as in this work, without using larger artificial supercells. However, following reference [79], the screened KKR method allows us to split a considered 2D system into a center region connected to a left and a right semi-infinite region on either side. Then along the axis perpendicular to the interface planes between the three regions, the system is treated in real space, while in the infinite planes, we can work in reciprocal space with a wave vector $\vec{k}_{\|}$. Treating the Dyson equation in real space in one dimension and in reciprocal space in the two other dimensions leads to the following equation, where the index μ runs now over all atoms in an infinitely long cell:

$$G_{LL'}^{\mu\mu'}(\vec{k}_{\|};E) = G_{LL'}^{R,\mu\mu'}(\vec{k}_{\|};E) + \sum_{L'',\mu''} G_{LL''}^{R,\mu\mu''}(\vec{k}_{\|};E)\Delta t_{l''}^{\mu''}(E) G_{L''L'}^{\mu''\mu'}(\vec{k}_{\|};E). \tag{2.79}$$

The indices of the atoms are chosen such that they increase continuously as one moves from atoms in the left lead through the central region to the right lead. $G_{LL'}^{R,\mu\mu'}(\vec{k}_{\|};E)$ decays exponentially with increasing distance between the atoms μ and μ', leading to a banded matrix structure of G. We can then group the atoms into so-called principal layers with index α, and within a layer, a second index β, such that the matrix $G_{LL'}^{R,\alpha\alpha'\beta\beta'}(\vec{k}_{\|};E)$ is essentially tridiagonal with respect to the index α. The index β then only runs up to a rather small number, while α runs over infinitely many layers.

In the next step, we divide the system into three regions: A finite center region (C), which can have a rather complex structure, a left semi-infinite region (L), and a right semi-infinite region (R). Here, 'semi-infinite' means that they are limited by their interface with the center region C on one side but extend infinitely in the other direction. The atomic structure in both semi-infinite regions is periodic in all directions except for the border to region C. Region C shall have a length of N principal layers:

$$1 \leq \alpha \leq N \tag{2.80}$$

When the region C is sufficiently long, the band shape of $G_{LL'}^{R,\alpha\alpha'\beta\beta'}(\vec{k}_{\|};E)$ allows us to write the matrix M from equation 2.74 as

$$M = \begin{pmatrix} M_{LL} & M_{LC} & 0 \\ M_{CL} & M_{CC} & M_{CR} \\ 0 & M_{RC} & M_{RR} \end{pmatrix}, \tag{2.81}$$

where M_{LL} and M_{RR} are both semi-infinite matrices. The coupling sub-matrices M_{LC},

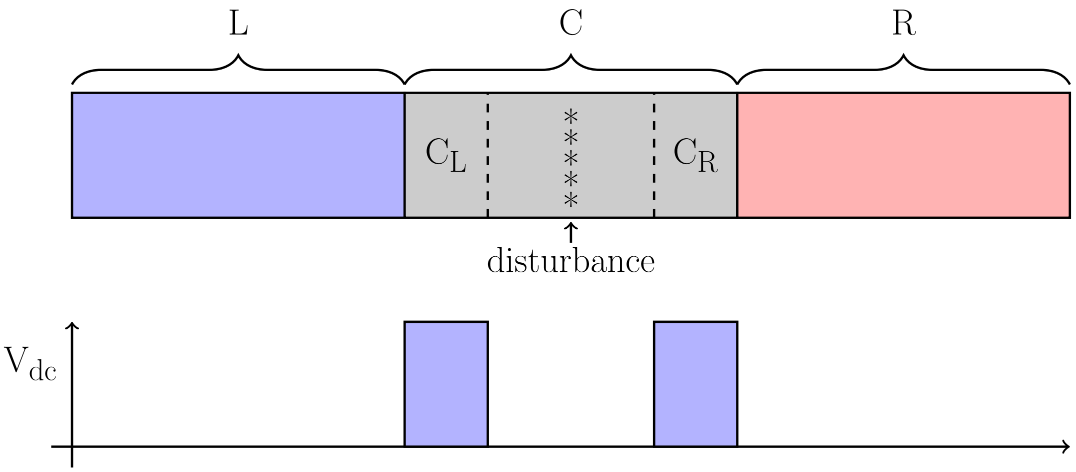

Figure 2.2: The three regions (L,C,R) into which the system is divided. The scattering due to skyrmions, which is investigated in this work, occurs only in the middle of the center region. Below: The decoupling potential V_{dc} is non-zero in the outer parts of the center region.

M_{CL}, M_{CR}, M_{RC} each contain only one non-zero block regarding the principal layer index α. Then it holds for the scattering path operator:

$$\tau = M^{-1} \Rightarrow \begin{pmatrix} \tau_{LL} & \tau_{LC} & 0 \\ \tau_{CL} & \tau_{CC} & \tau_{CR} \\ 0 & \tau_{RC} & \tau_{RR} \end{pmatrix} \begin{pmatrix} M_{LL} & M_{LC} & 0 \\ M_{CL} & M_{CC} & M_{CR} \\ 0 & M_{RC} & M_{RR} \end{pmatrix} = I \tag{2.82}$$

By solving the linear equation system we get the following expression for the center region of τ:

$$\tau_{CC} = (M_{CC} - M_{CL}M_{LL}^{-1}M_{LC} - M_{CR}M_{RR}^{-1}M_{RC})^{-1} \tag{2.83}$$

Note that all terms in τ_{CC}^{-1} except for M_{CC} are independent of any structures in the middle of the center region, which will become important later on. Because of the band shape of M, we only need the two principal layer blocks

$$\left[(M_{LL})^{-1}\right]^{0,0} \tag{2.84}$$

and

$$\left[(M_{RR})^{-1}\right]^{N+1,N+1} \tag{2.85}$$

of the inverted semi-infinite matrices. These two blocks are calculated using the so-called decimation technique, which is explained in detail by Wildberger [79], and they are known as the surface Green functions. Then, to obtain the full Green function in the center region, only equation 2.72 needs to be evaluated.

2.3 Non-equilibrium Green function (NEGF)

To calculate the resistance of coherent electronic transport through a barrier, the non-equilibrium Green function (NEGF) [68] can be used. The NEGF method works directly with the Green function, which is the main subject of the KKR method, and has already been implemented [84] in the KKR code used in this work. Following [85, 86], we consider a given physical system that is divided into the previously explained three regions: left, center, and right, as displayed in figure 2.2. The decoupled (dc) Hamiltonian

$$H_{dc} = \begin{pmatrix} h_L & 0 & 0 \\ 0 & h_C & 0 \\ 0 & 0 & h_R \end{pmatrix}, \tag{2.86}$$

shall then describe the three regions separately without any interaction, with the corresponding decoupled Green function

$$\tilde{G}_{dc} = \begin{pmatrix} \tilde{G}_L & 0 & 0 \\ 0 & \tilde{G}_C & 0 \\ 0 & 0 & \tilde{G}_R \end{pmatrix}. \tag{2.87}$$

Then interaction between the three regions is introduced via

$$\tau = \begin{pmatrix} 0 & \tau_{LC} & 0 \\ \tau_{CL} & 0 & \tau_{CR} \\ 0 & \tau_{RC} & 0 \end{pmatrix}, \tag{2.88}$$

leading to the full coupled Hamiltonian $H_c = H_{dc} + \tau$ and the fully coupled Green function

$$G_c = [z - H_{dc} - \tau]^{-1} = \begin{pmatrix} G_{LL} & G_{LC} & G_{LR} \\ G_{CL} & G_{CC} & G_{CR} \\ G_{RL} & G_{RC} & G_{RR} \end{pmatrix}. \tag{2.89}$$

By solving the linear equation system we can write:

$$G_{CC} = [z - h_C - \tau_{CL}\tilde{G}_L\tau_{LC} - \tau_{CR}\tilde{G}_R\tau_{RC}]^{-1}. \tag{2.90}$$

Or alternatively by defining the self-energies

$$\Sigma = \Sigma_L + \Sigma_R \tag{2.91}$$

$$\Sigma_L = \tau_{CL}\tilde{G}_L\tau_{LC} \tag{2.92}$$

$$\Sigma_R = \tau_{CR}\tilde{G}_R\tau_{RC}, \tag{2.93}$$

we can summarize to

$$G_{CC} = [z - h_C - \Sigma]^{-1}, \tag{2.94}$$

and write down the Dyson equation

$$G_{CC} = \tilde{G}_C + \tilde{G}_C\Sigma_L G_{CC} + \tilde{G}_C\Sigma_R G_{CC}. \tag{2.95}$$

Another related quantity is the broadening function

$$\Gamma = \Gamma_L + \Gamma_R \tag{2.96}$$

$$\Gamma_L = i(\Sigma_L - \Sigma_L^\dagger) \tag{2.97}$$

$$\Gamma_R = i(\Sigma_R - \Sigma_R^\dagger), \tag{2.98}$$

which describes the coupling of the device to the leads. When these quantities are known, it is possibly [68] to calculate the transmission probability of an electron $T(E)$ at the energy E using

$$T(E) = \mathrm{Tr}\left[G_{CC}(E)\Gamma_L(E)G_{CC}^\dagger(E)\Gamma_\mathrm{R}(E)\right]. \tag{2.99}$$

As further explained in reference [86] this description cannot be directly applied to the KKR method, since we have no way to decouple the system in such a way that the decoupled Green function $\tilde{G}_{dc}$ has absolute zero coupling between the center region and the left and right regions. However as we saw in the previous section 2.2.10 regarding the decimation approach, the introduction of the repulsive reference potential V_R leads to a Green function G_R, where at least the two lead regions are not directly coupled anymore. In a similar way we can now introduce a general repulsive potential V^{dc} and add it on top of the physical potential V. When G is the fully coupled physical Green function, and $\tilde{G}_{dc}$ now the Green function for the artificial potential $V^{dc} + V$, we can write in good approximation

$$G = \tilde{G}_{dc} + \tilde{G}_{dc}V_L^{dc}\tilde{G}_{dc}V_L^{dc}G + \tilde{G}_{dc}V_R^{dc}\tilde{G}_{dc}V_R^{dc}G. \tag{2.100}$$

This equation has the same structure as 2.95, which allows us to identify the self energies,

$$\Sigma_L = V_L^{dc}\tilde{G}_{dc}V_L^{dc} \tag{2.101}$$

$$\Sigma_R = V_R^{dc}\tilde{G}_{dc}V_R^{dc}, \tag{2.102}$$

so we can as well write

$$G = \tilde{G}_{dc} + \tilde{G}_{dc}\Sigma_L G + \tilde{G}_{dc}\Sigma_R G. \tag{2.103}$$

Now we take the expressions of the Green function in terms of the structural Green function from equation 2.49 for the fully coupled physical system and for the decoupled system,

$$G(\vec{r}_n, \vec{r}_{n'}; E) = \delta_{nn'} g_S(\vec{r}_n, \vec{r}_{n'}; E) + \sum_{LL'} R^n_L(\vec{r}_n; E) G^{nn'}_{LL'}(E) R^{n'}_{L'}(\vec{r}_{n'}; E) \tag{2.104}$$

$$G(\vec{r}_n, \vec{r}_{n'}; E)_{dc} = \delta_{nn'} g_{dc,S}(\vec{r}_n, \vec{r}_{n'}; E) + \sum_{LL'} R^n_{dc,L}(\vec{r}_n; E) G^{nn'}_{dc,LL'}(E) R^{n'}_{dc,L'}(\vec{r}_{n'}; E) \tag{2.105}$$

and their respective 2D fourier transformed structural Green functions $G^{\mu\mu'}_{LL'}(\vec{k}_\parallel, E)$ and $G^{\mu\mu'}_{dc,LL'}(\vec{k}_\parallel, E)$. By inserting these into equation 2.99, the expression for the transmission can be written as

$$T(\vec{k}_\parallel, E) = \lim_{z \to E} \operatorname{Tr}\left[G^{\nu'\mu}(\vec{k}_\parallel, z)\gamma^{\mu\mu'}_L(\vec{k}_\parallel, z, z^*)G^{\mu'\nu}(\vec{k}_\parallel, z^*)\gamma^{\nu\nu'}_R(\vec{k}_\parallel, z^*, z)\right], \tag{2.106}$$

where the angular momentum indices L are hidden for clarity. Note that the indices $\mu, \mu' \in L$ and $\nu, \nu' \in R$ only run over the atoms in their respective outer part of the center region, which are sketched as C_L and C_R in figure 2.2. As explained in [86], it is possible to show that we can write the γ matrices using the regular t-matrix of the decoupling potential

$$\Delta t^\nu(z) = \int R^{nu}_{dc}(\vec{r}, z)^\times V^{nu}_{dc}(\vec{r}) R^{nu}(\vec{r}, z) \tag{2.107}$$

and a modified t-matrix

$$\Delta\tilde{t}^\nu(z, z^*) = \int R^{nu}_{dc}(\vec{r}, z)^\times V^{nu}_{dc}(\vec{r}) R^{nu}(\vec{r}, z^*) \tag{2.108}$$

as

$$\begin{aligned} -i\gamma^{\nu\nu'}_R(\vec{k}_\parallel, z^*, z) =& \delta_{\nu\nu'}(-\Delta\tilde{t}^\nu(z, z^*)^* + \Delta\tilde{t}^\nu(z, z^*)^T) \\ &+ \Delta\tilde{t}^\nu(z, z^*)^* G^{\nu\nu'}_{dc}(\vec{k}_\parallel, z)\Delta t^\nu(z)^T \\ &- \Delta t^\nu(z)^* G^{\nu\nu'}_{dc}(\vec{k}_\parallel, z^*)\Delta\tilde{t}^\nu(z, z^*)^T), \end{aligned} \tag{2.109}$$

again with $\nu, \nu' \in R$. The other gamma matrix $-i\gamma^{\mu\mu'}_L(\vec{k}_\parallel, z, z^*)$ can be calculated analogously with $\mu, \mu' \in L$. It turns out [86] that the required structural Green function $G^{\nu\nu'}_{dc}(\vec{k}_\parallel, z)$ of the decoupled system is identical to the surface Green function, which drops out as an intermediate step from the decimation technique explained in subsection 2.2.10, and it must not be confused with the Green function of the reference system G_R. Note that the γ matrices are independent from any structures in the center region, which are sufficiently far away from the regions R and L. By using $G(z^*) = G^\dagger(z)$ we can as well write

$$T(\vec{k}_\parallel, E) = \lim_{z\to E} \mathrm{Tr}\left[G^{\nu'\mu}(\vec{k}_\parallel, z)\gamma_L^{\mu\mu'}(\vec{k}_\parallel, z, z^*)G^{\mu'\nu,\dagger}(\vec{k}_\parallel, z)\gamma_R^{\nu\nu'}(\vec{k}_\parallel, z^*, z)\right]. \qquad (2.110)$$

Now we finally have all tools at hand to calculate transmissions through 2D structures in the KKR method.

2.4 Specular and diffusive transport in supercells

When investigating electronic transport phenomena, it is possible to gain a better understanding by analyzing the $\vec{k}_\parallel$-resolved transmission [22, 87]. This information is lost in systems where translational invariance is broken by local structures such as defects, since in these cases, the Brillouin zone of the underlying lattice can no longer be used. Nevertheless, in most cases of interest, the structure that breaks translational invariance is limited to a small region of the center or device part of the transport cell. This situation is sketched in figure 2.2, where the structure that breaks translational invariance is indicated as a general disturbance. For example, in this work, we will take a look at magnetic skyrmions that exist only in a very thin layer embedded within a large, otherwise not even magnetized center region. This limitation of disturbance to the center region means that the electronic states in the leads are still bulk-like, and the transmission can be projected onto the Brillouin zones of both leads. The idea is that instead of a bulk transmission $T(\vec{k}_\parallel)$, we can still define a transmission $T(\vec{k}_\parallel, \vec{k}'_\parallel)$, which allows $\vec{k}_\parallel$ scattering between the leads. This transmission can be further decomposed into a $\vec{k}_\parallel$-conserving (specular) and a $\vec{k}_\parallel$-scattering (diffusive) contribution, where the latter is defined for each lead separately.

A similar method was already proposed in [88] for the Landauer-Büttiker formalism within KKR, where the influence of a small oxygen concentration at the Fe/MgO interface was investigated using supercells. Another related work was published by Drchal et al. [89] for the tight-binding linear muffin-tin orbital (TB-LMTO) method, but it is not directly applicable to the KKR method. While chemical disorder can be treated more accurately using CPA with vertex corrections [86], which also allows to obtain a $\vec{k}_\parallel$-transmission map, the supercell method is necessary for handling ordered structures like phonons, domain walls, or skyrmions. This is why the approach presented here was developed.

In the first part of this section, I explain the original derivation by Drchal et al. [89], which Czerner [90] adapted to the KKR method and implemented in the KKR code that I used. In the second part of this section, I demonstrate the method by applying it to iron bulk and iron supercells containing either some small atomic displacements or some non-collinear structure.

2.4.1 Supercell basis states

Guided by [89], we consider a 2D lattice with lattice vectors $\vec{a}_1$ and $\vec{a}_2$ and the corresponding reciprocal lattice vectors $\vec{b}_1$ and $\vec{b}_2$. Now, assume we want to calculate the transmission through a structure embedded in a supercell with lattice vectors

$$\begin{aligned} \vec{A}_1 &= M_1\vec{a}_1 \\ \vec{A}_2 &= M_2\vec{a}_2. \end{aligned} \tag{2.111}$$

with natural numbers M_1 and M_2. Then the supercell contains $M = M_1M_2$ atoms in total, which are located at

$$\vec{t}_n = n_1\vec{a}_1 + n_2\vec{a}_2 \tag{2.112}$$

with the compound index

$$n = (n1, n2), 0 \leq n_i \leq M_i - 1. \tag{2.113}$$

The reciprocal lattice vectors of the supercell are $\vec{B}_1 = \vec{b}_1/M_1$ and $\vec{B}_2 = \vec{b}_2/M_2$. As sketched in figure 2.3, we can then map any reciprocal vector $\vec{k}$ from the large Brillouin zone of the parent lattice (BZ) to a unique reciprocal vector $\vec{k}$ in the small supercell Brillouin zone (SCBZ) by adding a linear combination of the supercell's reciprocal lattice vectors:

$$\vec{k}_{\|} = \vec{q}_{\|} + \vec{Q}_j, \tag{2.114}$$

with

$$\vec{Q}_j = j_1\vec{B}_1 + j_2\vec{B}_2, \tag{2.115}$$

where we use another compound index

$$j = (j1, j2), 0 \leq j_i \leq M_i - 1. \tag{2.116}$$

For simplicity, the angular momentum indices and the indices regarding the atoms within the parent unit cell are omitted. According to the Bloch theorem, we can write the basis

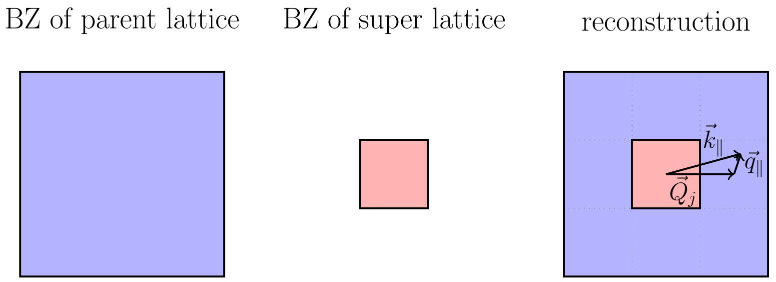

Figure 2.3: Reciprocal lattice vectors $\vec{Q}$ of the supercell connect points $\vec{k}_\parallel$ in the Brillouin zone of the parent lattice with points $\vec{q}_\parallel$ in the Brillouin zone of the supercell.

states of the parent lattice as

$$|\vec{k}_\parallel\rangle = \frac{1}{\sqrt{N_\parallel}} \sum_{\vec{R}} \exp(i\vec{k}_\parallel \cdot \vec{R})\, |\vec{R}\rangle \tag{2.117}$$

Analogously, we can write the basis states of the supercell as

$$|\vec{q}_\parallel\rangle = \frac{1}{\sqrt{N_\parallel^{\mathrm{SC}}}} \sum_{\vec{R}^{\mathrm{SC}}} \exp(i\vec{q}_\parallel \cdot \vec{R}^{\mathrm{SC}})\, |\vec{R}^{\mathrm{SC}}\rangle \tag{2.118}$$

with

$$\vec{R} = m_1\vec{A}_1 + m_2\vec{A}_2 + \vec{t}_n \tag{2.119}$$

and

$$\vec{R}^{\mathrm{SC}} = m_1\vec{A}_1 + m_2\vec{A}_2. \tag{2.120}$$

where $m_1, m_2 \in \mathbb{Z}$, $N_\parallel$ is the number of atoms in the plane and $N_\parallel^{\mathrm{SC}} = \frac{N_\parallel}{M}$. The vector $\vec{t}_n$ leads to the site $\vec{R}$ within the larger supercell. We can then convert between the two bases using the relations

$$\begin{aligned} |\vec{k}_\parallel\rangle &= \frac{1}{\sqrt{M}} \sum_{n=1}^{M} \exp(i\vec{Q}_j \cdot \vec{t}_n)\, |n\vec{q}_\parallel\rangle \\ |n\vec{q}_\parallel\rangle &= \frac{1}{\sqrt{M}} \sum_{j=1}^{M} \exp(-i\vec{Q}_j \cdot \vec{t}_n)\, |\vec{k}_\parallel\rangle\,. \end{aligned} \tag{2.121}$$

2.4.2 Unfolding the transmission map

When calculating the transmission through the supercell, we evaluate equation 2.110, which then reads

$$T(\vec{q}_\parallel) = \mathrm{Tr}\left[G(\vec{q}_\parallel)\gamma_L(\vec{q}_\parallel)G^\dagger(\vec{q}_\parallel)\gamma_R(\vec{q}_\parallel)\right]. \tag{2.122}$$

When considering a supercell where the translational symmetry-breaking structure is limited to the middle of the center region, we can directly see from the expression 2.109 for the γ matrices that the γ-matrices are unaffected by this translational symmetry-breaking structure and can therefore still be written as $\gamma_L(\vec{k}_\parallel)$ and $\gamma_R(\vec{k}'_\parallel)$. It is only $G(\vec{q}_\parallel)$ which cannot be written as $G(\vec{k}_\parallel)$ anymore. To unfold $\gamma_L(\vec{q}_\parallel)$ to $\gamma_L(\vec{k}_\parallel)$, we basically just convert between the two basis sets using the relations 2.121:

$$
\begin{aligned}
\gamma_L(\vec{k}_\parallel) &= \langle \vec{k}_\parallel | \hat{\gamma}_L | \vec{k}_\parallel \rangle \\
&= \langle \vec{k}_\parallel | \sum_{n'\vec{q}'_\parallel n''\vec{q}''_\parallel} |n'\vec{q}'_\parallel\rangle \; \underbrace{\langle n'\vec{q}'_\parallel | \hat{\gamma}_L | n''\vec{q}''_\parallel \rangle}_{=\gamma_L(\vec{q}'_\parallel)_{n'n''}\delta(\vec{q}'_\parallel - \vec{q}''_\parallel)} \; \langle n''\vec{q}''_\parallel | \vec{k}_\parallel \rangle \\
&= \sum_{n''n'\vec{q}'_\parallel} \langle \vec{k}_\parallel | n'\vec{q}'_\parallel \rangle \, \gamma_L(\vec{q}_\parallel)_{n'n''} \, \langle n''\vec{q}'_\parallel | \vec{k}_\parallel \rangle \\
&= \sum_{n'n''\vec{q}'_\parallel} \frac{1}{M} \sum_{n_1=1}^{M} \langle n_1\vec{q}_\parallel | n'\vec{q}'_\parallel \rangle \, e^{-i\vec{Q}_j\vec{t}_{n_1}} \gamma_L(\vec{q}_\parallel)_{n'n''} \sum_{n_2=1}^{M} \langle n''\vec{q}'_\parallel | n_2\vec{q}_\parallel \rangle \, e^{+iQ_j\vec{t}_{n_2}} \\
&= \sum_{n'n''} \frac{1}{M} e^{i\vec{Q}_j(\vec{t}_{n''}-\vec{t}_{n'})} \gamma_L(\vec{q}_\parallel)_{n'n''}
\end{aligned}
\tag{2.123}
$$

Regarding G, we know that it now describes scattering by entire reciprocal lattice vectors $\vec{Q}_j$ of the supercell. Therefore, we can write $G(\vec{k}_\parallel, \vec{k}'_\parallel)$ with $\vec{k}_\parallel = \vec{q}_\parallel + \vec{Q}_j$ and $\vec{k}'_\parallel = \vec{q}_\parallel + \vec{Q}_{j'}$. Similarly to how we unfolded $\gamma_L(\vec{q}_\parallel)$ to $\gamma_L(\vec{k}_\parallel)$, we can unfold $G(\vec{q}_\parallel)$ to $G(\vec{k}_\parallel, \vec{k}'_\parallel)$ by using the relations 2.121 between the two basis sets:

$$
\begin{aligned}
G(\vec{k}'_\parallel, \vec{k}_\parallel) &= \langle \vec{k}'_\parallel | \hat{G} | \vec{k}_\parallel \rangle \\
&= \langle \vec{k}'_\parallel | \sum_{n'\vec{q}'_\parallel n''\vec{q}''_\parallel} |n'\vec{q}'_\parallel\rangle \; \underbrace{\langle n'\vec{q}'_\parallel | \hat{G} | n''\vec{q}''_\parallel \rangle}_{=G(\vec{q}'_\parallel)_{n'n''}\delta(\vec{q}'_\parallel - \vec{q}''_\parallel)} \; \langle n''\vec{q}''_\parallel | \vec{k}_\parallel \rangle \\
&= \sum_{n''n'\vec{q}'_\parallel} \langle \vec{k}'_\parallel | n'\vec{q}'_\parallel \rangle \, G(\vec{q}_\parallel)_{n'n''} \, \langle n''\vec{q}'_\parallel | \vec{k}_\parallel \rangle \\
&= \sum_{n'n''\vec{q}'_\parallel} \frac{1}{M} \sum_{n_1=1}^{M} \langle n_1\vec{q}_\parallel | n'\vec{q}'_\parallel \rangle \, e^{-i\vec{Q}_{j'}\vec{t}_{n_1}} G(\vec{q}_\parallel)_{n'n''} \sum_{n_2=1}^{M} \langle n''\vec{q}'_\parallel | n_2\vec{q}_\parallel \rangle \, e^{+iQ_j\vec{t}_{n_2}} \\
&= \sum_{n'n''} \frac{1}{M} e^{i(\vec{Q}_j\vec{t}_{n''}-\vec{Q}_{j'}\vec{t}_{n'})} G(\vec{q}_\parallel)_{n'n''}
\end{aligned}
\tag{2.124}
$$

Analogously, we can write

$$
\gamma_R(\vec{k}'_\parallel) = \sum_{n'n''} \frac{1}{M} e^{i\vec{Q}_{j'}(\vec{t}_{n''}-\vec{t}_{n'})} \gamma_R(\vec{q}_\parallel)_{n'n''}, \tag{2.125}
$$

and

$$G^{\dagger}(\vec{k}_{\|},\vec{k'}_{\|}) = \sum_{n'n''} \frac{1}{M} e^{i(\vec{Q}_{j'}\vec{t}_{n''}-\vec{Q}_{j}\vec{t}_{n'})} G^{\dagger}(\vec{q}_{\|})_{n'n''}. \tag{2.126}$$

To transform the products $G(\vec{k'}_{\|},\vec{k}_{\|})\gamma_L(\vec{k}_{\|})$ and $G^{\dagger}(\vec{k}_{\|},\vec{k'}_{\|})\gamma_R(\vec{k'}_{\|})$, a naive approach might be to multiply the previously obtained expressions. However, this would eventually lead to an unnecessary complicated expression for the transmission. We can achieve a simpler expression by writing:

$$\begin{aligned}
G(\vec{k'}_{\|},\vec{k}_{\|})\gamma_L(\vec{k}_{\|}) &= \langle \vec{k'}_{\|}|\hat{G}\hat{\gamma}_L|\vec{k}_{\|}\rangle \\
&= \langle \vec{k'}_{\|}|\hat{G}\hat{I}\hat{\gamma}_L|\vec{k}_{\|}\rangle \\
&= \sum_{n''\vec{q''}_{\|}} \langle \vec{k'}_{\|}|\hat{G}|n''\vec{q''}_{\|}\rangle \underbrace{\langle n''\vec{q''}_{\|}|\hat{\gamma}_L|\vec{k}_{\|}\rangle}_{\propto\delta(\vec{q''}_{\|}-\vec{q}_{\|})} \\
&= \sum_{n''} \langle \vec{k'}_{\|}|\hat{G}|n''\vec{q}_{\|}\rangle \, \langle n''\vec{q}_{\|}|\hat{\gamma}_L|\vec{k}_{\|}\rangle \\
&= \sum_{n''} \frac{1}{M} \sum_{nn'} e^{-i\vec{Q}_{j'}\vec{t}_{n'}} \, \langle n'\vec{q}_{\|}|\hat{G}|n''\vec{q}_{\|}\rangle \, \langle n''\vec{q}_{\|}|\hat{\gamma}_L|n\vec{q}_{\|}\rangle \, e^{+i\vec{Q}_{j}\vec{t}_{n}} \\
&= \frac{1}{M} \sum_{nn'} e^{i(\vec{Q}_{j}\vec{t}_{n}-\vec{Q}_{j'}\vec{t}_{n'})} \sum_{n''} G(\vec{q}_{\|})_{n'n''}\gamma_L(\vec{q}_{\|})_{n''n} \\
&= \frac{1}{M} \sum_{nn'} e^{i(\vec{Q}_{j}\vec{t}_{n}-\vec{Q}_{j'}\vec{t}_{n'})} \{G(\vec{q}_{\|})\gamma_L(\vec{q}_{\|})\}_{n'n}
\end{aligned} \tag{2.127}$$

Analogously, we can write for the other product:

$$G^{\dagger}(\vec{k}_{\|},\vec{k'}_{\|})\gamma_R(\vec{k'}_{\|}) = \sum_{nn'} \frac{1}{M} e^{i(\vec{Q}_{j'}\vec{t}_{n'}-\vec{Q}_{j}\vec{t}_{n})} \{G^{\dagger}(\vec{q}_{\|})\gamma_R(\vec{q}_{\|})\}_{nn'} \tag{2.128}$$

Finally, by multiplying these two expressions, we can write down an expression for the unfolded transmission:

$$\begin{aligned}
T(\vec{k}_{\|},\vec{k'}_{\|}) &= \mathrm{Tr}\left[G(\vec{k'}_{\|},\vec{k}_{\|})\gamma_L(\vec{k}_{\|})G^{\dagger}(\vec{k}_{\|},\vec{k'}_{\|})\gamma_R(\vec{k'}_{\|})\right] \\
&= \frac{1}{M^2} \sum_{n_1n_2n_3n_4} e^{i\vec{Q}_{j}(\vec{t}_{n_2}-\vec{t}_{n_3})} e^{i\vec{Q}_{j'}(\vec{t}_{n_4}-\vec{t}_{n_1})} \\
&\quad \cdot \mathrm{Tr}\left[\{G(\vec{q}_{\|})\gamma_L(\vec{q}_{\|})\}_{n_1n_2}\{G^{\dagger}(\vec{q}_{\|})\gamma_R(\vec{q}_{\|})\}_{n_3n_4}\right]
\end{aligned} \tag{2.129}$$

2.4.3 Application to Iron

To demonstrate the method, we apply it to iron bulk. Iron has a ferromagnetic ground state, which can be separated into a majority (here up ↑) and a minority (here down ↓) spin channel. The following results are plotted for both spin channels. All calculations are carried out using our screened Korringa-Kohn-Rostoker (KKR) code [64, 65] within

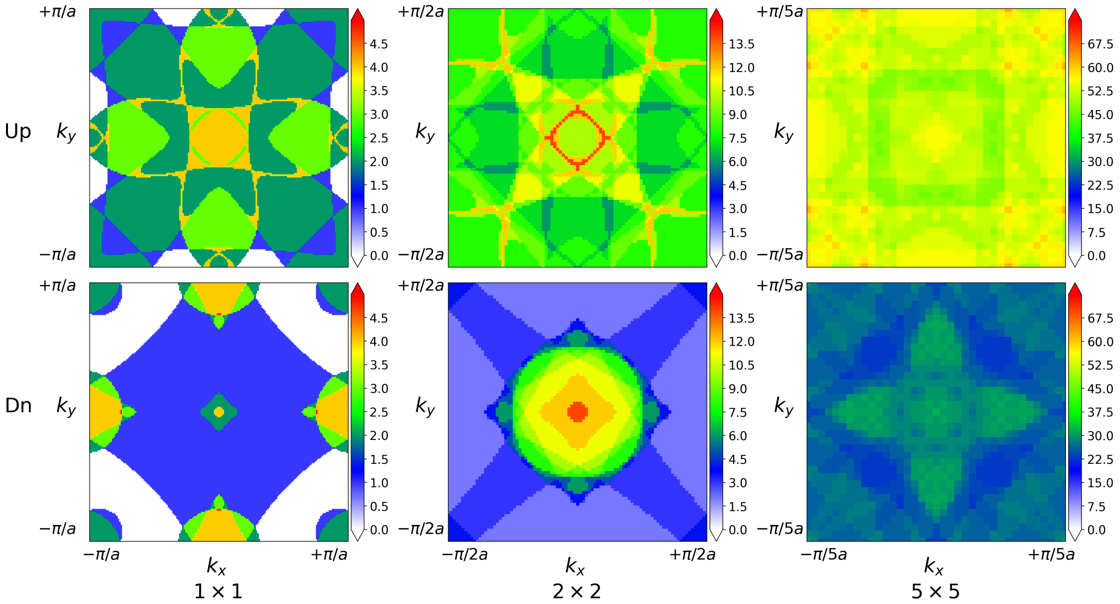

Figure 2.4: Transmittance maps through pure iron bulk for three different cell sizes.

the atomic sphere approximation (ASA). The potential of pure iron was calculated in a self-consistent manner using an LDA exchange-correlation potential and an angular momentum cut-off of $l_{\text{max}} = 3$. The potential for the perturbed cells was obtained by shifting or rotating the pure iron potential without applying further self-consistent iterations. Electronic transport was then calculated using the non-equilibrium Green function method (NEGF), as explained in section 2.3. In this step, we used an angular momentum cut-off of $l_{\text{max}} = 2$. For Brillouin zone sampling for different supercell sizes of 1×1, 2×2, 5×5, k-point meshes of 180×180, 90×90, and 36×36 were used, respectively. When unfolding the transmission maps, we used equation 2.129 to calculate $T(\vec{k}_{\parallel}, \vec{k}'_{\parallel})$, which is then used to compute the specular and diffusive transmission:

$$\begin{aligned} T_{\text{spec}}(k_{\parallel}) &= T(k_{\parallel}, k_{\parallel}) \\ T_{\text{diff}}(k_{\parallel}) &= \sum_{k'_{\parallel} \neq k_{\parallel}} T(k_{\parallel}, k'_{\parallel}) \end{aligned} \tag{2.130}$$

In this case, the diffusive part is defined for the left lead. This distinction becomes important when the structure is asymmetric with respect to the transport direction, especially when the leads are made of different materials. In such a case, the diffusive contributions on both sides may be viewed separately.

When calculating the transmission for pristine iron bulk for different in-plane supercells, the overall transmission is always the same. The $\vec{k}_{\parallel}$ dependent transmission, shown in figure 2.4, gets folded into the corresponding smaller Brillouin-zone as the supercell size is increased. When applying the decomposition in this situation, the diffusive part is always zero, while the specular contribution is identical to the transmission map of the 1×1 cell.

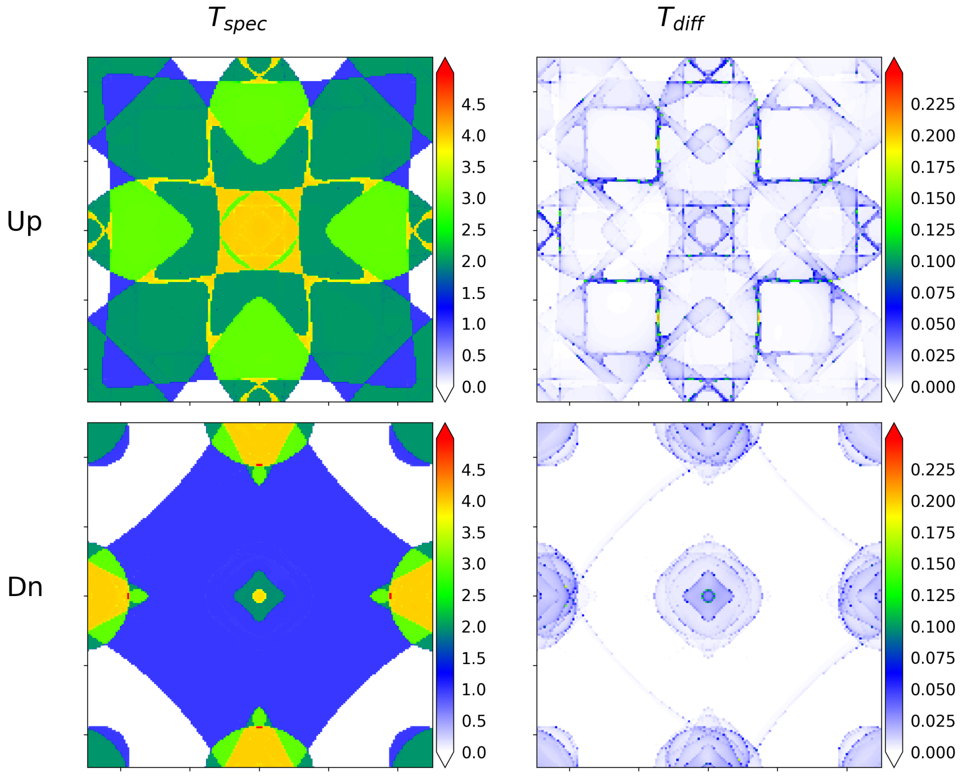

Figure 2.5: Transmittance maps through a 2×2 iron bulk supercell with random atomic displacements of about 1% of the lattice constant in one layer.

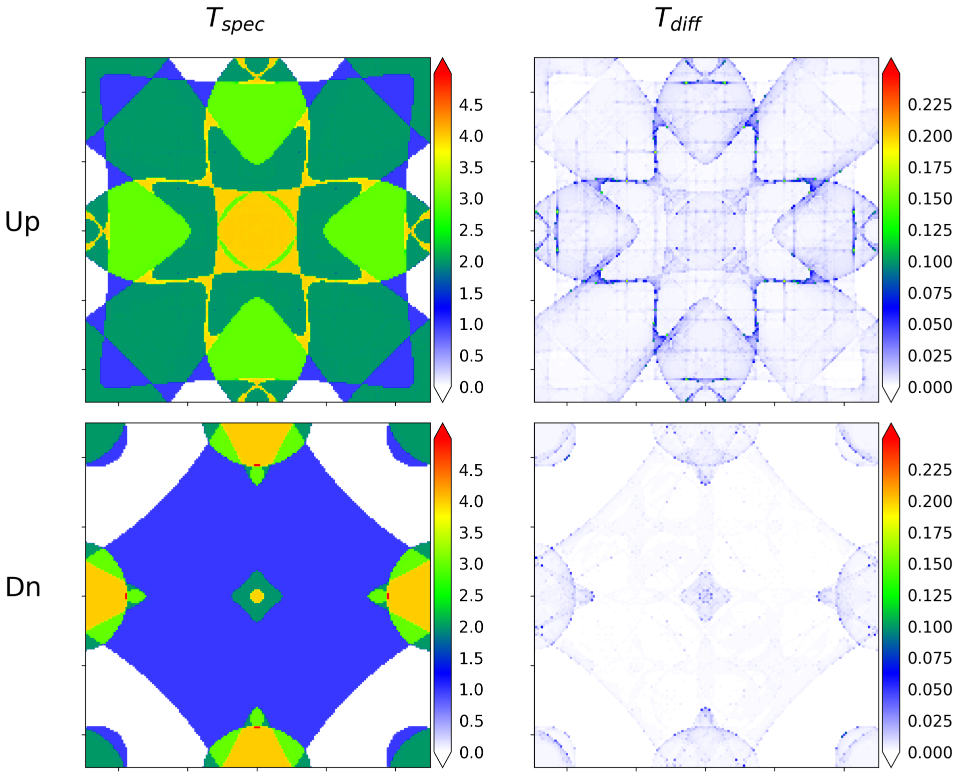

Figure 2.6: Transmittance maps through a 5×5 iron bulk supercell with random atomic displacements of about 1% of the lattice constant in one layer.

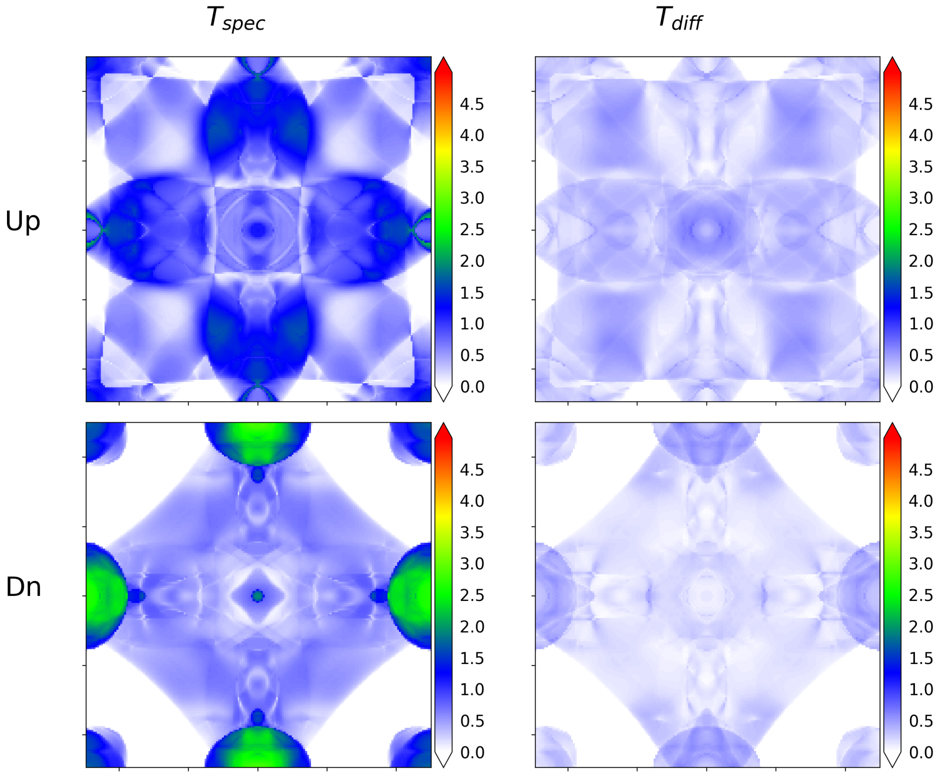

Figure 2.7: Transmittance maps through a 2×2 iron bulk supercell with a random non-collinear structure in one layer.

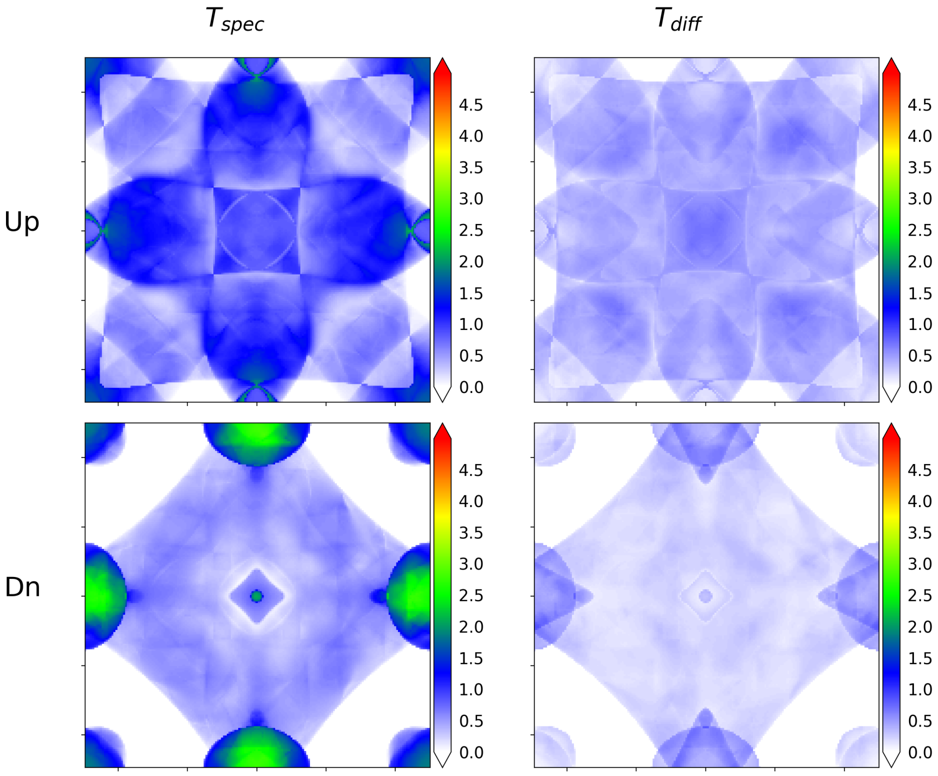

Figure 2.8: Transmittance maps through a 5 × 5 iron bulk supercell with a random non-collinear structure in one layer.

When the in-plane translational invariance is broken in the device region, the situation changes. This is tested by applying two kinds of perturbation. First, we randomly displace one layer of iron atoms in the center of the device region. This type of perturbation may be used to study the impact of phonons on transport. It could serve as a complementary approach to the work in reference [91]. The results for this situation in the 2×2 and 5×5 in-plane supercell are shown in figures 2.5 and 2.6, respectively. The impact of the atomic displacement is rather small in this case, which means that the specular contribution and the transmission through the unperturbed bulk material can hardly be distinguished. The diffusive part is rather small, but it is not completely zero. The largest contributions occur at the edges of the bands. The physical interpretation of this result is that the Fermi velocity in the transport direction vanishes at the edges, which means that the electrons spend more time in the vicinity of the scatterer, leading to stronger scattering effects. The influence of the supercell size is clearly visible when comparing the diffusive contribution between figures 2.5 and 2.6. In the diffusive part of the transmission through the 2×2 cell, several peculiar features are observable, particularly the asymmetry of the lines in the down part (minority) is very prominent. When the supercell size is increased from 2×2 to 5×5, these asymmetric features diminish, and the overall diffusive transmission becomes smoother. As a second type of perturbation, we impose a random non-collinear structure onto one layer of iron atoms. This perturbation has a more significant impact on the transmission maps than the atomic displacement, as can be seen in figures 2.7 and 2.8. The specular contribution to transport is much smaller than the transmission through pristine iron. The distribution of the diffusive transport also differs from that caused by atomic displacement. While the diffusive transmission in case of the displacement is mainly located at certain band edges, it is smoothly distributed across the entire bands by the non-collinear structure. The influence of the supercell size is similar for both types of perturbation. While the transmission in the small 2×2 supercell contains obvious artificial features, these features are less pronounced in case of the larger supercell. This is not the only aspect that the two examples share, which can be generalized. Most importantly, areas of the Brillouin zone with zero transmission through the bulk material also have zero transmission in the specular and diffusive case. This is because the transmission maps refer to the electronic structure of the pristine bulk materials of the leads in all cases. When the transmission through the bulk material is zero, this means that there are no states available in the leads, resulting in both diffusive and specular transmission remaining zero. If the structure consists of several different layers, the situation is slightly different, and the diffusive transmission of one lead may contain transmission contributions in parts of the Brillouin zone where the other lead provides no electronic states. This possibility becomes important later in this work.

2.5 Tunneling magnetoresistance

While the tunneling magnetoresistance effect (TMR) [20, 21] is not the main subject of this work, its underlying mechanism is crucial for understanding the effects described here. The tunneling magnetoresistance effect refers to the change in resistance through a thin insulating layer, sandwiched between two magnetic conducting leads, which occurs when the magnetization direction of one of the magnetic leads is altered. Such a structure is called a magnetic tunnel junction (MTJ), since the electric current needs to tunnel through the insulating barrier to pass the junction. A simple approach to explain the effect is the Julliere model [92], which assumes that the total conductance is proportional to the product of the available number of charge carriers in both leads. As explained in [93], there are two independent spin channels in a parallel or antiparallel magnetic alignment, whose carriers do not intermix and have to be treated separately. The conductance at parallel alignment can be described as

$$I^{\mathrm{P}} = I^{\uparrow\uparrow} + I^{\downarrow\downarrow} \propto n_L^{\uparrow} n_R^{\uparrow} + n_L^{\downarrow} n_R^{\downarrow} \tag{2.131}$$

and at anti-parallel alignment as

$$I^{\mathrm{AP}} = I^{\uparrow\downarrow} + I^{\downarrow\uparrow} \propto n_L^{\uparrow} n_R^{\downarrow} + n_L^{\downarrow} n_R^{\uparrow}. \tag{2.132}$$

This means that a large difference between $n^{\uparrow}$ and $n^{\downarrow}$ leads to a large TMR effect. Experiments with amourphous Al_2O_3 are supporting this model [94, 95]. Later experiments with crystalline MgO barriers, however, showed much larger effects, that can not be explained within the Julliere model. These can only be explained by the symmetry filtering effect of MgO [22]. Specifically, the tunneling probability through MgO of electrons with Δ_1 symmetry is much higher than that of electrons with Δ_5, Δ_2, or $\Delta_{2'}$ symmetry. As sketched in figure 2.9, iron at E_{F} provides Δ_1 symmetry electrons only in the majority spin channel. In a parallel aligned MTJ, effectively tunneling Δ_1 electrons can enter the junction from one iron lead and exit into the other iron lead coherently. In contrast, in an anti-parallel aligned configuration, as sketched in figure 2.10, no effectively tunneling states are available. While this explanation, is of course, only exactly valid at the Γ-point in a purely crystalline structure, it has been shown [96, 97] that it remains qualitatively correct for electrons with small transverse crystal momentum $k_{\|}$. Thus, for simplicity, following Gradhand et al. [97], I will refer to electronic states which are sufficiently close to Δ_1 symmetry as Δ_1-like throughout this work.

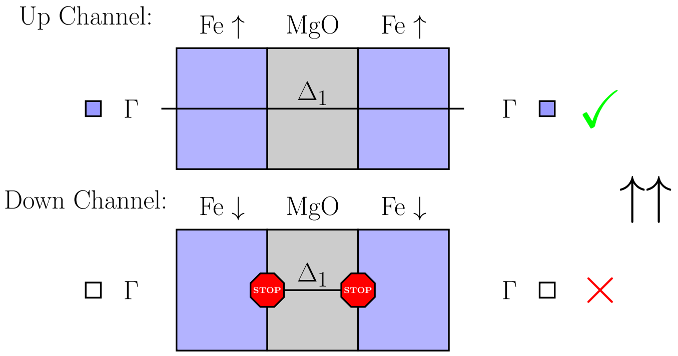

Figure 2.9: When both iron leads are parallel magnetized, the Δ_1-electrons in the majority channel can easily tunnel through the MgO into the other lead. The minority channel, on the other hand, does not provide any significant current. The sum of both, the total tunnel current, remains significant.

2.6 Tunneling anisotropic magnetoresistance

While the TMR effect relies on the relative angle of the magnetization directions of two different layers, even a change in the magnetization direction of a single magnetic layer next to an insulating barrier (see figure 2.11) can change the tunneling current through that barrier. This effect is known as the tunneling anisotropic magnetoresistance effect (TAMR) [25], because it describes an anisotropy regarding the magnetization direction. It cannot be explained non-relativistically, since in non-relativistic quantum mechanics,

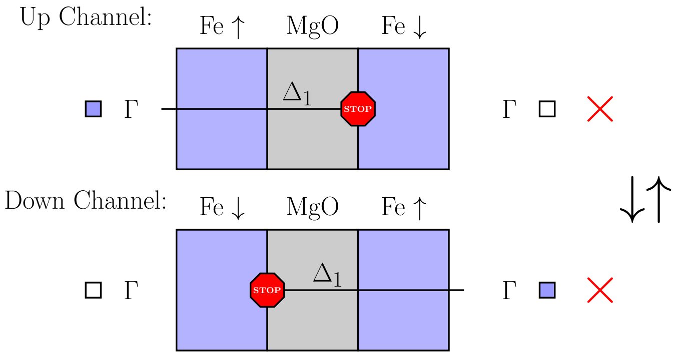

Figure 2.10: When both iron leads are antiparallel magnetized, the Δ_1-electrons from the majority channel on each side cannot enter the other respective lead on the other side of the MgO barrier. All other states are effectively filtered by the MgO barrier. The total current through the junction is very small.

spin space and real space are not coupled. It requires spin-orbit coupling (SOC), which is a term included in the relativistic Dirac equation. Typically, TAMR occurs in structures containing heavy elements which provide large SOC [98], but it turns out that a large TAMR can even be obtained without using any heavy elements [99].

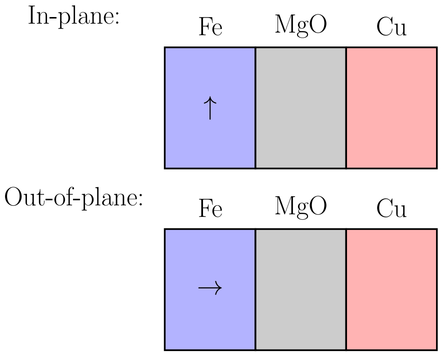

Figure 2.11: The tunneling current from the ferromagnetic Fe lead, through the MgO into the Cu lead depends on the magnetization direction of the Fe. The sketched effect is called out-of-plane TAMR. An in-plane rotation of the magnetization can lead to an in-plane TAMR effect.

2.7 Magnetic interactions

In order to accurately describe the formation of complex magnetic structures, such as skyrmions, it is important to understand the dominant terms of magnetic interaction between atoms [100, 101, 102]. A commonly used model to study magnetic interactions is the atomistic Heisenberg model, which assumes that all magnetic moments are a countable set of individual localized vectors $\vec{n}_i$ with a fixed length. The most familiar term of this model is the Heisenberg exchange interaction. The Heisenberg exchange interaction [103] Hamiltonian for atoms with magnetization direction, i.e. unit vector of the magnetic moment $\vec{n}$, is described as

$$H_{\mathrm{EXI}} = -\sum_{ij} J_{ij}\vec{n}_i \cdot \vec{n}_j. \tag{2.133}$$

Depending on the sign of J_{ij}, the interaction H_{EXI} will favor either ferromagnetism or antiferromagnetism, hence parallel or antiparallel alignment of the magnetic moments. In case of skyrmions, the Dzyaloshinskii–Moriya Interaction (DMI) [104, 105, 106] plays an important role. The DMI has its origin in spin-orbit coupling and is represented by

$$H_{\mathrm{DMI}} = -\sum_{ij} \vec{D}_{ij}(\vec{n}_i \times \vec{n}_j). \tag{2.134}$$

The DMI favors an orthogonal arrangement of neighboring spins, and thus competes with the Heisenberg exchange interaction, leading to a large variety of magnetic phenomena. The vector $\vec{D}_{ij}$ is called Dzyaloshinskii–Moriya vector. The Moriya symmetry rules [104] restrict the possible direction of the Dzyaloshinskii–Moriya vector in real systems. These rules are explained and applied to the system considered in this work in section 2.10. Another dominant term in materials with strong spin-orbit coupling is magnetocrystalline anisotropy [107], given by

$$H_{\mathrm{A}} = -\sum_{i} K(\vec{n}_i), \tag{2.135}$$

where K depends on the symmetry of the crystal structure. We can always state that magnetocrystalline anisotropy favors specific magnetization directions in a material. In crystals with a high symmetry axis, the uniaxial anisotropy term $H_{\mathrm{A,u}}$ dominates, which depends on the angle θ between $\vec{n}_i$ and the high symmetry axis. Assuming the high symmetry axis to be $\propto \vec{e}_z$ and omitting a constant, we can write [108, 109]

$$H_{\mathrm{A,u}} = -\sum_{i}(K_{u,1}n_{i,z}^2 + K_{u,2}n_{i,z}^4 + \dots), \tag{2.136}$$

which, depending on the sign of the factors, favors either an out-of-plane or in-plane magnetization direction. In cubic crystals, magnetocrystalline anisotropy can most easily be described in terms of the cosines of the angles between $\vec{n}$ and the crystal axes, which we shall call $\alpha_1, \alpha_2, \alpha_3$. The cubic anisotropy $H_{\mathrm{A,c}}$ can then, omitting a constant, be written as [108, 109]

$$H_{\mathrm{A,c}} = -\sum_{i}(K_{c,1}(\alpha_{i,1}^2\alpha_{i,2}^2 + \alpha_{i,2}^2\alpha_{i,3}^2 + \alpha_{i,3}^2\alpha_{i,1}^2) + K_{c,2}(\alpha_{i,1}^2\alpha_{i,2}^2\alpha_{i,3}^2) + \dots), \tag{2.137}$$

which, depending on the sign of the factors, either favors a magnetization direction diagonal in the cube lattice or along the cube edge axes. Interestingly, it is possible to tune anisotropy via an applied voltage, known as voltage-controlled magnetic anisotropy (VCMA) [110, 111], which can be useful when working with skyrmions [112]. Besides these three terms, we also have to consider more classic terms, such as the dipole-dipole interaction (DDI) between the atoms:

$$H_{\mathrm{DDI}} = -\frac{\mu_{\mathrm{S}}^2 \mu_0}{4\pi a^3} \sum_{i<j} \frac{3(\hat{\vec{r}}_{ij} \cdot \vec{n}_i)(\hat{\vec{r}}_{ij} \cdot \vec{n}_j) - \vec{n}_i \cdot \vec{n}_j}{|\vec{r}_{ij}|^3} \tag{2.138}$$

Here, $\hat{\vec{r}}$ are the unit vectors between the atoms with the lattice constant a, and μ_{S} is the magnetic moment of the atoms. While DDI is relatively weak on a small scale, it decays very slowly with increasing distance between the atoms, which makes it important on larger scales. When DDI from many magnetic moments is combined, it can add up to so-called stray fields, which complicate skyrmion formation and interaction [42, 113]. Due to the longe range of DDI, the shape of any macroscopic magnetized object also influences the preferred magnetization axes of the object. This effect is called shape anisotropy [114], and it adds up with the magnetocrystalline anisotropy to the total or effective magnetic anisotropy. For example, Denker et al. [115] utilized the control of shape anisotropy to create skyrmions in a thin ferromagnetic layer. When the ferromagnetic layer was too thin, uniaxial magnetocrystalline anisotropy, which preferred an out-of-plane magnetization, dominated and suppressed the formation of skyrmions. However, increasing the ferromagnetic layer thickness enhanced shape anisotropy, which preferred in-plane magnetization. This effect added up with uniaxial magnetocrystalline anisotropy, resulting in zero effective magnetic anisotropy at a specific thickness, thereby allowing the formation of skyrmions. In other cases [116], a non-zero effective magnetic anisotropy is important for the formation of skyrmions, because it suppresses helical states that would appear otherwise.

Lastly, the influence of an external magnetic field $\vec{B}_{\mathrm{ext}}$ on atoms in a material is described by the Zeeman Hamiltonian

$$H_{\mathrm{Z}} = -\mu_{\mathrm{S}} \sum_i \vec{B}_{\mathrm{ext}} \cdot \vec{n}_i, \tag{2.139}$$

which is often [27], but not always [117], required for the formation of skyrmions. This list is not comprehensive, and there are many others terms, like biquadratic exchange [118], which might be considered in a more accurate analysis. Theoretically, an exact description of the magnetic interactions requires an infinite expansion of multispin interactions. For example, Singer et al. [119] used an expansion of up two 20 terms to achieve a very accurate description of bulk iron.

2.8 Topological charge

While the above atomistic formulas describe magnetic interactions between single atoms, the micromagnetic approximation [120, 121, 122], based on the Landau–Lifshitz–Gilbert equation, describes the same interactions in a continuous way. It neglects the atomic structure of the material, which reduces the computational cost for simulating larger systems. When this model is used to describe a system with DMI, and the magnetization in a small spot of the material is inverted with respect to the rest of the material, it can be shown that the energy required to continuously evolve the magnetization such that this spot of inverted magnetization is eliminated and the entire system becomes homogeneously magnetized is infinite. Since this infinite barrier cannot be bypassed for topological reasons, such a structure is said to be topologically protected. This topologically protected quasi-particle can be associated with a topological charge Q [123], which is an integer number and cannot be altered with a finite amount of energy within the micromagnetic model. The topological charge can be calculated for a two dimensional system using

$$Q = \frac{1}{4\pi} \int \vec{m} \cdot \left(\frac{\partial \vec{m}}{\partial x} \times \frac{\partial \vec{m}}{\partial y} \right) d^2x. \tag{2.140}$$

The infinite energy barrier, however, is a result of the micromagnetic model, and in a real physical system, this energy is, of course not infinite. Since this topological concept was first developed by Tony Skyrme [4] in the context of nuclear physics, objects with a topological charge of $Q = \pm 1$ are called skyrmions [27]. In general, all kinds of magnetic structures can be characterized by their topological charge, where topologically unstable objects with $Q = 0$ are often referred to as trivial bubbles.

2.9 Magnetic structures

Due to the various competing interactions, a variety of magnetic structures may occur. The magnetization in skyrmion-like structures [124, 125, 126] can be described as

$$\vec{m}(\vec{r}) = \begin{pmatrix} \cos\Phi(\vec{r}) \sin\Theta(\vec{r}) \\ \sin\Phi(\vec{r}) \sin\Theta(\vec{r}) \\ \cos\Theta(\vec{r}) \end{pmatrix}, \tag{2.141}$$

with $\Phi(\phi) = \nu\phi + \eta$. When the skyrmion-like structure is centered around the origin and cylindrical coordinates $\vec{r} = (r\cos\phi, r\sin\phi)$ are used. ν is called the vorticity, and η is the helicity. When the magnetization in the center of the structure (let's assume $+\vec{e}_z$) and in the surrounding region is fixed (let's assume -$\vec{e}_z$) [124], within the bounds of equation 2.141, the vorticity determines the topological charge, and the helicity is linked to the spin texture. The structure with $(Q, \nu, \eta) = (1, 1, \pm\pi/2)$ is called a Bloch skyrmion, and the structure with $(Q, \nu, \eta) = (1, 1, 0 \text{ or } \pi)$ is called a Néel skyrmion (see figure 2.12). Both structures could also exist in an antiferromagnetic host material, where they are referred to as antiferromagnetic skyrmions [127] (see figure 2.13). Any structure with $(-1, -1, \eta)$ is called antiskyrmion. The antiskyrmion [128], along with an example of a trivial bubble are sketched in 2.14. In general, any object with a positive vorticity is called vortex, and any object with a negative vorticity is called anti-vortex. However, these terms are usually only used when the more specific topological terms do not apply [129].

In materials with easy-plane anisotropy, there are no skyrmions with radial symmetry. Instead, in such materials, a topological object with $Q = 1$ splits into two smaller objects [130], each with a vorticity, forming a vortex and an anti-vortex with a topological charge of $Q = \pm 1/2$. Deriving from the Greek word 'Μέρος', meaning part or fraction, such objects with a topological charge of $Q = \pm 1/2$ are called merons [131]. The combined object is displayed in figure 2.15 and is called a bimeron.

Since the term 'meron' is fundamentally associated with a topological charge of $Q = \pm 1/2$ and only loosely connected to in-plane skyrmions, it is also used in the literature to describe other objects with a similar half topological charge, which requires caution [29]. Besides the ferromagnetic state, another typical magnetic ground state of thin magnetic films is the helical state, which consists of stripe domains. The ends of such stripes [132], which have a topological charge of $Q = \pm 1/2$, are also merons. Consequently, short stripes could be called bimerons.

For further reading, reference [133] provides a comprehensive overview over the different magnetic objects described in the literature.

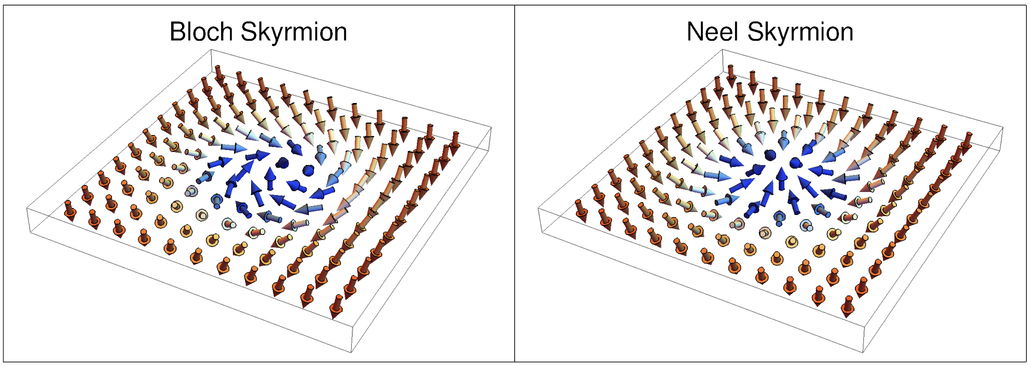

Figure 2.12: The two common types of skyrmions. The symmetry of the DMI vectors, and consequently the symmetry of the material itself, determines whether the skyrmions in a material are of Néel [6] or Bloch [7] type.

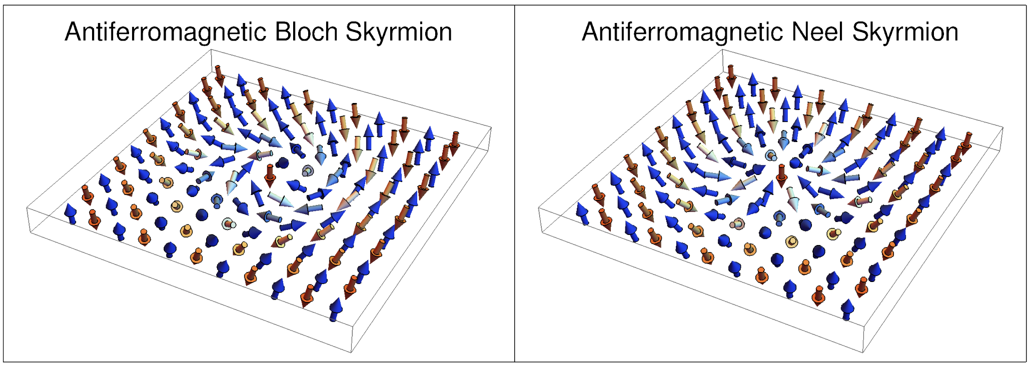

Figure 2.13: The displayed antiferromagnetic skyrmions [127] are a Néel skyrmion and a Bloch skyrmion in an antiferromagnetic material, where the magnetization in one of the sublattices is inverted.

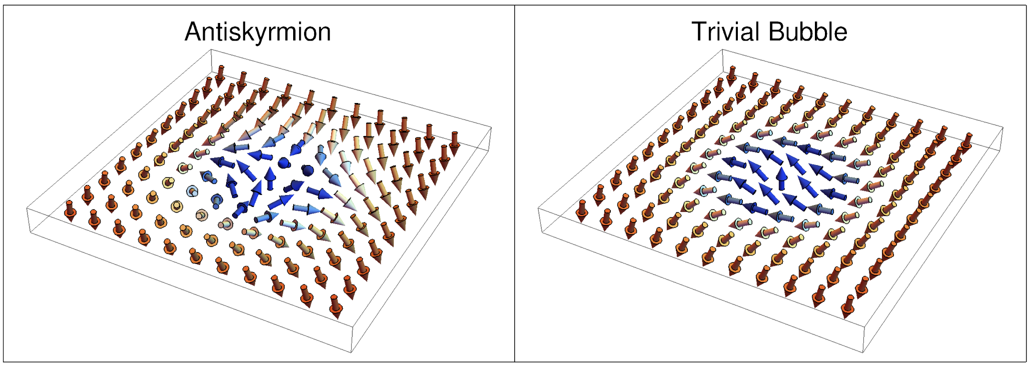

Figure 2.14: Left: An antiskyrmion [134, 128] as it could possibly exist in Fe double layers grown on a W(110) surface. Right: Any structure with $Q = 0$ is a topologically trivial bubble [135].

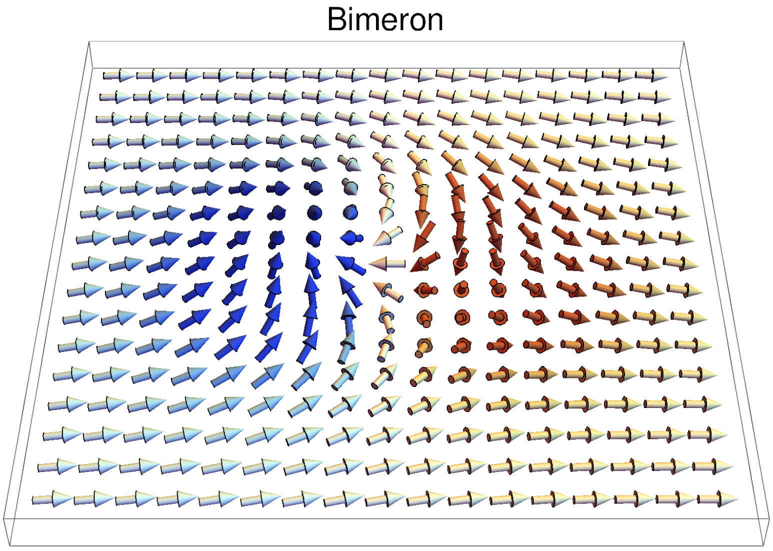

Figure 2.15: A bimeron, composed of two merons, in the sense of an in-plane skyrmion according to Göbel et al. [29].

2.10 Moriya symmetry rules

The formation of skyrmions requires a well balanced interplay of competing magnetic interactions. Of these interactions, the most important ingredient is the Dzyaloshinskii–Moriya interaction (DMI), which causes a canting of neighboring magnetic moments. The DMI requires broken inversion symmetry and is based on SOC. While DMI is present in non-centrosymmetric bulk materials [136], interfaces also break inversion symmetry and allow more flexibility in their design [137]. Besides the necessary absence of inversion symmetry, remaining symmetries, like the C_{4v} symmetry in the V/Fe/MgO/Cu system, which will be used in this work (see section 3), also restrict the possible DMI vectors. These constraints are also known as Moriya rules [104], which we can use to show that only Néel-type skyrmions may appear in our V/Fe/MgO/Cu system, while Bloch-type skyrmions are suppressed.

Consider two spins located at the positions $\vec{R}_1$ and $\vec{R}_2$. The following rules apply for the DMI vector $\vec{D}_{1,2}$:

1. If a center of inversion is located in the middle between both spins at $(\vec{R}_1 + \vec{R}_2)/2$, then: $\vec{D}_{1,2} = \vec{0}$
2. If a mirror plane perpendicular to $(\vec{R}_1 - \vec{R}_2)$ passes through the middle $(\vec{R}_1 + \vec{R}_2)/2$, then $\vec{D}_{1,2}$ is perpendicular to $(\vec{R}_1 - \vec{R}_2)$.
3. If a mirror plane includes both $\vec{R}_1$ and $\vec{R}_2$, then $\vec{D}_{1,2}$ is perpendicular to the mirror plane.
4. If a 2-fold rotation axis perpendicular to $(\vec{R}_1 - \vec{R}_2)$ passes through the middle $(\vec{R}_1 + \vec{R}_2)/2$, then $\vec{D}_{1,2}$ is perpendicular to the rotation axis.
5. If an n-fold rotation axis with $n > 1$ includes $\vec{R}_1$ and $\vec{R}_2$, then $\vec{D}_{1,2}$ is parallel to $(\vec{R}_1 - \vec{R}_2)$.

Now, we want to apply these rules on the spins of neighboring Fe atoms in the system V/Fe/MgO/Cu system. For better illustration, all mentioned planes and axes are sketched in figure 2.16. We get the following results:

1. Since this is a layered system, there is no center of inversion, so a non-zero DMI is possible.
2. There is a mirror plane M_2 (2 for the rule number) between $\vec{R}_1$ and $\vec{R}_2$, so $\vec{D}_{1,2}$ is perpendicular to $(\vec{R}_1 - \vec{R}_2)$.
3. There is also a mirror plane M_3 through $\vec{R}_1$ and $\vec{R}_2$, so $\vec{D}_{1,2}$ must be perpendicular to M_3.

4. A 2-fold rotation axis $\vec{A}_4$ (4 for the rule number) is perpendicular to $(\vec{R}_1 - \vec{R}_2)$ and the entire Fe layer, passing through the middle $(\vec{R}_1 + \vec{R}_2)/2$, so $\vec{D}_{1,2}$ must lie in the plane formed by the Fe layer.

5. There is no n-fold rotation axis with $n > 1$ that includes $\vec{R}_1$ and $\vec{R}_2$, so this rule doesn't apply in this case.

In combination, this means that the DMI vector $\vec{D}_{1,2}$ must lie within the plane formed by the Fe layer and must be perpendicular to $(\vec{R}_1 - \vec{R}_2)$. Only its sign and length are not determined by the Moriya rules.

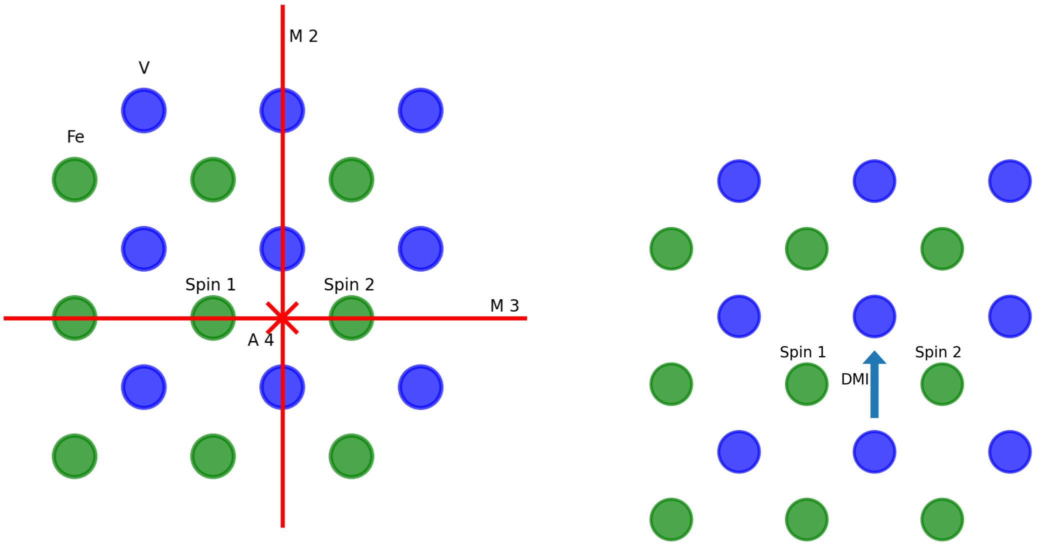

Figure 2.16: Left: Projections of the mirror planes M_2, M_3, along with the projection of the 2-fold rotation axis $\vec{A}_4$, onto the Fe plane, as used in the applied Moriya rules with respect to the two considered spins at $\vec{R}_1$ and $\vec{R}_2$. Right: The resulting DMI vector as it lies within the Fe plane. Its sign and length are not determined by the Moriya rules.

Due to the fact that the DMI vector $\vec{D}_{1,2}$ lies within the plane of the Fe layer and is perpendicular to $(\vec{R}_1 - \vec{R}_2)$, combined with the rotational C_{4v} symmetry of the system, only Néel skyrmions, and not Bloch skyrmions, are stabilized by the DMI in this system [138]. This can be understood when we look at the energy difference due to the DMI, described by $H_{\text{DMI}} = -\sum_{ij} \vec{D}_{ij}(\vec{n}_i \times \vec{n}_j)$. The energy is minimized when the cross product $(\vec{n}_i \times \vec{n}_j)$ aligns with the direction of the DMI vector. When we look at the spin at the center of a supposed skyrmion, which is perpendicular to the Fe layer, a neighboring spin will then be tilted directly within plane M_3, either towards or away from the spin at the center, as it is the case of a Néel skyrmion (see figure 2.12). On the other hand, a $\vec{D}$ parallel to $(\vec{R}_1 - \vec{R}_2)$ would lead to a tilt of spin 2 within plane M_2, leading to the formation of a Bloch skyrmion.

Chapter 3

Tunneling non-collinear magnetoresistance

In order to test the effect of skyrmions on transport, we will take a look at three different systems composed of established materials. But first, I outline the key components and conditions of the calculations. Here, MgO is used as the tunnel barrier for several reasons. Electronic transport through MgO tunnel barriers is well understood on the theoretical level and has been investigated experimentally in many works [22, 96, 97, 139, 140, 141, 142] . Also, the interface between iron and MgO locally provides large electric fields [143], leading to significant spin-orbit coupling (SOC). This interfacial SOC is essential for the DMI interaction, and thus necessary for the stabilization of skyrmions. As computational method, the full-relativistic KKR [144] is used to incorporate SOC and other relativistic effects. Only in a few calculations, where explicitly stated, the scalar relativistic KKR method is used, which excludes SOC but still includes relativistic mass enhancement and the Darwin term. For the leads, we use copper and vanadium, which can be reasonably treated in the KKR method with an angular momentum cut-off of $l_{\text{max}} = 2$. All other applied numerical parameters are explained in appendix A. For the exchange-correlation potential, we use a LSDA potential [54]. The unit cell of the ferromagnetic system is shown in figure 3.1, with the positions provided by M. Czerner [145]. The most important aspect of the unit cell is the structure of the interface, particularly the fact that the Fe atoms in the first layer adjacent to the MgO are directly sitting next to the oxygen atoms [139, 146, 147], as displayed in figure 3.2.

In this work, the iron layer is only one atom thick and hosts the skyrmion. Apart from the iron monolayer, all other atoms in the system are either paramagnetic or diamagnetic.

For the self-consistent calculation of the system in equilibrium, the system is described using a long supercell. In the transport calculations, the leads are semi-infinite and are treated using the decimation technique. This approach means that, in the self-consistent calculation, the long supercell is treated as if the two end regions are in direct contact with each other, which differs from the actual system where the leads are semi-infinite. To avoid introducing artifacts from this artificial contact, I extract the potentials from the atoms located in the central region of the two lead material blocks, which are far away from the ends. These potentials, which accurately represent the bulk properties of the leads, are then used as the effective potential for the semi-infinite leads in the transport calculation using the decimation technique.

In this part of my work, only three systems are treated: V/Fe/MgO/Cu, Cu/Fe/MgO/V, and Cu/Fe/MgO/Cu. These systems are sufficient to demonstrate the potentially large tunnel non-collinear magnetoresistance (TNCMR) effect in MgO barriers and to explain the underlying mechanism. Throughout this thesis, the optimistic definition of TNCMR is used, which is given by

$$\mathrm{TNCMR}\ /\ \% = \frac{T_{\mathrm{NC}} - T_{\mathrm{FM}}}{\min(T_{\mathrm{NC}}, T_{\mathrm{FM}})} \cdot 100\% \tag{3.1}$$

where T_{FM} is the transmission through the ferromagnetic cell, and T_{NC} is the transmission through the non-collinear (in this case, skyrmion) cell.

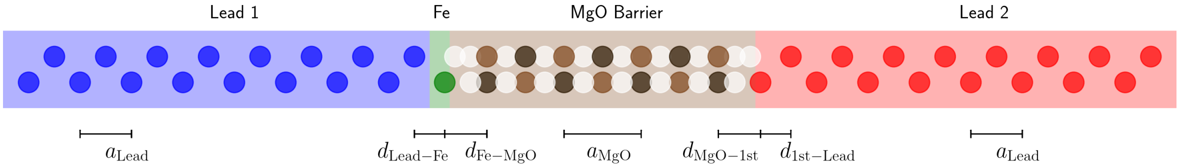

Figure 3.1: In-plane unit cell of the ferromagnetic system with non-magnetized leads. The MgO barrier consists of only 7 monolayers. In the discussion, electrons are interpreted as coming from the left, passing first through the iron layer and then through the MgO barrier into the right lead. In the calculations, empty-spheres are placed in the MgO structure, which are represented by white circles. The lengths and distances are listed in table 3.1.

a_{Lead}	$= 5.4159551\ a_{\mathrm{B}}$	≈ 0.287 nm
$d_{\mathrm{Lead\text{-}Fe}}$	$= 0.59\ a_{\mathrm{Lead}}$	≈ 0.169 nm
$d_{\mathrm{Fe\text{-}MgO}}$	$= 0.82\ a_{\mathrm{Lead}}$	≈ 0.235 nm
a_{MgO}	$= 1.5\ a_{\mathrm{Lead}}$	≈ 0.430 nm
$d_{\mathrm{MgO\text{-}1st}}$	$= d_{\mathrm{Fe\text{-}MgO}}$	≈ 0.235 nm
$d_{\mathrm{1st\text{-}Lead}}$	$= d_{\mathrm{Lead\text{-}Fe}}$	≈ 0.169 nm

Table 3.1: The distances and lattice constants used in the model system. The abbreviation $1st$ refers to the first layer of the lead material.

While iron is the only material in the structure which is magnetized in its bulk form, it also induces significant magnetization in the neighboring layers, as shown in figure 3.3. Especially, the atoms in the interface vanadium layer have approximately one quarter of

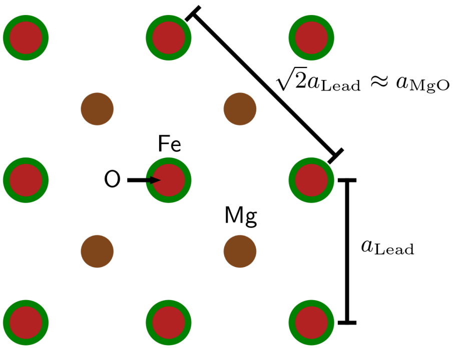

Figure 3.2: In-plane view of the interface structure, showing the iron (green) and first MgO layer (Mg in brown, O in red). The oxygen atoms in the first MgO layer are positioned directly above the iron atoms.

the magnetic moment of the iron layer, but with opposite sign due to the antiferromagnetic coupling between the two layers [148].

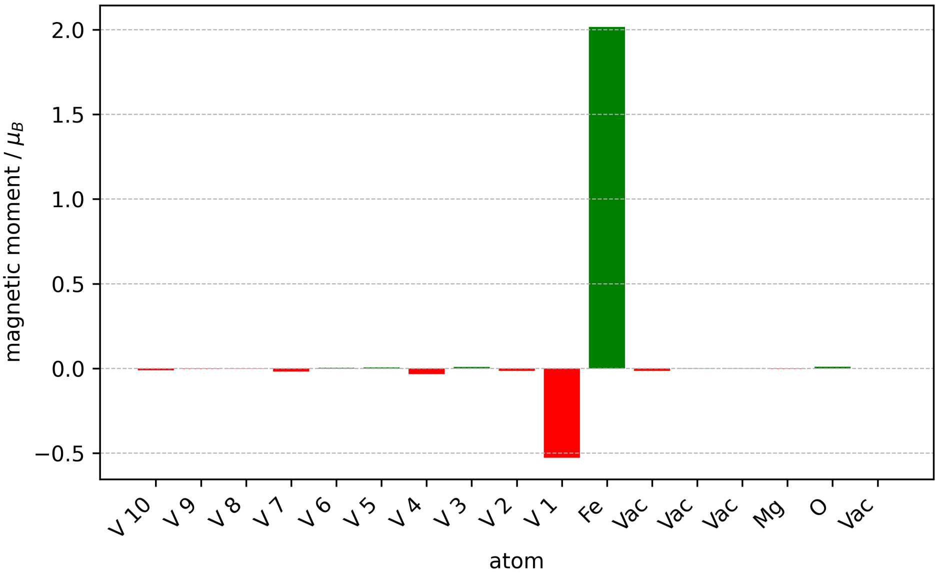

Figure 3.3: Magnetic moments of the atoms in the layer structure. While the first vanadium layer is significantly magnetized, the magnetization rapidly decreases into the vanadium bulk on one side and into the magnesium oxide on the other.

As skyrmion structure, I used two slightly different magnetic structures. The first structure was obtained from an atomistic spin dynamics simulation, which included only the Heisenberg exchange interaction, Dzyaloshinskii–Moriya Interaction (DMI), and an external magnetic field. The parameters were then arbitrarily tuned with the single goal of producing a very small skyrmion that reasonably fits into a 5x5 cell. This structure was used in the earlier calculations with the intention to use a skyrmion structure which reflects the actual underlying magnetic interactions. The second structure was obtained by assuming perfect radial symmetry of the skyrmion, which fully determines the angles Φ

of the magnetic moments. The angle $\Theta(r)$ is described using the analytical formula from [149], which actually describes domain wall profiles but also gives a rough approximation for skyrmions:

$$\theta(\rho, w) = 2 \arcsin\left(\tanh \frac{-\rho}{w/2}\right) + \pi \tag{3.2}$$

This analytically described skyrmion was used in the later calculations because it is a more flexible description. It allows a clean scaling of the skyrmion size and can also be used for other structures, such as antiferromagnetic skyrmions. I fitted the formula to the simulated skyrmion, resulting in a parameter of $w \approx 1.665$ in units of the lattice constant. The skyrmions produced by both methods are very similar and difficult to distinguish in their graphical representations in figure 3.4. The differences between the two skyrmions in their influence on the calculated transport effect are negligible and are discussed in appendix B. Additionally, in appendix B, I explain why the self-consistent potential was calculated only for the ferromagnetic cell without including the skyrmion, and how the transmission is affected when the magnetic moments in all layers, not just the iron layer, are tilted according to the skyrmion shape.

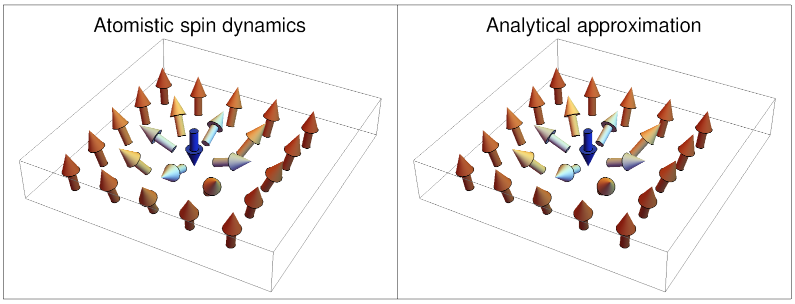

Figure 3.4: The two different yet very similar model skyrmions used for calculations in this section. Adapted from [O1]. Copyright (2019) by the American Physical Society.

Actual skyrmions in similar structures have also been observed experimentally. However, these studies involved heavier metals directly below the ferromagnetic layer, and they all observed much larger skyrmions than those used in this work. For example, Chen et al. [150] reported sub-100 nm magnetic skyrmions even at room temperature in Ir/-CoFeB/MgO structures, but they consider the large DMI to be mainly caused by the heavy metal to CoFeB interface. Denker et al. [115] reported 85 nm skyrmions in Ta/-CoFeB/MgO trilayers, which only exist in the material for a very specific range of CoFeB thickness, $t_{\mathrm{CoFeB}} = 1.20$ nm to 1.44 nm . This is due to the transition from perpendicular magnetic anisotropy (PMA) to in-plane magnetic anisotropy (IMA) around $t_{\mathrm{CoFeB}} = 1.384$ nm, where the effective magnetic anisotropy vanishes. Experimentalists typically use a mixture of iron, cobalt, and boron, hence CoFeB [151, 152], because it leads to a more pristine barrier structure. Usually, the boron is absorbed by the mostly used underlying tantalum [153] during the annealing step, but the magnetic layer still remains a mixture of Fe and Co. In contrast, I consider a pure Fe monolayer in most calculations in this work. To better understand how this mixture might affect the overall TNCMR, I explore this difference in subsection 3.5, where I consider the effect of chemical impurities due to mixing of Co and Fe.

3.1 Energy dependent transmission

Technically, for electronic transport, only the transmission at the Fermi energy is relevant. However, it is still helpful to have information about the transmission over a broader energy range. When a bias voltage is applied, the transmission within the corresponding energy window contributes to the overall transport. Additionally, the position of the Fermi energy itself can also be shifted by some extent, a process known as Fermi level engineering. The transmission and the resulting TNCMR effect, calculated using the NEGF method within KKR for the three systems, are shown in figure 3.5.

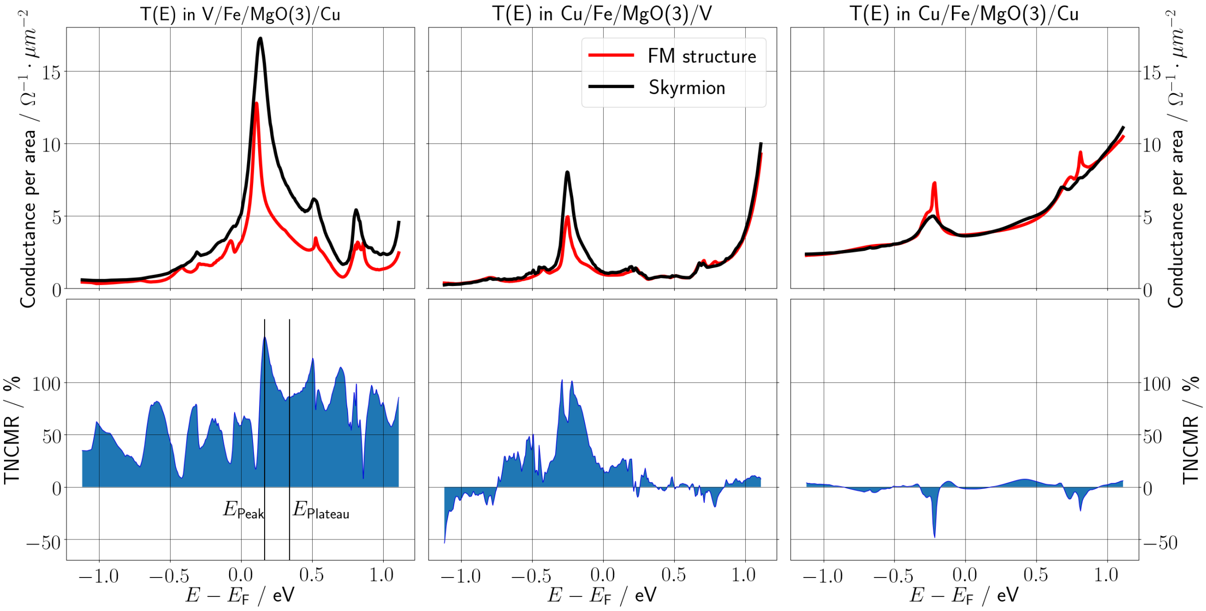

Figure 3.5: The top row displays the energy dependent transmission curves for all three systems: the ferromagnetic case (red) and the case with a skyrmion present in the iron layer (black). The resulting TNCMR effect is given by the difference of both values, divided by the smaller one. The vertical lines indicate the sample energies selected for the later analysis of the effect's dependence on skyrmion size. The figure is taken from [O1]. Copyright (2019) by the American Physical Society.

We immediately see that the TNCMR is very different for each material stack. While it is quite small in case of Cu/Fe/MgO/Cu, it is very large in case of V/Fe/MgO/Cu. We want to follow this trail in the following sections to gain a better understanding of the large effect calculated for the V/Fe/MgO/Cu structure.

3.2 Dependence on barrier thickness

To better understand the role of the MgO barrier, I calculated the energy dependent transmission for all five barrier thicknesses, ranging from 3 to 7 MgO monolayers, through the V/Fe/MgO/Cu structure. The results for the ferromagnetic and skyrmion cells are presented in figure 3.6. At first glance, we see that all curves have a very similar shape for all barrier widths, but the size of the transmission decreases by about one order of magnitude with each additional MgO monolayer. However, this is not true for the peaks of the transmission in the ferromagnetic cells, where the maximum peak height decreases much more slowly than the rest of the transmission curve as the barrier width is increasing. Another interesting observation can be made regarding the large transmission peak at about 0.13 eV above E_F. It turns out that the peak shifts to lower energies for odd numbers of MgO monolayers and towards higher energies for even numbers. This oscillation in peak position converges with increasing barrier width. The lower transmission peak does not exhibit this even-odd variation. The presence of a skyrmion affects the transmission similarly across all barrier thicknesses, which can be summarized by two main observations. First, the peaks of the transmission are smoothed down by the skyrmion, which can be attributed to the disturbance of quantum well states (QWS), which will be explained in more detail in section 3.6. Second, the skyrmion leads to a large increase in transmission over a wide energy range. This increase grows with increasing barrier thickness, which is explained in section 3.3 based on $k_{\parallel}$-scattering and the symmetry filtering effect in MgO.

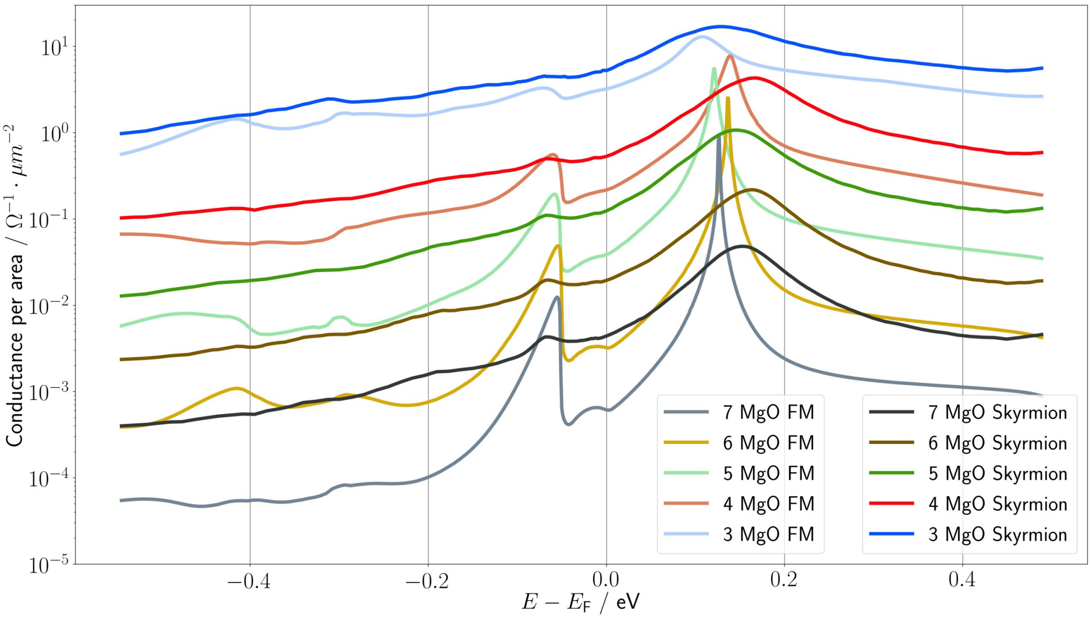

Figure 3.6: The energy dependent transmission curves for different MgO barrier thicknesses. The color represents the barrier thickness. For each thickness, the transmission through the ferromagnetic (FM) cell is plotted in a pale color, while the transmission through the skyrmion cell is plotted in the corresponding stronger color.

The resulting optimistic TNCMR effect is displayed in figure 3.7. In case of the 3-monolayer MgO barrier, the increase of the transmission fully compensates for the smearing of the sharp peaks. For thicker barriers the smearing of the peaks dominates, leading to an overall negative TNCMR effect at the peak energies. At the Fermi energy and most other energies within the considered range, the TNCMR effect is positive and increases with a greater barrier thickness.

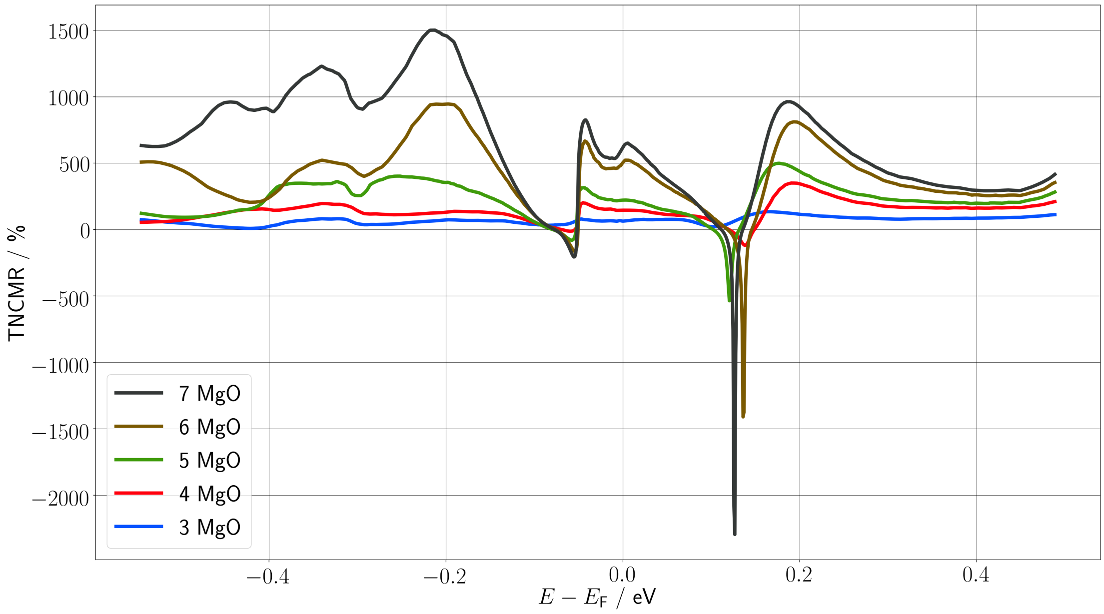

Figure 3.7: The energy dependent TNCMR effect for different MgO barrier thicknesses is shown. The color indicates the barrier thickness. In general, the TNCMR effect increases with barrier width and is positive for most energies. Only in two small energy ranges, corresponding to peaks of the transmission curve, does the TNCMR effect show negative spikes.

3.3 Scattering enhanced transmission mechanism

In order to gain deeper insight into the underlying mechanism, it is helpful to examine a $k_\parallel$ resolved map of the transmission. Since the skyrmion breaks the in-plane translational invariance, the transmission can no longer be plotted in the large Brillouin zone of the unit cell. But since the leads remain bulk like, the total transmission can be decomposed into a specular ($k_\parallel$-conserving) and a diffusive ($k_\parallel$-scattering) contribution. The decomposition formalism itself is explained in detail in section 2.4. The diffusive contribution $T(k_\parallel, k'_\parallel)$ can be projected onto the two leads separately:

$$
\begin{aligned}
T_{\text{diff,in}}(k_{\|}) &= \sum_{k'_{\|} \neq k_{\|}} T(k_{\|}, k'_{\|}) \\
T_{\text{diff,out}}(k_{\|}) &= \sum_{k'_{\|} \neq k_{\|}} T(k'_{\|}, k_{\|})
\end{aligned}
$$

A diffusive contribution can only arise when in-plane translational invariance is broken. To gain deeper insight into the underlying physics, we compare the transmittance maps of V/Fe/MgO(3)/Cu and Cu/Fe/MgO(3)/V at the Fermi energy. The diffusive contribution projected onto both leads, the specular contribution, and the transmittance map for the ferromagnetic case are plotted in figure 3.8. As we see in figure 3.5, a skyrmion increases the transmission at E_F in case of V/Fe/MgO(3)/Cu by about 60%. In Cu/Fe/MgO(3)/V, transmission is increased only slightly. The details behind this difference are clarified in the following explanation, based on the results in figure 3.8, with the mechanism driving this behavior sketched in figure 3.9. When looking at the transmittance maps in figure 3.8, we see that the total transmission in case of V/Fe/MgO(3)/Cu is dominated by a large diffusive contribution. This diffusive contribution arises from electrons entering the system in areas (k_sc) away from the Γ-point in vanadium, scattering in the skyrmion layer, and then leaving the system at and near the Γ-point in copper. The transmittance map in the ferromagnetic case shows that the transmission at the Γ-point vanishes. This means that vanadium does not provide any states at the Γ-point, which would be suitable for crossing the MgO barrier without scattering. The presence of the skyrmion, however, breaks translational invariance, allowing electrons from vanadium to scatter to the Γ-point, become Δ_1 like, and cross the MgO barrier with a much higher transmission probability than without a skyrmion. This underlying mechanism may therefore be referred to as the scattering-enhanced transmission mechanism. We can thus say that the entire system acts as a spin valve, which can be opened with a skyrmion as a movable switch. This mechanism also explains why the skyrmion does not enhance transmission in Cu/Fe/MgO(3)/V as effectively as in V/Fe/MgO(3)/Cu. In case of Cu/Fe/MgO(3)/V, the electrons can still not tunnel very well from the vanadium through the barrier, since the skyrmion, which would allow transmission-enhancing scattering, is located at the other side of the barrier.

The responsible material properties can already be seen from the Bloch spectral density of the bulk systems. Being at the Γ-point is not a sufficient criterion for Δ_1 states. The states also need to have $m = 0$. This can be seen in Bloch density of states of vanadium bulk, plotted in figure 3.10, where we see that only the $m = \pm 2$ components of vanadium are not vanishing at the Γ-point. As explained in [154], in a material with C_{4v} symmetry, electronic states at the Γ-point with $l = 2$ and $m = \pm 2$ can either have Δ_2 or Δ'_2

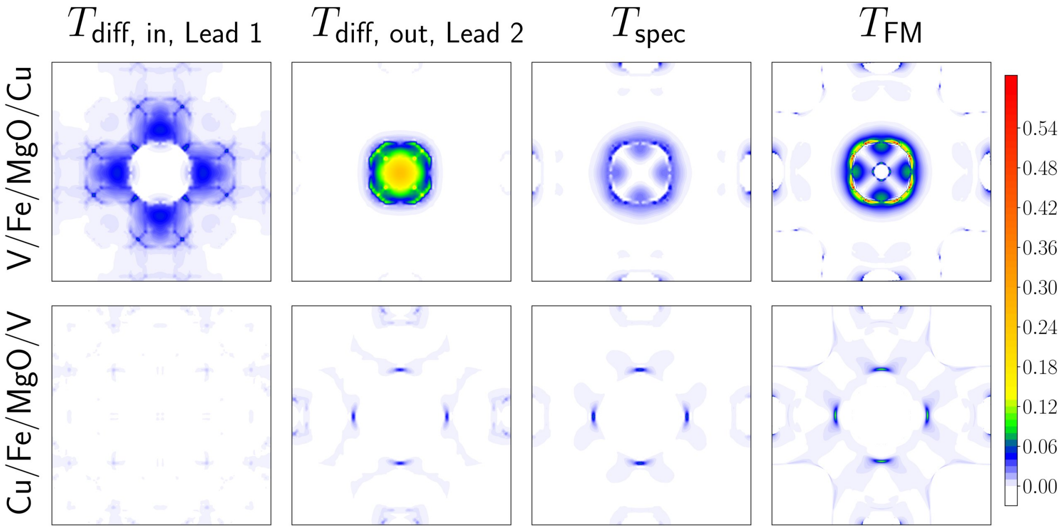

Figure 3.8: The rows show the $k_{\|}$-resolved transmission at the Fermi energy for the two systems, obtained when using V and Cu as leads in Lead 1/Fe/MgO(3)/Lead 2 . The first three columns show the diffusive contribution of the in- and out-scattering electrons, and the specular contribution of the transmission in the presence of a skyrmion. The right column shows the transmission (T_{FM}) in the ferromagnetic case. The color scale, in arbitrary units, is used in all following k-resolved Bloch density of states and transmission plots. We see a large diffusive contribution in the case of V/Fe/MgO(3)/Cu, including electrons far from the Γ-point in vanadium, being scattered to the Γ-point in copper. The applied colormap with arbitrary units is used in all subsequent density plots. Adapted from [O1]. Copyright (2019) by the American Physical Society.

symmetry, both of which lead to a very low tunneling probability through MgO. Hence, the states in vanadium at the Γ-point are not Δ_1-like and cannot tunnel well through the MgO barrier. This can further be verified by a band structure calculation resolved by the irreducible representations (IRR). The IRR resolved band structures for vanadium, copper, and iron are displayed in figure 3.11. It turns out that vanadium at the Fermi level indeed only provides Δ_2-states at the Γ-point. This is in perfect agreement with the results in references [155] and [140].

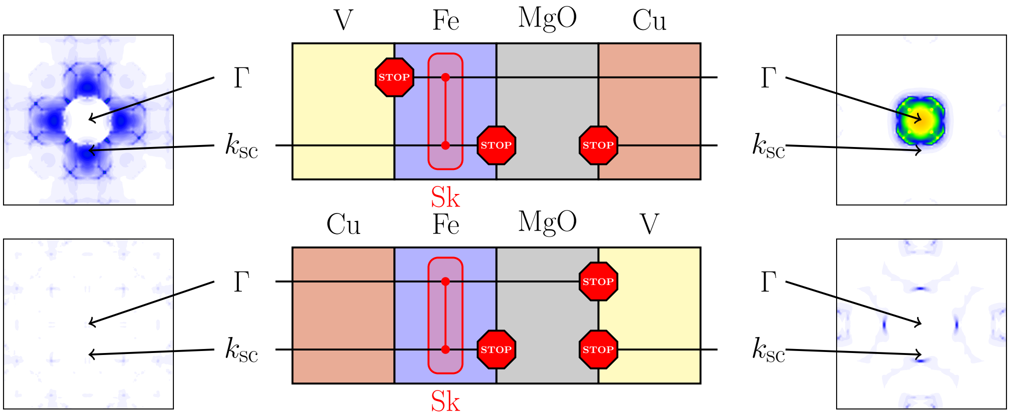

Figure 3.9: At the Fermi energy electrons from vanadium can not tunnel well through the MgO barrier. The skyrmion layer (Sk) enables $k_{\|}$-scattering, which allows electrons from vanadium in V/Fe/MgO(3)/Fe to become Δ_1-like and tunnel through the MgO with a high probability. On the other hand, in case of Cu/Fe/MgO(3)/V the skyrmion does only enable scattering on the copper side, where Δ_1-like electrons are already present in the ferromagnetic case. The figure is taken from [O1]. Copyright (2019) by the American Physical Society.

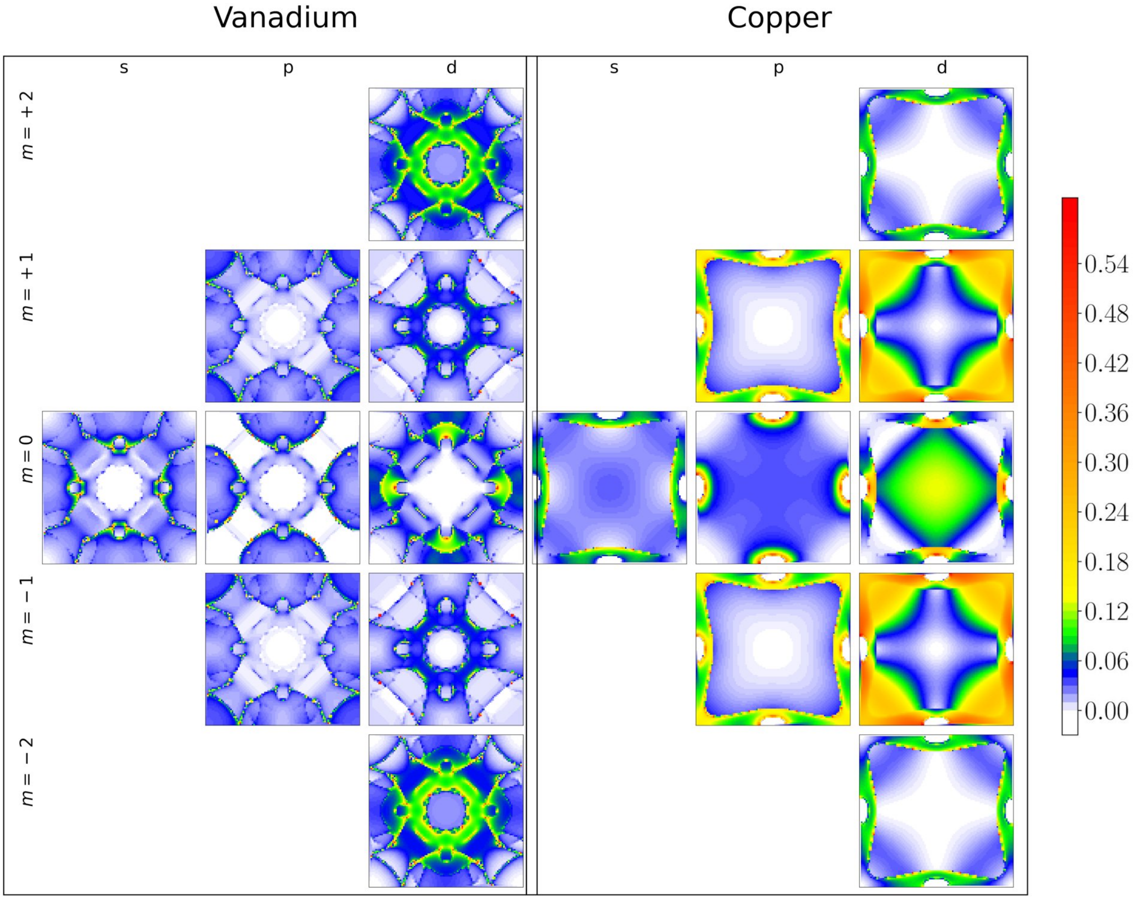

Figure 3.10: The Bloch spectral density of bulk vanadium and copper at the Fermi energy of the composed V/Fe/MgO/Cu system. The potentials are identical to the lead potentials of the V/Fe/MgO/Cu cell. Vanadium provides states at the Γ-point, but they are not Δ_1-like, since they are of $m = \pm 2$ character. Copper, on the other hand, provides electrons at the Γ-point with $m = 0$, which are therefore Δ_1-states.

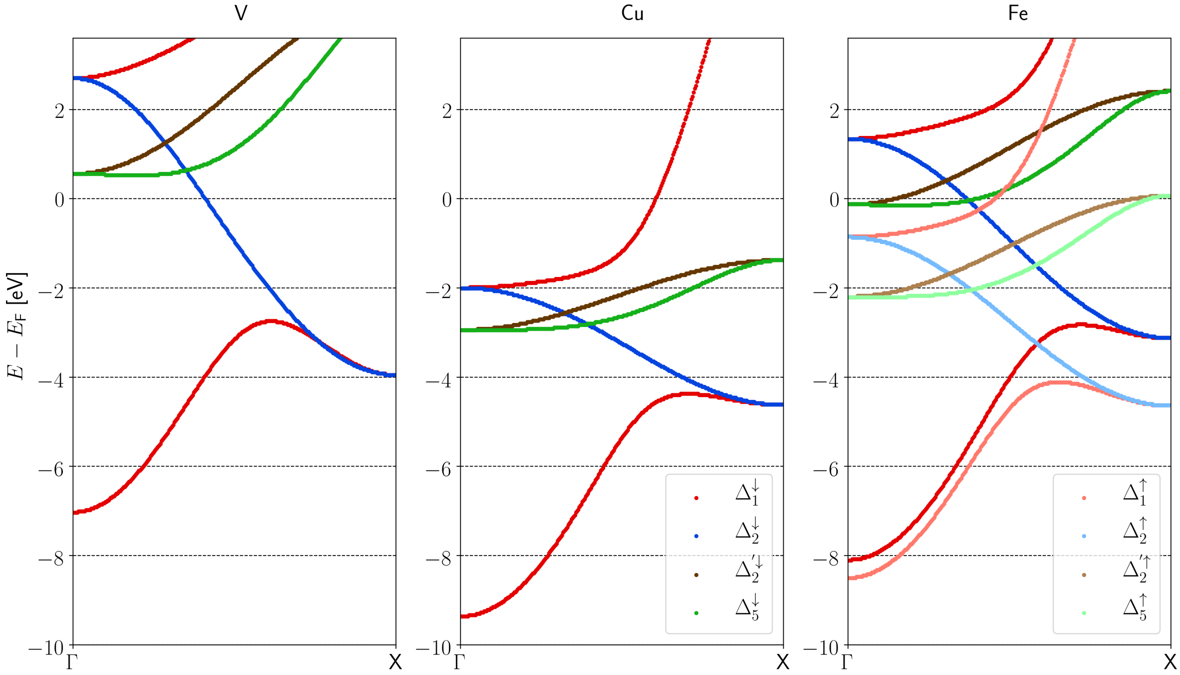

Figure 3.11: Band structures of copper, vanadium, and iron. The different IRRs are indicated by the color. At the Fermi level, along the plotted path, vanadium only provides poorly transmitting Δ_2-states, copper only provides well-transmitting Δ_1-states, and iron provides well transmitting Δ_1-states only in the majority (here up ↑) spin channel.

3.4 Dependence on the skyrmion size

Since the effect is caused by local changes of the magnetization direction, a smaller change of the direction from atom to atom can be expected to lead to a smaller effect. In order to understand how the effect scales with the size of the skyrmions, I calculated the effect for 4 different skyrmion sizes (see figure 3.12) at three different energies in the V/Fe/MgO(3)/Cu system. Larger skyrmions are very challenging because the size of the matrix in the computer's memory increases with N^4, where N is the width of the supercell. To achieve a clean scaling of the skyrmion to different sizes, perfect cylindrical symmetry is assumed, and the radial dependence of θ is described by the approximate equation 3.2 given by Romming et al. [156]. Continuing from [156], the skyrmion diameter is defined by the circle where $m_z = 0$. This formula can not precisely represent the shape of the 5x5 skyrmion obtained from atomistic spin-dynamics simulations, but it provides a reasonable fit. The sample energies are denoted alongside the energy dependent transmission curves in figure 3.5. The resulting effect sizes, with increasing skyrmion size, are displayed in figure 3.13. As expected, the effect shrinks with increased skyrmion size. This suggests that for realistic skyrmions, which are typically much larger, a smaller effect than for the 5x5 skyrmion should be expected.

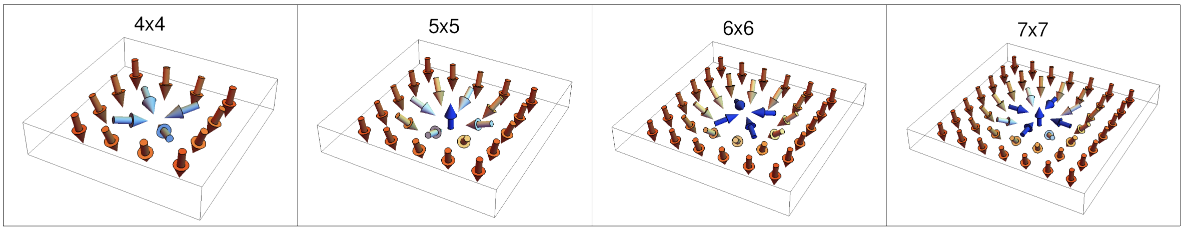

Figure 3.12: The four skyrmions which were used for the analysis of the size dependence of the effect. Due to the very small size of the model skyrmions, the structure around the center varies significantly between even and odd sizes.

3.5 Influence of defects

The previous explanation of the underlying mechanism relies on scattering due to the skyrmion in the iron layer, along with a blocking of transport between vanadium and MgO in the ferromagnetic case. This suggests that other types of defects, like chemical disorder or phonons, could potentially undermine the TNCMR effect by increasing the conductance through the ferromagnetic sample. A first hint that the crucial blocking of transport between vanadium and the MgO is experimentally obtainable is provided by Martínez et al. [155]. They state that, while the measured conductance through their Fe/MgO/V sample does not completely vanish, it is about 100 times smaller than through samples of Fe/MgO(2nm)/CoFe and Fe/MgO(2nm)/Au of comparable geometry and quality. So we

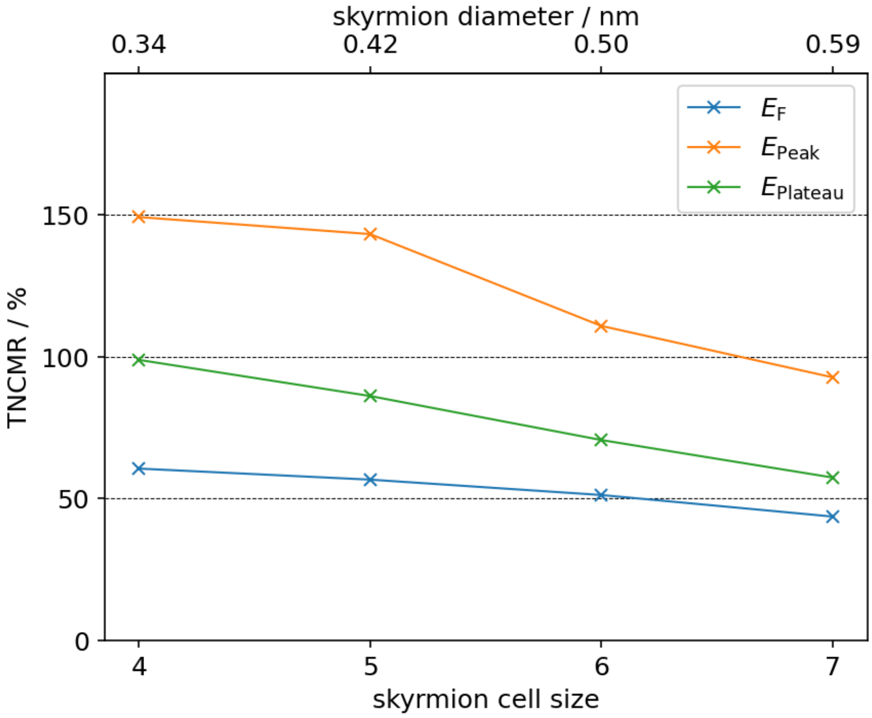

Figure 3.13: The size of the TNCMR effect in V/Fe/MgO(3)/Cu at E_F and two other selected energies, as denoted in figure 3.5, for different skyrmion sizes. The resulting effect continuously decreases with increasing skyrmion size. This is expected, since the relative change of the magnetization direction from one atom to its neighbor, which is the main driver of the TNCMR effect, becomes smaller as the skyrmion size is increasing.

know that it is possible to create actual samples that demonstrate a blocking of transport between vanadium and MgO, despite their unavoidable interface roughness and other defects. Now I take a different approach by evaluating this from a theoretical perspective. To assess how disturbances might weaken the blocking of states from vanadium through the barrier, and thereby weaken the overall effect, I use transport calculations based on the coherent potential approximation (CPA) [86] and vertex correction to simulate the influence of chemical disorder on the conductance through the V/Fe/MgO/Cu system. I also use the rather newly [91] implemented method for electron-phonon induced resistivity within the NEGF formalism.

The results in figures 3.14 and 3.15 indicate that scattering due to chemical impurities can indeed lead to an increase of transmission through the ferromagnetic V/Fe/MgO/Cu cell, which may diminish the experimentally observable TNCMR effect. The simulated phonon interaction did not lead to an increase in the transmission.

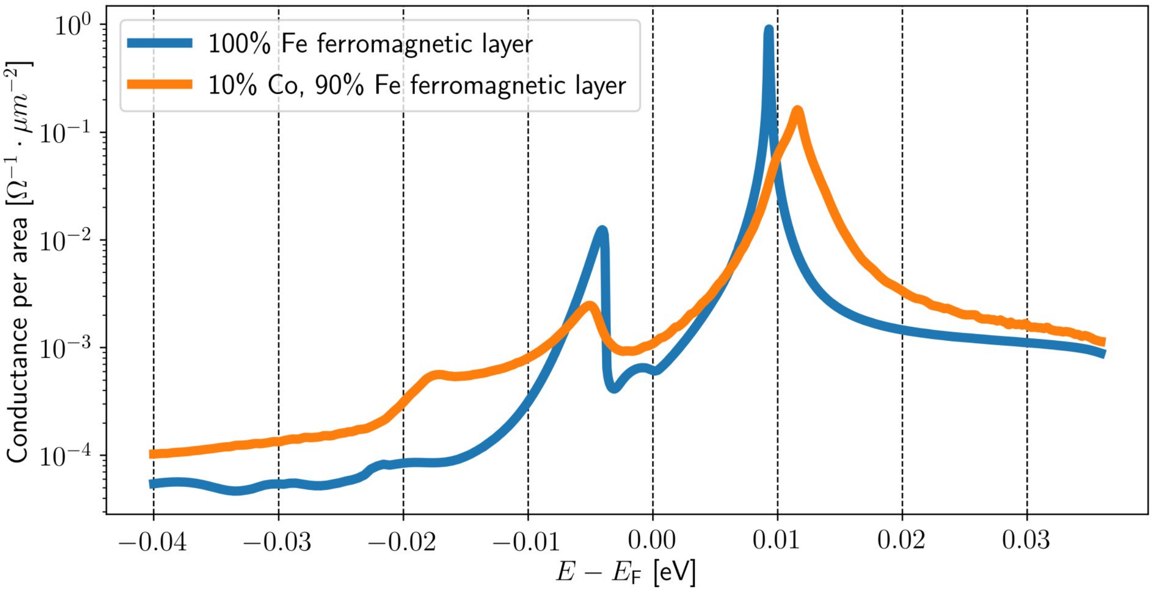

Figure 3.14: The energy dependent conductance through the ferromagnetic V/Fe/MgO(7)/Cu cell with a pure Fe layer and a mixed Co/Fe layer, simulated using the CPA method in comparison. Similar to the increase in transmission due to scattering on a skyrmion, the disturbance caused by a mixed Co/Fe layer leads to an increase in transmission. However, the increase in transmission is smaller and has a different energy dependency compared to the increase caused by the 5x5 skyrmion shown in figure 3.6.

3.6 Quantum well states

The previously explained scattering-enhanced transmission mechanism is based on bulk states and explains the overall increase of conductance through the barrier. However, it can not explain the sharp conductance peaks in the ferromagnetic cell and why they are broadened and reduced in the presence of the skyrmion. This is because it does not consider the influence of the interface structure and possible quantum well states (QWS) in the thin iron layer. The conductance peaks can either be caused by interface resonance states (IRS) [96, 157] or by possible quantum well states (QWS), which are known to be important for this system [140, 158]. An IRS is a two-dimensional state localized at an interface and it can couple to a band of the lead. QWS are not located directly at the interface between two materials but exist within the thin layer itself. Both types of states can lead to a large increase in conductance around a specific energy in a small region of reciprocal space. To understand whether and how the conductance peaks plotted in figure 3.6 originate from IRS or QWS, I take a look at several different properties of these peaks.

First, I take a look at the dependence of these states on the thickness d of the iron monolayer without recalculating the potentials. IRS only exist at the interface between two materials, which means that their energy levels are not very sensitive to the thicknesses of these material layers. The energies of QWS, on the other hand, are in theory proportional

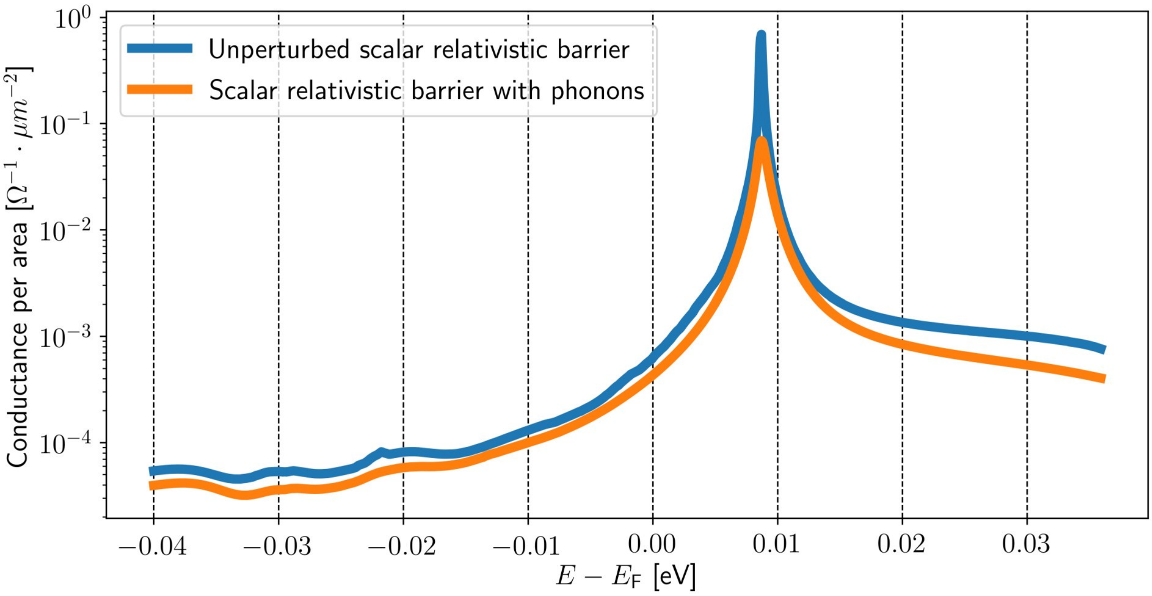

Figure 3.15: The scalar-relativistic, energy dependent conductance through the ferromagnetic V/Fe/MgO(7)/Cu cell with an undisturbed pure Fe layer and a Fe layer disturbed by phonons, shown for comparison. Phonon scattering, as described by [91], does not lead to an increase in transmission.

to $\propto 1/d^2$, which means that for very small changes in d, we would expect to see a nearly linear shift in the energy of the conductance peaks. In figure 3.16, we see the results of calculations for three steps of a linear change in the iron layer thickness d. As expected for QWS, the energetic positions of both conductance peaks shift almost linearly.

The other property that allows to distinguish between a QWS and a IRS is the transmission and their density in reciprocal space. IRS can be very complex and often provide sharp peaks [96] in reciprocal space. Perfect QWS are much simpler and have a parabolic energy dependency on $k_{||}^2$, with $\vec{k}_{||}$ being a wave vector parallel to the plane defined by the iron layer. And at a fixed energy, the $\vec{k}_{||}$ dependent transmission is expected to form a circle with a very thin border.

In figure 3.17, the $\vec{k}_{||}$ dependent transmission at both peaks is displayed. The energetically lower peak QWS 1, at about 0.06 eV below $\mathrm{E_F}$, indeed forms a circle with a very thin border in reciprocal state, as expected for a QWS. The other peak, at about 0.13 eV above $\mathrm{E_F}$, is not really circular, but a perfect circle cannot be expected since the potential in the well is neither even nor isotropic.

Another approach for distinguishing between IRS and QWS could be to analyze their spatial dependence orthogonally to the plane defined by the well. The KKR method allows us to see the density resolved by atom layers in reciprocal space, which is called the bloch spectral function (BSF) of each atomic layer, which is displayed in figures 3.18 and 3.19 for both states. However, since the well is only one atomic monolayer thick, we cannot determine if the states decay from the interface into the well, as expected for an

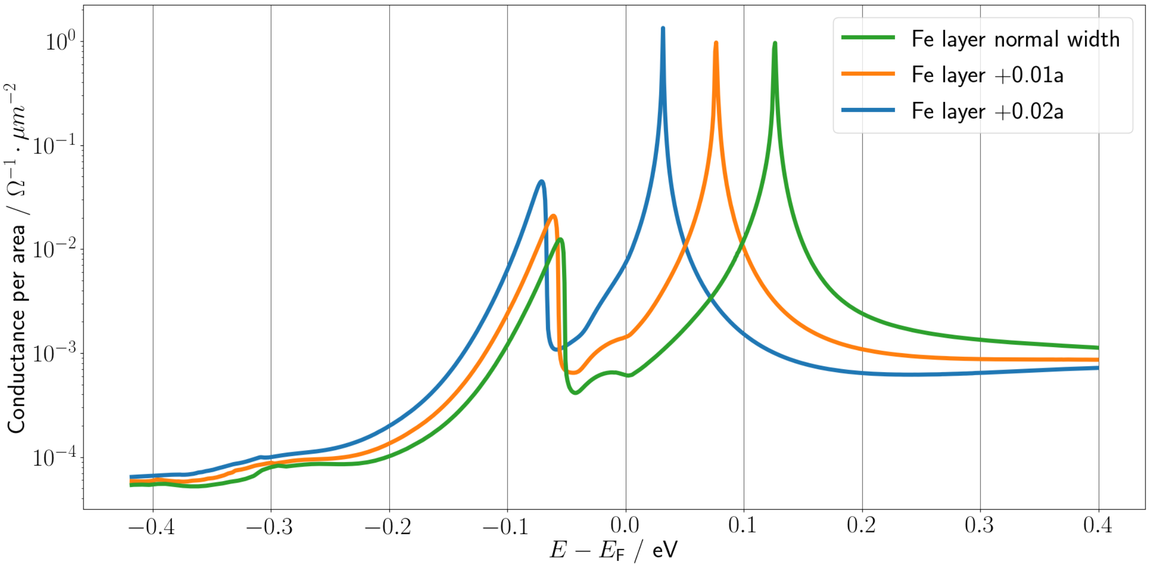

Figure 3.16: The energy dependent conductance through V/Fe/MgO(7)/Cu is shown for three different widths of the Fe layer. In the normal relaxed geometry (green), which was used in all other calculations, the distance between the last V layer and the first MgO layer is 1.0895a, with a being the lattice constant of Fe. The gap containing the Fe layer is widened by +0.01a steps to 1.0995a (orange) and 1.1095a (blue). For all calculations, the same self-consistent potentials of the individual atoms in the relaxed structure are used. The almost linear shift of the conductance peaks with varying layer width suggests that these are caused by quantum well states.

IRS, or if they have a nearly constant density throughout the entire well width. But we can confirm that both states are indeed located in the iron layer and observe how they leak into the MgO barrier and V lead.

While a high density of states is generally good for large transmission (within the Julliere model explained in 2.5), large transmission also requires matching states in the other lead and good transmission of the states through the barrier. To understand how much both QWS actually have a parabolic structure and how much the density of states can be converted into transmission, I display both the energy dependent BSF, also called BSFE, alongside the $\vec{k}_{\|}$ resolved energy dependent transmission and the total energy dependent transmission in a single image 3.20. At first glance, we see that both conductance peaks correspond to van-Hove singularities of the QWS states. The energetically higher QWS 2 shows a significant deviation from the parabolic shape, but except for a small region around the Γ-point, all states contribute to the transmission.

When looking at the l- and m-resolved BSF at the energy of QWS 2, around 0.13 eV above $\mathrm{E_F}$ in the Fe layer, as displayed in figure 3.21, we can verify how well this observation matches the known symmetry filtering mechanism of MgO. We see that QWS 2 is dominated by the spin up-channel (majority) by $m = 0$ states for $l = 1, 2, 3$ around the Γ-point, which are thus actually Δ_1-like states, as required for efficient tunneling through

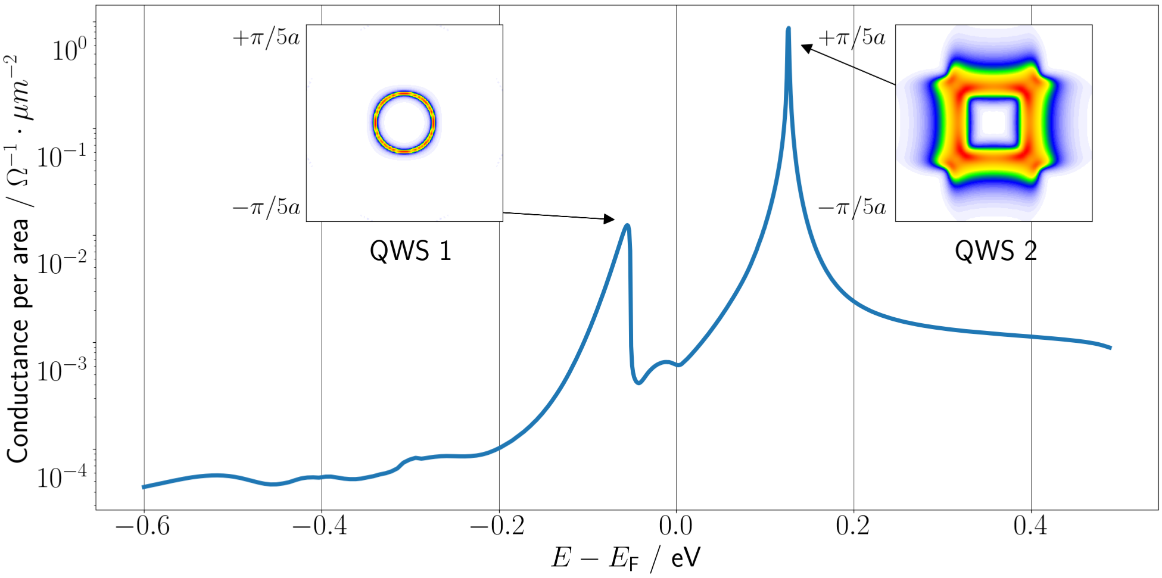

Figure 3.17: The energy dependent conductance through V/Fe/MgO(7)/Cu. The insets show the k-resolved transmission at the two peaks. They correspond to the quantum well states (QWS 1 and QWS 2) discussed in this chapter.

MgO. However, the states in the very small spot around the Γ-point still do not contribute to the transport, because the QWS cannot couple to any suitable states in vanadium at the Γ-point.

The energetically lower QWS 1, around 0.06 eV below E_F, exhibits a much more interesting behaviour. In the BSFE, we see that it consists of two bands dominated by the down-spin channel (minority), with the lower band being a relativistic split-off band, which also has a small up-spin portion. Comparing the BSFE to the transmission, we see that the split-off band almost exclusively contributes to the transmission of QWS 1, while the other band has a vanishingly small contribution to the transmission. The role of the relativistic split-off band becomes even more evident when we do the calculations without including spin

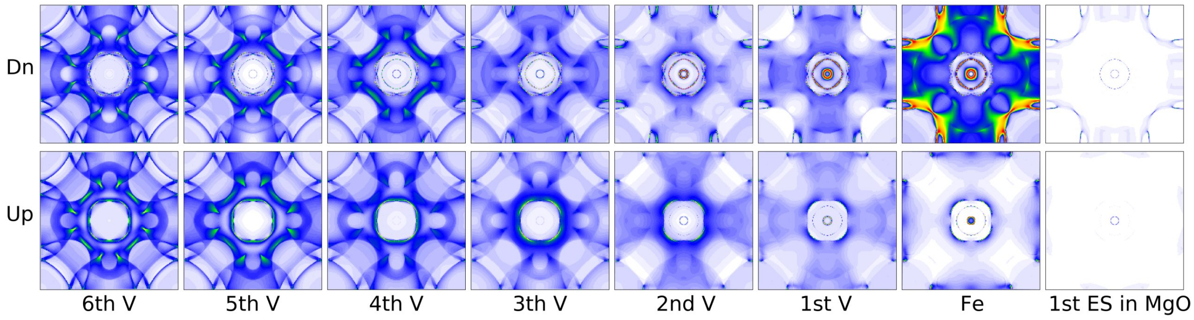

Figure 3.18: The atomically resolved BSF of QWS 1 at about 0.06 eV below E_F. The vanadium layers are numbered, followed by the iron layer, and then only the first adjacent empty sphere of the MgO barrier is included. We see that QWS 1 is located in the iron layer, is dominant in the down (minority) spin channel, and quickly decays into the bulk vanadium and MgO barrier.

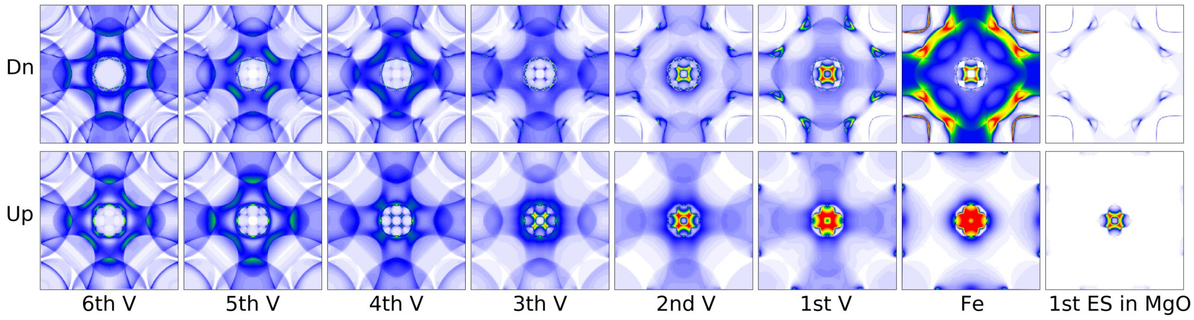

Figure 3.19: The atomically resolved BSF of QWS 2 at approximately 0.13 eV above E_F. It is dominant in the up (majority) spin channel and remains visible in the neighboring vanadium layers, though it decays slowly as it extends further into the lead material.

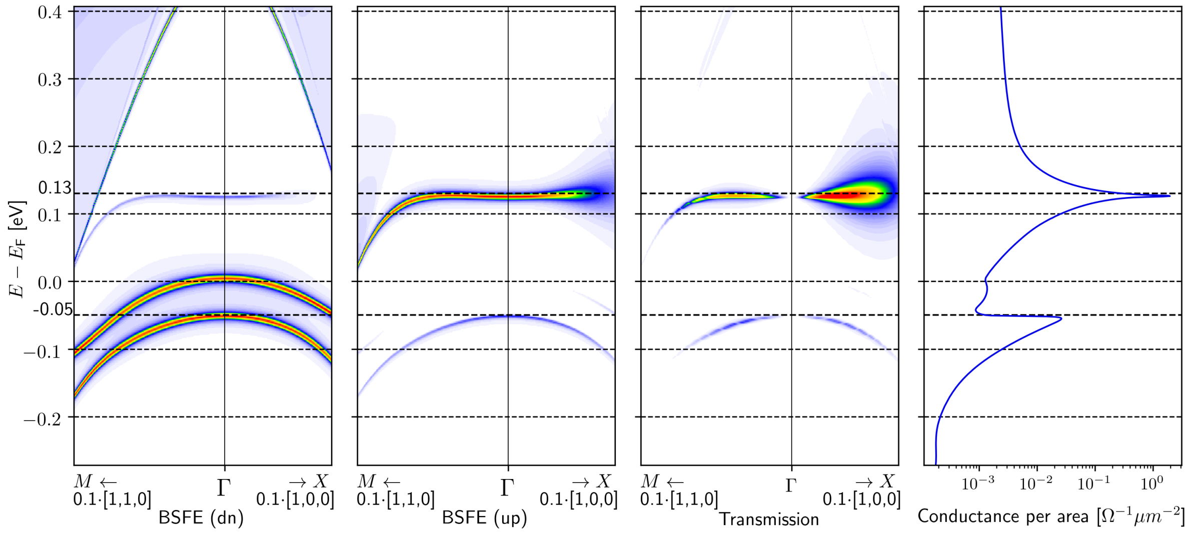

Figure 3.20: Comparison of the energy dependent conductance, the k resolved transmission, and the energy resolved BSF. As expected, the conductance peaks correspond to the van-Hove singularities of the QWS bands. Interestingly, the energetically lower QWS 1, around 0.06 eV below E_F, has a split-off band that almost exclusively contributes to the transmission of QWS 1.

orbit coupling (SOC). The way this is done is explained in reference [144]. The results of that are displayed in figure 3.22. Now we see that, without SOC, the two bands of the lower QWS 1, around 0.06 eV below E_F, merge into one degenerate band and no longer provide a transmission peak.

This becomes more clear when we take a look at the l- and m-resolved BSF of that state without SOC, shown in figure 3.23. Here, we see that the energetically lower non-relativistic QWS 1 is dominated by $l = 2$, $m = \pm 1$ components, making it Δ_5-like and thus not well-suited for tunneling through the MgO barrier. But when SOC is taken into account, as we see in figure 3.24, the structure in the $l = 2$, $m = \pm 1$ components near the Γ-point splits into two separate rings. Additionally, a small ring appears in the up spin channel at $l = 2$, $m = 0$ making it Δ_1-like, which allows efficient tunneling, leading to the

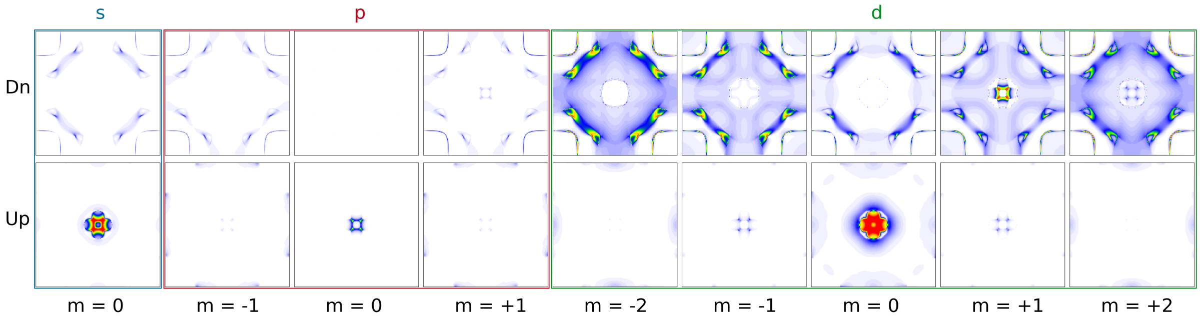

Figure 3.21: The l- and m-resolved BSF in the iron layer of QWS 2, around 0.13 eV above E_F. QWS 2 is dominated by the $m = 0$ components of the up-spin (majority) channel, so we shall call it Δ_1-like.

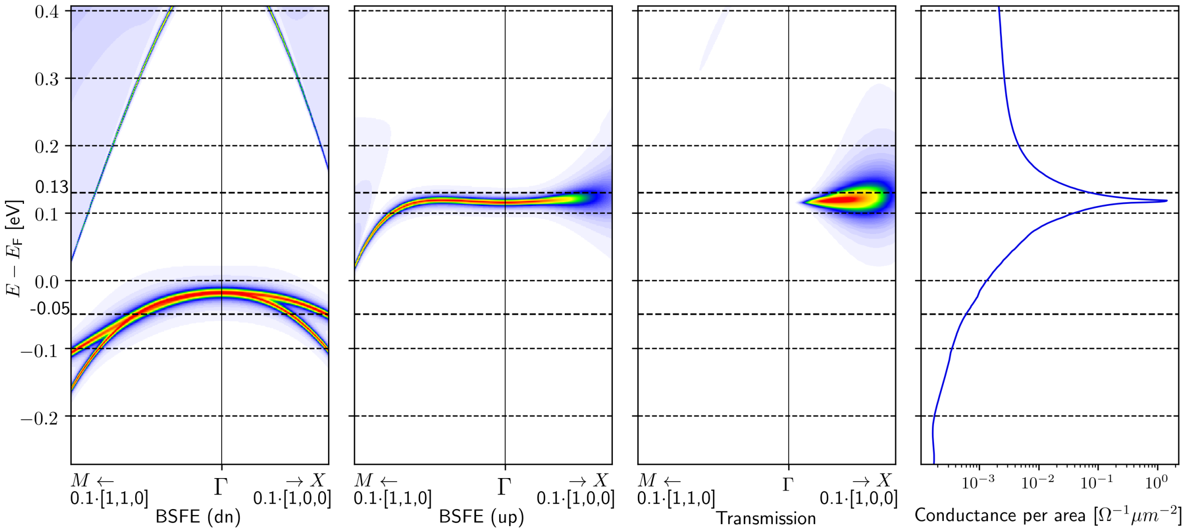

Figure 3.22: Comparison of the energy dependent conductance with the energy resolved BSF without SOC. The lower QWS 1, around 0.06 eV below E_F, is degenerate and does not lead to any transmission peak.

corresponding transmission peak. This result is quite remarkable because is shows that a density peak of a van-Hove singularity can contribute almost zero transmission, but can then lead to a huge transmission peak when the relatively weak SOC effect is taken into account.

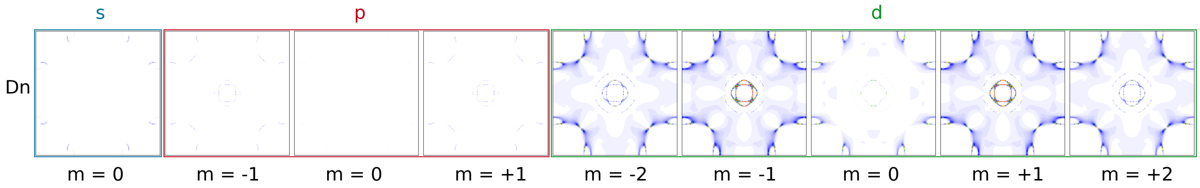

Figure 3.23: The l- and m-resolved scalar-relativistic BSF in the iron layer of the down-spin contribution of QWS 1, 0.06 eV below $\mathrm{E_F}$. Without SOC, the $l = 2$, $m = \pm 1$ components are identical. The up (majority) contribution is vanishingly small.

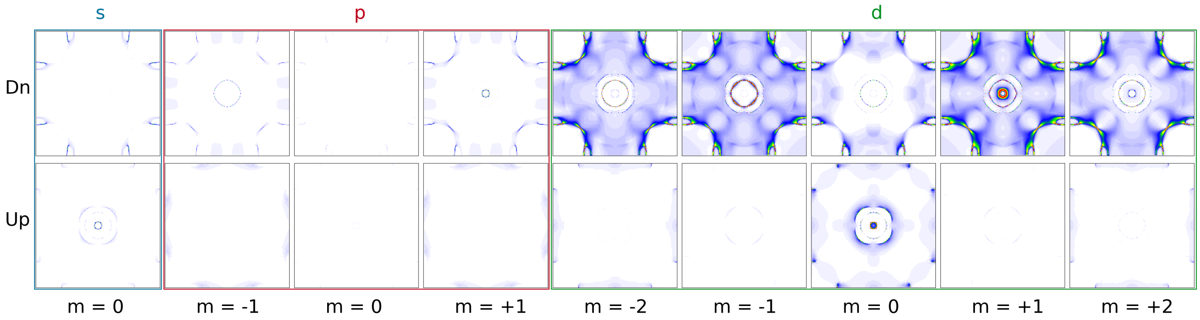

Figure 3.24: The l- and m-resolved BSF in the iron layer of QWS 1, 0.06 eV below $\mathrm{E_F}$. QWS 1 is dominated by the $l = 2$, $m = \pm 1$ components of the down-spin (minority) channel, making it Δ_5-like. The different behaviour of $m = +1$ and $m = -1$ is solely due to SOC. The smaller $l = 2$, $m = 0$ component in the up-spin (majority) channel contains a small Δ_1-like ring. Only the small ring of the $l = 2$, $m = +1$ and $m = 0$ parts around the Γ-point is responsible for the increased transmission.

3.6.1 Relativistic transmission peak

The origin of the small QWS 1 Δ_1-like ring, which is crucial for the transmission peak, can be explained by applying SOC with perturbation theory to the non-relativistic wave function. The angular momentum resolved BSF of the contributing states in figure 3.23 provides the right ansatz for the non-relativistic wave function:

$$|\Psi\rangle \propto |\Psi_1\rangle + |\Psi_2\rangle$$

$$|\Psi_1\rangle = |l = 2, m_s = -\frac{1}{2}, m = +1\rangle$$

$$|\Psi_2\rangle = |l = 2, m_s = -\frac{1}{2}, m = -1\rangle$$

Now we treat the influence of the spin-orbit coupling Hamiltonian $\hat{H}_{\mathrm{SO}}$ in first order perturbation theory. Using

$$\hat{H}_{\mathrm{SO}} = \hat{L} \cdot \hat{S} = \hat{L}_z \hat{S}_z + \frac{1}{2}(\hat{L}_+ \hat{S}_- + \hat{L}_- \hat{S}_+)$$

we see that $|\Psi_1\rangle$ and $|\Psi_2\rangle$ diagonalize $\hat{H}_{\mathrm{SO}}$ and thus provide a good basis set to treat the problem:

$$\begin{pmatrix} \langle\Psi_1|\hat{H}_{\mathrm{SO}}|\Psi_1\rangle & \langle\Psi_1|\hat{H}_{\mathrm{SO}}|\Psi_2\rangle \\ \langle\Psi_2|\hat{H}_{\mathrm{SO}}|\Psi_1\rangle & \langle\Psi_2|\hat{H}_{\mathrm{SO}}|\Psi_2\rangle \end{pmatrix} = \frac{\hbar^2}{2}\begin{pmatrix} -1 & 0 \\ 0 & 1 \end{pmatrix}$$

Spin-orbit coupling lifts the degeneracy of the two states:

$$E^{(1)}_{1/2} = \pm\frac{\hbar^2}{2}$$

In the next step, we derive the change of the wave function in first order perturbation theory to understand the magnificent change in the transmission. When working with a basis $|n\rangle$, the perturbation of first order on $|\Psi_{1/2}\rangle$ is given by

$$|\Psi^{(1)}_{1/2}\rangle = \sum_{|n^{(0)}\rangle\neq|\Psi_{1/2}\rangle} |n^{(0)}\rangle \frac{\langle n^{(0)}|\hat{H}_{\mathrm{SO}}|\Psi_{1/2}\rangle}{E^{(0)}_{1/2} - E^{(0)}_n}.$$

When we use angular momentum eigenstates as basis $|n\rangle$, we can exploit the orthogonality relations and find that most matrix elements $\langle n^{(0)}|\hat{H}_{\mathrm{SO}}|\Psi_{1/2}\rangle$ vanish. The only remaining matrix element for each wave function represents its respective first order change:

$$|\Psi^{(1)}_1\rangle \propto |l = 2, m_s = +\frac{1}{2}, m = 0\rangle \tag{3.3}$$

$$|\Psi^{(1)}_2\rangle \propto |l = 2, m_s = +\frac{1}{2}, m = -2\rangle \tag{3.4}$$

This means that $|\Psi^{(1)}_1\rangle$ is Δ_1-like! While we do not know much else about the exact wavefunctions and eigenenergies, this result is sufficient to understand the conductance increase due to SOC. As explained in chapter 2.5, the transmission probability at the Γ-point through the MgO barrier highly depends on the symmetry character of the wave function and is strongly enhanced in case of Δ_1-symmetry, i.e. $m = 0$. This means that a small perturbation from SOC can be responsible for a large increase of the tunneling probability. A similar behaviour was described in [159], where a small Δ_1-contribution due to SOC was predicted to have a significant influence on the overall TMR in an IrMn/FeCo/MgO/FeCo/IrMn structure.

3.6.2 Influence of spin-orbit coupling

After describing the nature of the QWS in the ferromagnetic system, I will continue to investigate how they can be affected by a skyrmion and therefore contribute to the overall

TNCMR effect.

From the non-relativistic point of view, the absolute direction of the magnetization direction is unrelated to the crystal orientation in real space. Within the Dirac equation, however, this is not the case. The leading term, which connects the orbital angular momentum $\vec{L}$ and the spin $\vec{S}$ of an electron, is then called spin-orbit coupling (SOC). It is responsible for effects linking real space and the absolute magnetization direction, like tunneling anisotropy resistance (TAMR) and magnetic anisotropy. From the previous analysis, we know that the transmission from the energetically lower QWS 1 is highly dependent on the influence of SOC on the state. This implies that a rotation of the magnetization direction of the iron layer, which is directly connected to the QWS via SOC, can have very significant effect on the transmission, which is the TAMR effect.

TAMR is typically measured in systems where a tunnel barrier is sandwiched between a ferromagnetic and a non-magnetized layer, as in the V/Fe/MgO/Cu structure used in this work. Even though there are no heavy elements involved in this system, the interface between Fe and MgO provides significantly large SOC [142, 160, 161, 143]. Since the magnetization direction changes locally within a skyrmion, part of the total change in conductance due to the skyrmion can be attributed to TAMR. But a clear decomposition is a not a trivial task, however, it is important to understand how much the overall effect is driven by TAMR.

As a first step in analyzing the role of SOC in this system, I determined the out-of-plane TAMR by calculating the energy dependent transmission through the V/Fe/MgO(7)/Cu structure when the magnetization of the iron layer is lying in-plane, and compared it to the same structure with out-of-plane magnetization. The results, which are displayed in figure 3.25, show a significant shift in the conductance peak of the energetically lower QWS 1. This shift directly corresponds to a substantial TAMR effect, which is plotted in figure 3.26. The previous explanation of the scattering mechanism behind the calculated TNCMR effect in section 3.3 does not involve SOC, and only the conductance at the energetically lower QWS 1 appears to be strongly dependent on SOC. This suggests that the total TNCMR effect should not change much when SOC is scaled to zero [144]. To disentangle the different effects, I calculated the TNCMR effect in the V/Fe/MgO/Cu structure without SOC, thereby removing the TAMR contribution, and compared it to the originally calculated TNCMR with SOC. Both energy dependent TNCMR effects are plotted in figure 3.27.

The difference between these two TNCMR values is referred to as ΔTNCMR. The ΔTNCMR and the pure out-of-plane TAMR are plotted in figure 3.28. We can see that ΔTNCMR and pure TAMR are close to zero for most energies. However, for some energies, TNCMR changes drastically when SOC is scaled down, particularly at energies where TAMR is large as well and exactly where the energetically lower QWS 1 is located.

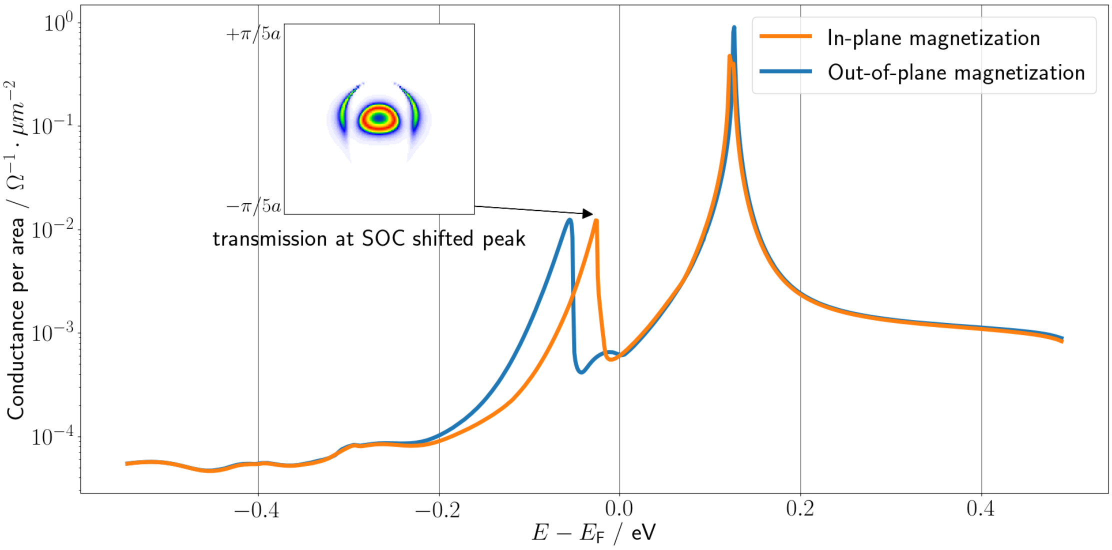

Figure 3.25: Energy dependent conductance through V/Fe/MgO(7)/Cu with in-plane magnetization, compared to the previously plotted conductance with out-of-plane magnetization. The inset shows the k resolved transmission at the SOC induced peak, which is shifted by the tilt of the magnetization.

Despite this, ΔTNCMR and TAMR are not directly correlated, and ΔTNCMR is much smaller than the total TNCMR effect for most energies.

In summary, while SOC does influence the overall effect through TAMR and also slightly beyond TAMR, it is only of minor importance for the TNCMR effect. The key role of SOC in the Dzyaloshinskii–Moriya interaction (DMI), and consequently in the formation of skyrmions, which is essential for the actual occurrence of the TNCMR effect from skyrmions in a real system, remains, of course, unaffected by this result.

3.6.3 Smearing of peaks by QWS disturbance

While TAMR can partially explain the TNCMR due to the energetically lower QWS 1 around 0.06 eV below E_F, it does not explain the sharp negative peak in TNCMR caused by the energetically higher QWS 2, which is clearly visible in figure 3.7. In figure 3.6, we see that the skyrmion not only increases the conductance over a wide energy range, but also broadens the peaks. This smearing of conductance peaks is also visible in the CPA chemical disorder calculation for the system in figure 3.14. As explained in [162], perturbation from phonons and defects decreases the quasiparticle lifetime of QWS in quantum wells, leading to an energetic broadening of the corresponding peaks. From this point of view, the skyrmion is a defect as well, which broadens the peaks. This smearing mechanism explains the small negative TNCMR peak in the Cu/Fe/MgO/Cu system in figure 3.5, and partially the two negative TNCMR peaks (fig. 3.7) in the V/Fe/MgO/Cu system, which are related to the two QWS discussed in this chapter.

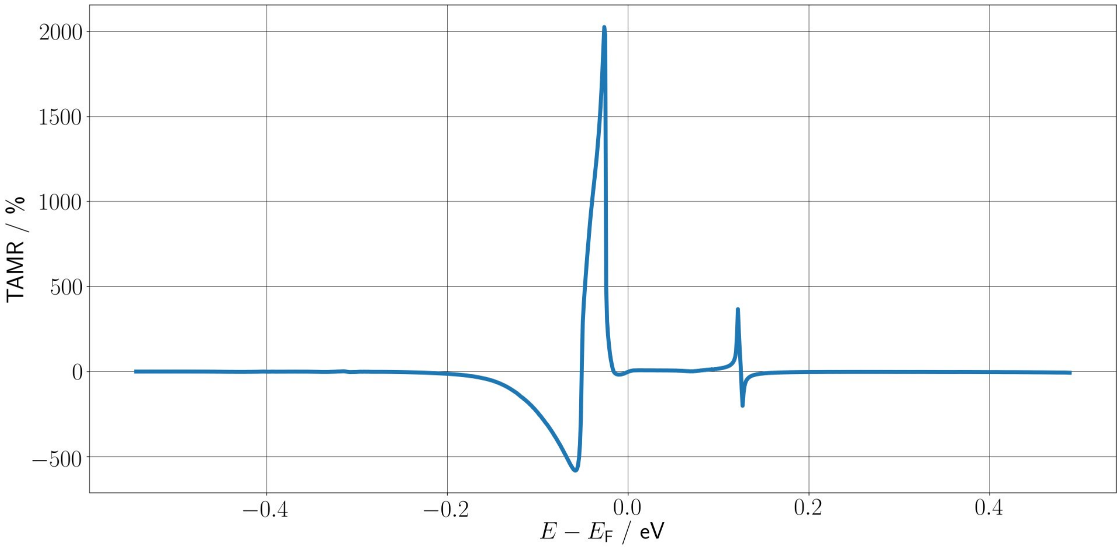

Figure 3.26: The resulting energy dependent TAMR between in-plane and out-of-plane magnetization for V/Fe/MgO(7)/Cu. The effect is dominated by the SOC sensitive QWS 1, around 0.06 eV below E_F.

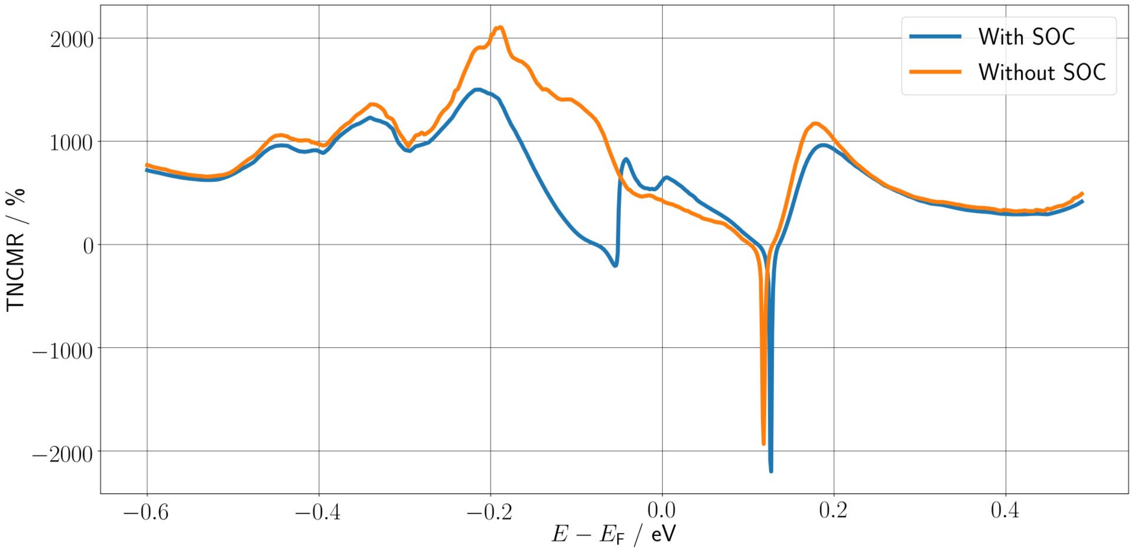

Figure 3.27: The TNCMR effect due to a skyrmion with SOC and a calculation of the TNCMR without SOC in the V/Fe/MgO(7)/Cu cell.

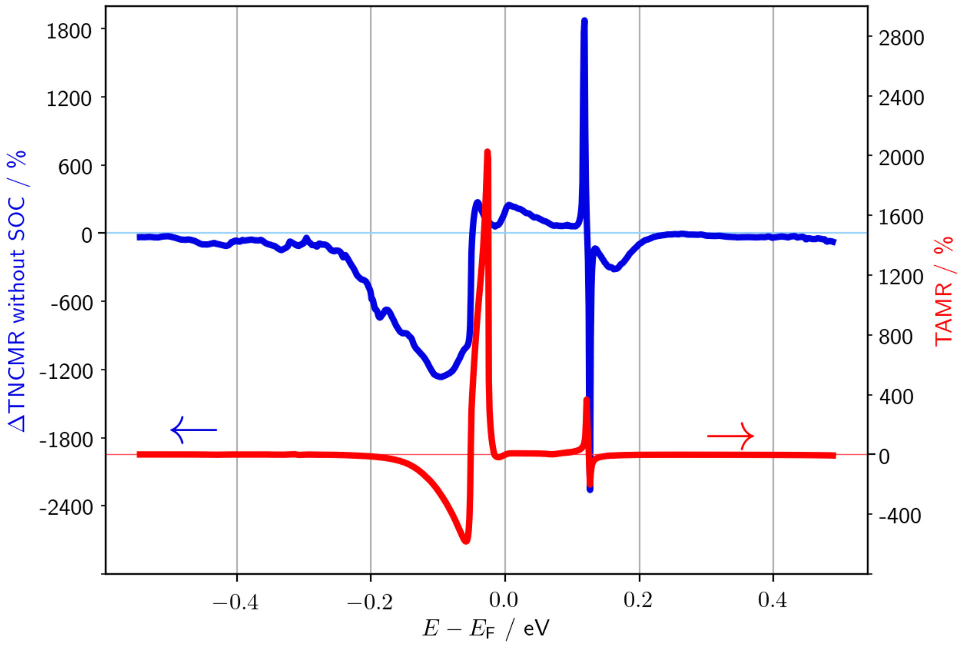

Figure 3.28: The difference between a calculation of TNCMR with SOC and a calculation without SOC (left axis) in the V/Fe/MgO(7)/Fe cell. The ferromagnetic out-of-plane TAMR effect (right axis).

3.6.4 Discussion of increase and decrease of transmission

While an increase in the transmission through the scattering mechanism by 10% in figure 3.5 seems about as valuable as a reduction due to peak smearing by 10%, an increase is actually more desirable in practice. This is because a skyrmion might only influence the conductance in a small area of the total detection area. In such a case, the total conductance through the tunnel barrier is more sensitive to an increase of conductance in a small area than to a decrease of similar size. This can be seen by approximating the detection tunnel barrier as an array of resistors connected in parallel. The TNCMR effect due to a small skyrmion can be seen as a variation of the resistance of only one of the resistors. Let's assume the tunnel junction covers an area N times the size of the skyrmion, and the resistance through the skyrmion's area in the ferromagnetic state is R, with the appearance of the skyrmion changing the local resistance in its area by a factor x. Then, we can calculate total resistance R_{tot} through the tunnel junction with and without skyrmion via

$$\frac{1}{R_{\mathrm{tot}}} = \underbrace{\frac{1}{R} + ... + \frac{1}{R}}_{N-1} + \frac{1}{x \cdot R}. \tag{3.5}$$

Then the change of the total resistance is:

$$\Rightarrow \frac{R_{\text{tot, skyr}}}{R_{\text{tot, fm}}} = \frac{N}{N - 1 + \frac{1}{x}} \tag{3.6}$$

As an example, we now assume 10 resistors in total, and the resistance of one resistor is doubled. In this case, the total resistance increases by about 5%. But if the resistance of that one resistors drops by 50%, the total resistance drops by about 9%. This effect becomes even more evident in the limit. If the skyrmion could completely block any transmission in its vicinity (i.e. $x \to \infty$), we would end up with a total resistance increase of only about 11% for $N = 10$. On the other hand, if the skyrmion would lead to a complete drop of resistance in its vicinity, the total resistance would drop by 100% to complete zero for any N. Thus, we can demonstrate with simple physical arguments that an increase of transmission tends to produce a stronger signal, because of the effective parallel connection of many resistors in a tunnel junction, making an increase in transmission more desirable for actual detection devices.

Chapter 4

Tunneling non-collinear magneto-Seebeck effect

When two stripes of different electric conducting materials are connected at two contacts to form an electric circuit, and both contacts have different temperatures, an electric current begins to flow through the circuit. This generation of voltage due to temperature differences is called the Seebeck effect [163, 164]. This effect can also be observed in magnetic tunnel barriers [37]. When one side of the barrier structure is suddenly heated with a laser, a temperature gradient forms across the barrier structure, and a voltage between between both leads of the junction can be measured.

4.1 Theory

The energy dependent transmission, which is calculated using the NEGF formalism, cannot be directly measured. But some information about the transmission function can still be gained experimentally by measuring the conductance and the Seebeck coefficient [165, 166]. At zero temperature, the conductance is identical to the transmission at the Fermi energy, multiplied by the conductance quantum. And as explained in [167, 37], at finite temperature and vanishing bias voltage, the conductance is given by

$$g = \frac{e^2}{h} \int T(E) \left(-\frac{\partial}{\partial E} f(E, E_\mathrm{F}, T) \right) \mathrm{d}E. \tag{4.1}$$

With the Fermi-Dirac distribution

$$f(E, E_\mathrm{F}, T) = \frac{1}{e^{\frac{E-E_\mathrm{F}}{k_\mathrm{B}T}} + 1}, \tag{4.2}$$

the Seebeck coefficient is calculated by

$$S = -\frac{\int T(E)(E - E_{\mathrm{F}})\left(-\frac{\partial}{\partial E} f(E, E_{\mathrm{F}}, T)\right) \mathrm{d}E}{e \int T(E)\left(-\frac{\partial}{\partial E} f(E, E_{\mathrm{F}}, T)\right) \mathrm{d}E}, \tag{4.3}$$

which is essentially the geometric center of $T(E)\left(-\frac{\partial}{\partial E} f(E, E_{\mathrm{F}}, T)\right)$. Thus, a large conductance of the material is associated with a large transmission function, and a large absolute Seebeck coefficient is related to a steep slope of the transmission function. Since both properties of the transmission function are independent of each other, a change in the magnetic configuration of the system might have a significant effect on one of the properties, while the other property may remain mostly unaffected. For the collinear case, the corresponding Seebeck effect is called tunnel magneto-Seebeck effect (TMS) [165, 37, 168, 169].

4.2 Results

Since the discovery of the tunnel magneto-Seebeck effect (TMS) [37], we know that the magnetic configuration of a tunnel barrier can alter not only the conductance but also the Seebeck coefficient. Further research [166] on the TMS effect in tunnel barriers with Co-Fe alloy leads showed that the Seebeck coefficient can be significantly more sensitive to disorder than the conductance. In this chapter, I verify whether this trend also applies to disorder caused by non-collinear magnetic structures. To understand the general behaviour of the Seebeck coefficient, both the energy dependence and the temperature dependence are investigated. All calculations are carried out in the V/Fe/MgO/Cu system with 3 to 7 monolayers of MgO. Figure 4.1 displays the energy dependent Seebeck coefficient for T=100 K, and T=300 K separately. Please note the different scaling of the Seebeck coefficient axis.

In figure 4.1, it can be seen that the Seebeck coefficients for larger barrier thicknesses have similar energy dependence. Because of that, we will focus on wider MgO barriers of 5 to 7 MgO monolayers in the following figures, as they are more representative, while keeping the plots less complex.

Figure 4.2 displays the Seebeck coefficients at 300 K for both the ferromagnetic and the skyrmion system at once. This allows for a better comparison between the two cases. First, we see that the Seebeck coefficient in the skyrmion cell is usually smaller than in the ferromagnetic cell. While the general energy dependent behaviour is similar, the Seebeck effect is reduced when the skyrmion is present.

The change in the Seebeck coefficient due to changes of magnetic structure is also known

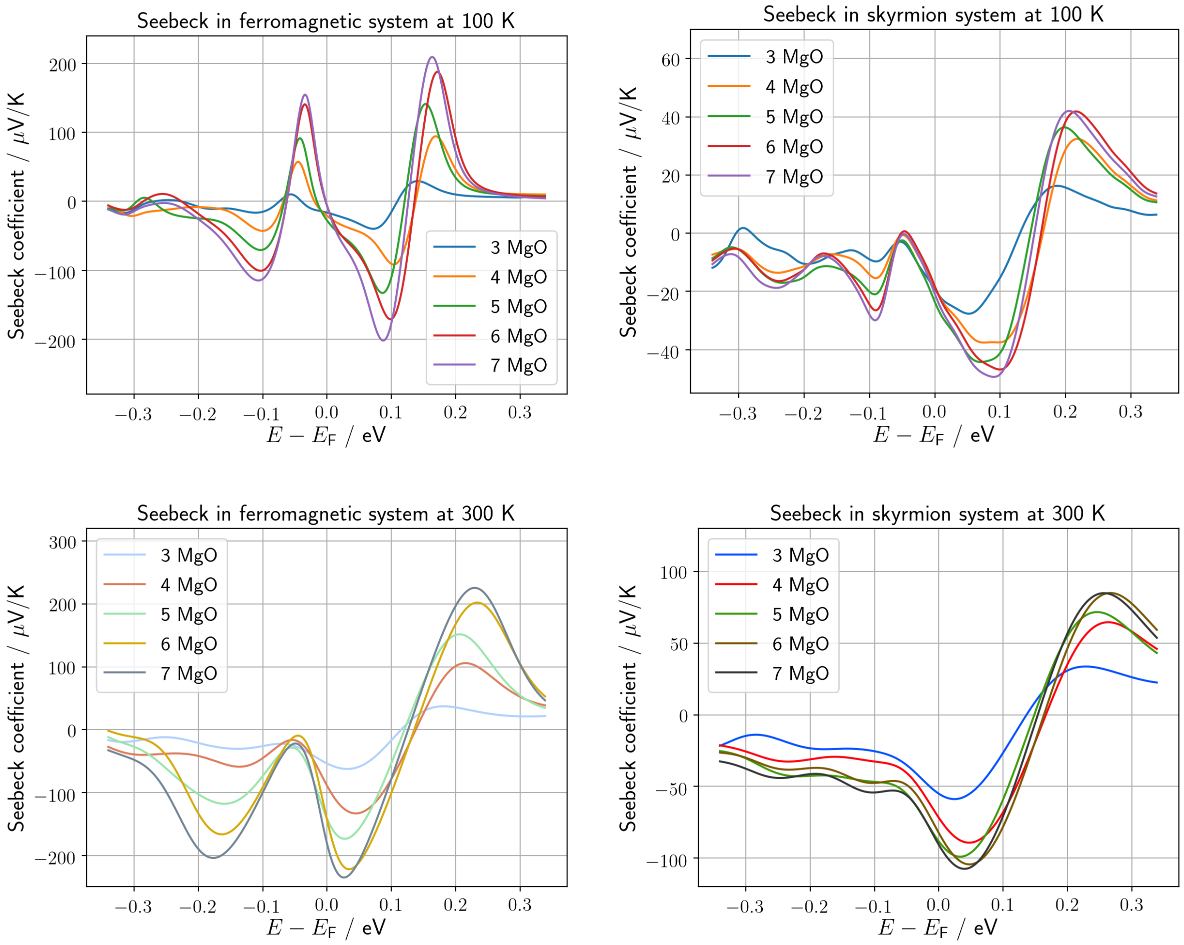

Figure 4.1: Seebeck coefficient for two different temperatures, for both the ferromagnetic and 5×5 skyrmion system. The calculations were carried out for 3 to 7 monolayers of MgO in the V/Fe/MgO/Cu system.

as magneto-thermoelectric power (MTEP) [165, 170], and is defined by

$$\mathrm{MTEP} = \frac{S_\mathrm{skyr} - S_\mathrm{fm}}{\min(|S_\mathrm{skyr}|, |S_\mathrm{fm}|)} \cdot 100\%. \tag{4.4}$$

The change in MTEP with respect to energy at 300 K is displayed in figure 4.3. Since S in the denominator can become zero, the MTEP ratio can theoretically become infinite.

The parallel connection of Seebeck coefficients is more complicated than that of resistors, which is explained in references [171, 172, 173]. However, they also show that if we can neglect in-plane currents, we can calculate the total Seebeck coefficient by

$$S_\mathrm{total} = \frac{(1-x)\sigma_\mathrm{fm} S_\mathrm{fm} + x\sigma_\mathrm{skyr} S_\mathrm{skyr}}{(1-x)\sigma_\mathrm{fm} + x\sigma_\mathrm{skyr}}, \tag{4.5}$$

where x is the fraction of the area, which is covered by the skyrmion, σ_fm is the conductance through the ferromagnetic system, and σ_skyr is the conductance through the skyrmion. If

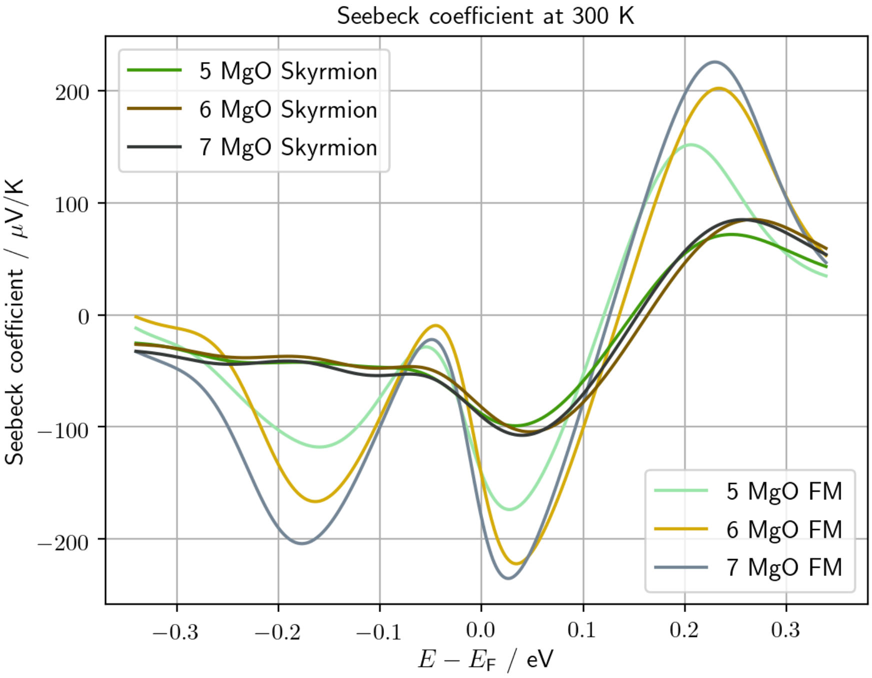

Figure 4.2: The Seebeck coefficient at 300 K for both the ferromagnetic and 5×5 skyrmion system.

we assume for simplicity $\sigma_{\mathrm{fm}} = \sigma_{\mathrm{skyr}}$, then this breaks down to $S_{\mathrm{total}} = (1-x)S_{\mathrm{fm}} + xS_{\mathrm{skyr}}$, which is fully analogous to the formula for the conductance $\sigma_{\mathrm{total}} = (1-x)\sigma_{\mathrm{fm}} + x\sigma_{\mathrm{skyr}}$. In cases where σ_{fm} is larger than σ_{skyr}, the influence of σ_{skyr} is even more significant onto the total Seebeck coefficient. This analogy means that we may use the same argument as discussed in subsection 3.6.4, where we saw that in a MTJ device, an increase in transmission due to a skyrmion should generally be easier to measure than a decrease in transmission. Assuming that the skyrmion covers only a smaller area of the total heated area in a Seebeck measurement, it becomes clear that we prefer a small absolute value of the Seebeck coefficient of the ferromagnetic background and a larger absolute value of the Seebeck coefficient including the skyrmion. To account for this in the discussion, it is more reasonable in this case to define the non-collinear MTEP with respect to the ferromagnetic background by dividing only by the absolute value of S_{fm}, instead of the minimum of both coefficients. The result is displayed in figure 4.4, and it shows that the most promising region for MTEP measurements is likely the negative peak around 0.05 eV below E_{F} .

The temperature dependence of the Seebeck effect is plotted in figure 4.5. Here we see a clear trend for the skyrmion system, where the Seebeck coefficient drops continuously with rising temperature. This can be explained directly using the energy dependent transmission curve in figure 3.6. The derivative of the energy dependent transmission through the skyrmion cell is always positive at E_{F} and has a positive curvature. A positive slope of the transmission curve means that the system is called a n-conductor, and directly

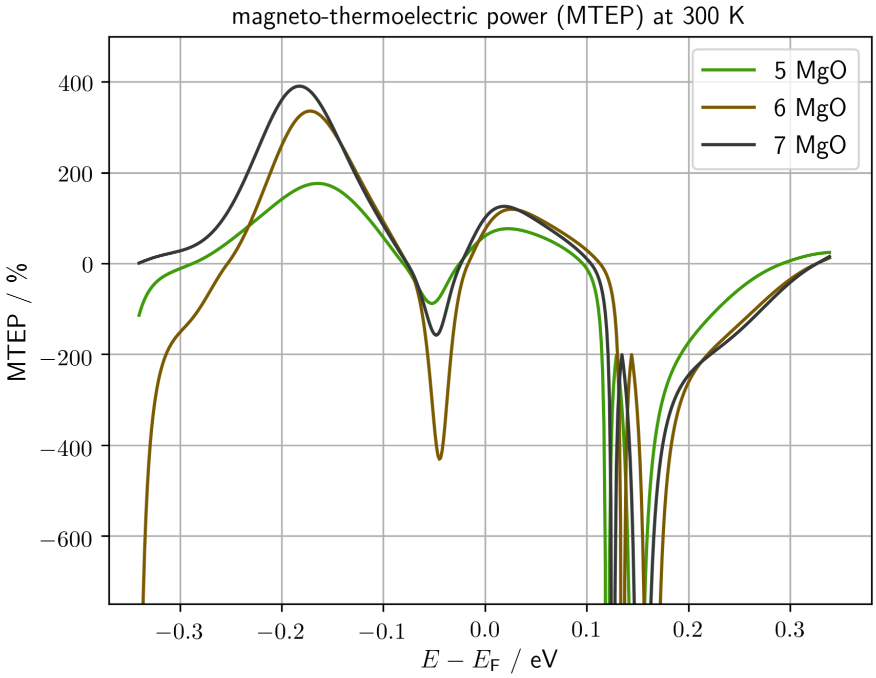

Figure 4.3: The energy dependent MTEP ratio at 300 K . Between 0.1 and 0.2 eV above E_F, as energy increases, the Seebeck coefficients for all three thicknesses first reach zero in the ferromagnetic case, and at a bit higher energy for the skyrmion case, which causes two consecutive negative poles for each thickness in this region.

leads to a negative Seebeck coefficient [174]. The increased temperature means that not only the slope of the transmission at one particular energy is taken into account, but the average slope of the transmission, weighted by the derivative of the distribution function. This means that at larger temperatures, the transmission over a wider energy window becomes relevant, where the positive curvature leads in a larger effective slope of the transmission.

The energy dependent transmission curves in the ferromagnetic case are more complex, leading to a slightly more complex temperature behaviour of the Seebeck coefficient. Particularly at larger barrier widths, we see a small dip in the transmission curves at E_F. This dip directly leads to a low Seebeck coefficient at low temperatures. Only above 150K the Seebeck coefficient for 6 and 7 MgO monolayers overcomes the vicinity of the dip. When the temperature is increased further, the Seebeck coefficients drop drastically due to the positive slope above the dip. Around 400 K, the transmission peak below E_F starts to influence the Seebeck coefficient, which stops the decline.

The results for the Seebeck coefficient and the discussion show that detection of skyrmions using the Seebeck coefficient is, in principle, possible. But for the Seebeck effect, the same arguments regarding the increase and decrease of the effect size apply as for the TNCMR effect, which is explained in section 3.6.4. This means that a change of the Seebeck coefficient should be much easier to observe when the absolute value in the ferromagnetic

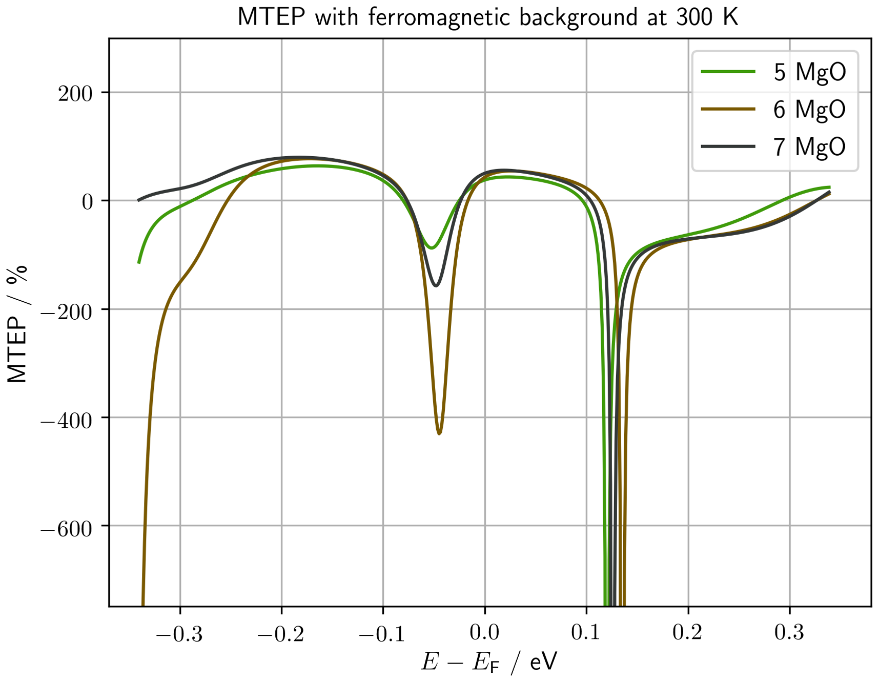

Figure 4.4: The energy dependent MTEP ratio with respect to the ferromagnetic background at 300 K . By dividing only by S_{fm}, one of the two poles between 0.1 and 0.2 eV above E_F is lost.

cell is very small and is increased by a skyrmion. According to our results and the general reasoning on the Seebeck effect and its dependence on the transmission curve, this situation is difficult to achieve for the Seebeck effect, since the smoothing of the transmission curves due to the skyrmion generally leads to smaller absolute values of the Seebeck effect. But this general rule does not apply to all energies, and there is room for exceptions.

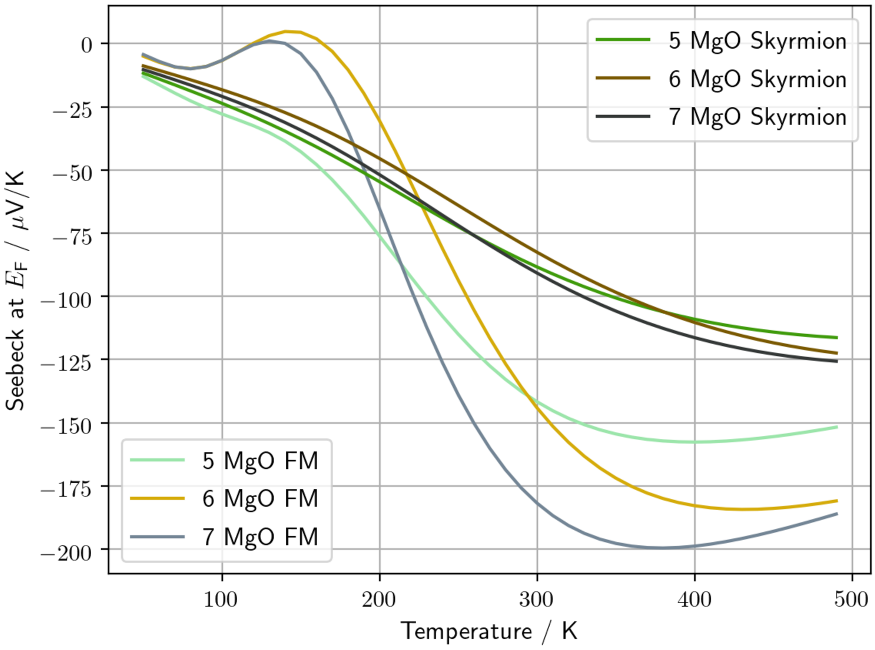

Figure 4.5: The temperature dependent Seebeck coefficient at E_{F} for both the ferromagnetic and the 5×5 skyrmion system.

Chapter 5

Detection of antiferromagnetic skyrmions

5.1 Motivation to use antiferromagnetic skyrmions

While magnetic skyrmions have already been created, manipulated, and observed in many different materials, they have some drawbacks that make their technological use challenging. For example, when a skyrmion is moved on a racetrack using an electric current, the skyrmion Hall effect will push the skyrmion perpendicular to the current direction against the racetrack boundary [39]. This results in significant drag or even destruction of the skyrmion when it is pushed against the boundary, which is not desirable. Since the skyrmion Hall effect is proportional to the topological charge Q, one possible solution to this issue is to replace the ferromagnetic host material with a fully compensated antiferromagnetic material [175]. In this case, the antiferromagnetic skyrmion, like in figure 2.14, can be described by a ferromagnetic skyrmion on each of the two sublattices, whose topological charges, and thus skyrmion Hall angles, effectively sum up to zero [176]. Additionally, antiferromagnetic skyrmions can be moved with much smaller current densities [176] and at faster speeds [177] than ferromagnetic skyrmions, making their application more energy efficient. While antiferromagnetic skyrmions have not yet been observed experimentally, Amin et al. [178] demonstrated the generation and control of antiferromagnetic merons and antimerons, which are similar to antiferromagnetic skyrmions from the perspective of detection in my work.

An alternative approach are synthetic antiferromagnetic materials [113, 179], where two separate ferromagnetic layers with opposite magnetization directions are combined. In this case, the forces due to the skyrmion hall effect on the two connected skyrmions in the two layers have opposite sign and cancel each other. Yet another alternative are ferrimagnetic skyrmions, which, similarly to antiferromagnetic skyrmions, can be described by two fer-

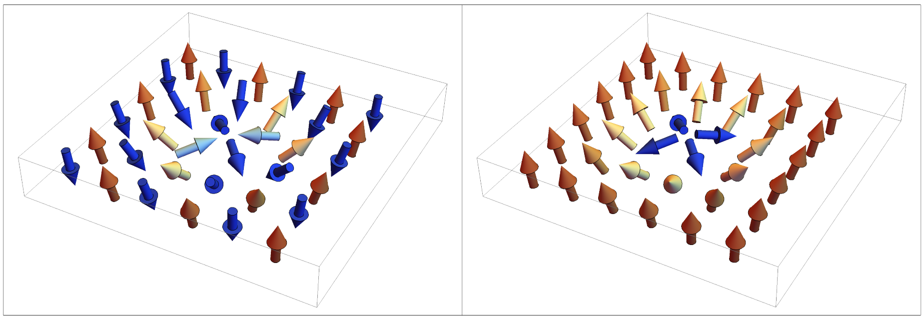

Figure 5.1: Left: Orientation of the magnetization vectors for the antiferromagnetic skyrmion of size 6 × 6 used in this section. Right: The corresponding ferromagnetic skyrmion of the same size for comparison.

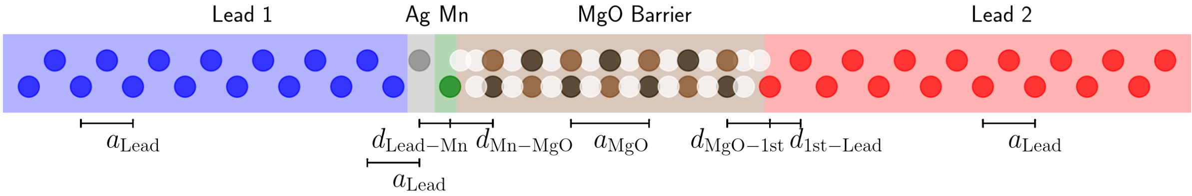

Figure 5.2: The geometric structure of the V/Ag/Mn/MgO/Cu barrier used as the host system for antiferromagnetic skyrmions in this calculation. The atomic positions are the same as those used in chapter 3.

romagnetic skyrmions on two sublattices. However, unlike antiferromagnetic skyrmions, the two sublattices are chemically different and typically not fully compensated. Fully compensated ferrimagnetic skyrmions are possible and are expected to provide AFM-like dynamics [180]. Ferrimagnetic skyrmions have already been experimentally observed in GdFeCo films grown on Pt [181], and a few of the advantages expected for antiferromagnetic skyrmions over ferromagnetic skyrmions have been experimentally confirmed for ferrimagnetic skyrmions as an intermediate step. For example, it was demonstrated in [181] that the skyrmion Hall angle for the experimentally observed ferrimagnetic skyrmions is significantly smaller, and the skyrmion velocity is faster than that of ferromagnetic skyrmions.

While there are many possible ways to detect magnetic skyrmions in ferromagnetic materials, detecting antiferromagnetic skyrmions is much more challenging [113, 42]. Three approaches were discussed, including the topological spin Hall effect (THSE) [182], magnetic force microscopy [113], and X-ray magnetic linear dichroism photoemission electron microscopy (XMLD-PEEM) [178]. However, none of these approaches are well suited for solid state devices [183], for the same reasons as their ferromagnetic counterparts are not ideal for the detection of ferromagnetic skyrmions. In [183], the possibility to use MTJs to detect antiferromagnetic skyrmions is discussed, where the antiferromagnetic layer is placed between one of the ferromagnetic contacts and the insulating layer. In this chapter, I present a new approach by applying the concept of the TNCMR effect to antiferromag-

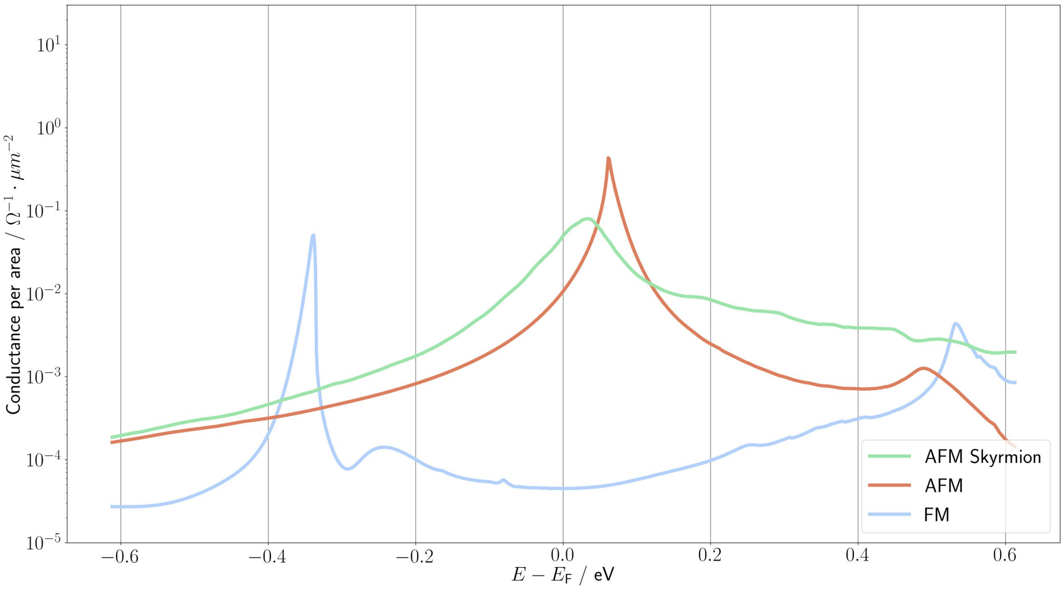

Figure 5.3: The energy dependent transmission through the V/Ag/Mn/MgO(7)/Cu barrier with either a ferromagnetic or antiferromagnetic structure, or an antiferromagnetic skyrmion in the Mn layer. For most energies, the appearance of the skyrmion slightly increases the transmission. The transmission peak just above the Fermi energy is smeared out by the antiferromagnetic skyrmion, similar to the transmission peaks in the ferromagnetic system in the presence of a ferromagnetic skyrmion. The transmission in the case of a ferromagnetic manganese layer is completely different and much smaller around the Fermi energy.

netic skyrmions, demonstrating that the ferromagnetic contacts are not necessary for the detection of antiferromagnetic skyrmions with a tunneling barrier.

5.2 Results

In order to model an antiferromagnetic skyrmion within a layer structure suitable for TNCMR calculations, I replace the ferromagnetic Fe layer in the V/Fe(1)/MgO(7)/Cu skyrmion structure with a manganese monolayer combined with a silver monolayer. This is because a manganese monolayer grown on silver is expected to have a c2×2 antiferromagnetic ground state [44], making it a more realistic host for the antiferromagnetic skyrmion than the ferromagnetic iron monolayer. As a result, the exchange of the skyrmion host layer leads to a V/Ag(1)/Mn(1)/MgO(7)/Cu structure, displayed in figure 5.2, which I use in this chapter. For simplicity, the positions of atoms are the same as those used in the V/Fe/MgO/Cu system calculations, only with the first monolayer of the vanadium lead adjacent to the magnetic layer being replaced by silver atoms, and the iron replaced by manganese atoms.

The numerical parameters used for the calculation are explained in appendix A. The antiferromagnetic structure used for this calculation is displayed on the left of figure 5.1.

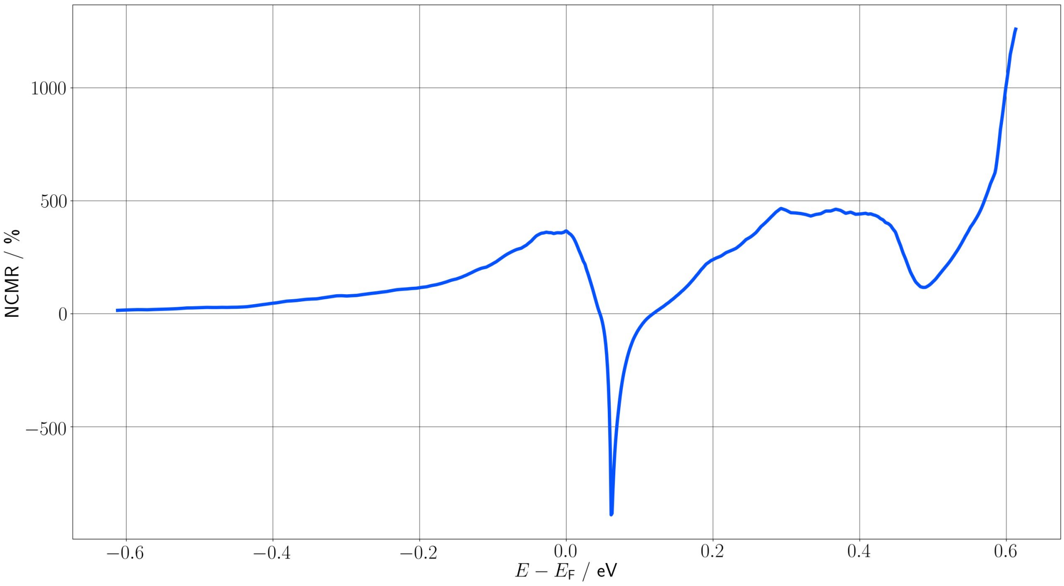

Figure 5.4: The resulting TNCMR effect is caused by the appearance of the antiferromagnetic skyrmion in the antiferromagnetic host material. Due to the described change of the transmission function, the TNCMR effect is positive for most energies but shows a sharp negative dip at the position of the transmission peak in the antiferromagnetic system.

The resulting energy dependent TNCMR effect in figure 5.4 shows a similar behavior to the collinear TNCMR in figure 3.7. At most energies, the non-collinear structure increases the conductance. But, as in the collinear case, the appearance of the non-collinear structure depresses sharp peaks in the conductance, leading again to negative TNCMR effect peaks.

Another interesting change in the energy dependent conductance due to the antiferromagnetic skyrmion, which is displayed in figure 5.3, is the shift of the conductance peak. The Seebeck effect at the top of a wide conductance peak is very small [184], but its absolute value gets large in the proximity of the top. This means that a shift in the conductance peak can lead to a significant change in the Seebeck effect. This change is shown in figure 5.5, where the most drastic change occurs about 0.05eV above the Fermi energy. Here, the Seebeck effect switches from its largest negative value to zero when the antiferromagnetic skyrmion shifts the conductance peak to that position. At the Fermi energy, the change is smaller but still significant. Besides this, the non-collinear structure generally smooths energy dependent conductance, leading to an overall weaker Seebeck effect. This holds even more at higher temperatures, as can be seen in figure 5.6.

The temperature dependence of the Seebeck effect at the Fermi energy is shown in figure 5.7. This curve is relevant if we assume that the calculated Fermi energy is accurate. In this case, we see that the Seebeck coefficient is reduced by the presence of the antiferromagnetic skyrmion across the entire considered temperature range, which makes detection via the TNCMS difficult for the same reasons explained in section 3.6.4.

Although the assumed antiferromagnetic system and the antiferromagnetic skyrmion con-

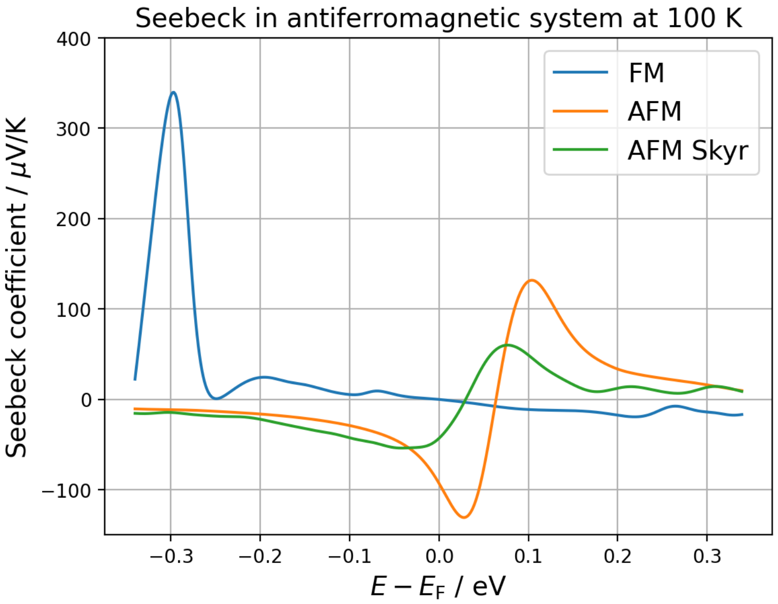

Figure 5.5: The resulting energy dependent Seebeck effect at 100K through the V/Ag/Mn/MgO(7)/Cu barrier. The energy dependent Seebeck coefficient has a very similar shape for the antiferromagnetic system with and without the antiferromagnetic skyrmion. In the presence of the antiferromagnetic skyrmion, the Seebeck coefficient curve is slightly flattened and shifted to lower energies, similar to the transmission peak in 5.3. The Seebeck coefficient in the hypothetical ferromagnetic case is much smaller for energies close to the Fermi energy, and has a sharp peak at the lower end of the calculated energy spectrum.

sidered here are admittedly artificial and unlikely to be experimentally reproduced in this specific material, the calculated results still demonstrate that the occurrence of antiferromagnetic skyrmions could, in principle, lead to transmission changes large enough for detection. Patience is required in this matter, since the observable effect is highly dependent on the Fermi energy, and Fermi level engineering may be necessary to make a sufficiently large signal accessible.

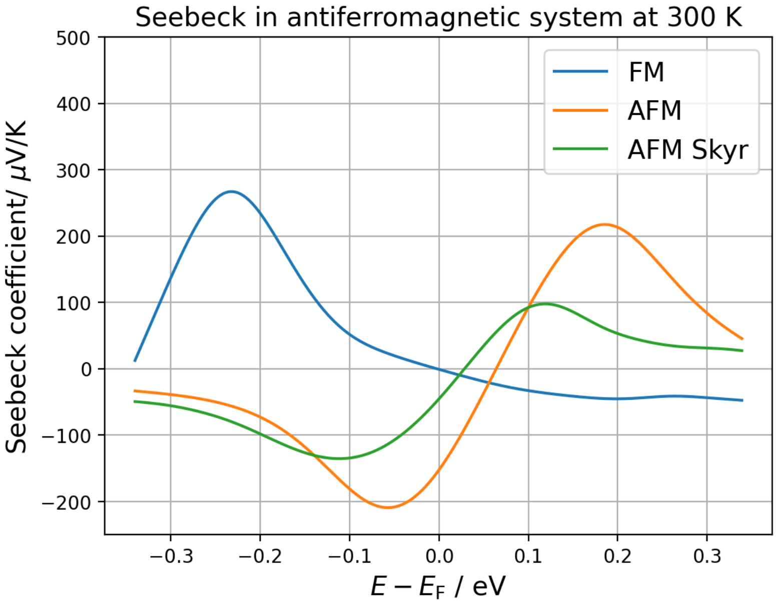

Figure 5.6: The resulting energy dependent Seebeck effect at 300K through the V/Ag/Mn/MgO(7)/Cu barrier. When the temperature is increased, both energy dependent Seebeck coefficient curves still have the same qualitative behavior, only with the peaks becoming larger in both height and width.

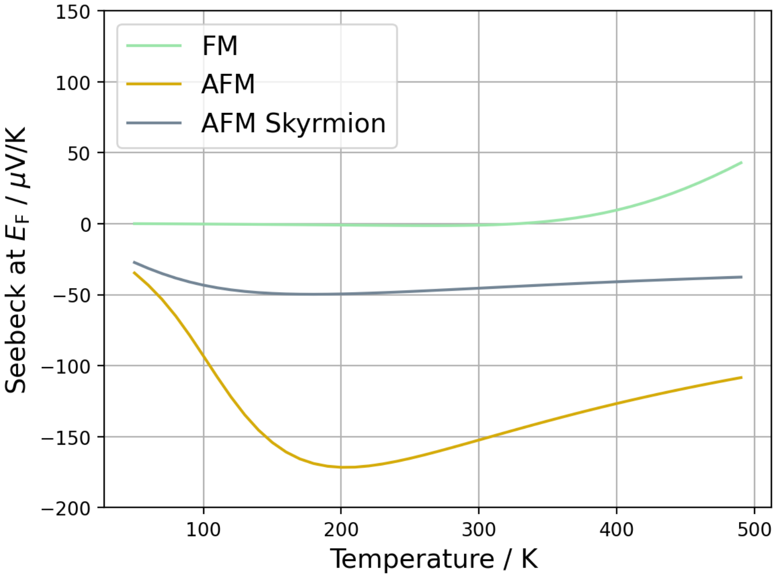

Figure 5.7: The resulting temperature dependent Seebeck effect at the Fermi energy through the V/Ag/Mn/MgO(7)/Cu barrier.

Chapter 6

TMR for characterization of magnetic structures

Magnetic skyrmions are not the only magnetic structures (see section 2.9) occurring in thin magnetic films, and it is important to be able to experimentally distinguish between these structures. For SP-STM and STM, the characterisation of magnetic structures is already thoroughly investigated [185, 36, 45]. But when no imaging tool like STM is available, and only the signal from an MTJ can be used, distinguishing between structures like skyrmions and magnetic bubbles [186, 187, 188, 126, 189] becomes very difficult. But as I will demonstrate, even without any spatial resolution, it is possible to use MTJs to test the symmetry properties of magnetic structures, which then allows one to distinguish skyrmions from trivial magnetic bubbles. The approach in this work is based on a tunnel magnetoresistance (TMR) [190] setup, as sketched in figure 6.1. It basically consists of an insulating layer sandwiched between two magnetic layers. The bottom magnetic layer is out-of-plane magnetized and may contain movable non-collinear structures. The top magnetic layer, on the other hand, is magnetized in-plane, and its magnetization direction can be rotated. While the spatial resolution compared to STM is lost, it is possible to show that several measurements with different reference magnetization directions can be used to gain information about the symmetry properties of magnetic structures.

The idea is that the symmetry properties of magnetic structures are reflected by the change of the total transmission when the in-plane angle ϕ_{ref} of the reference magnetization is rotated. Ideal skyrmions exhibit rotational symmetry [191, 192], which means that, just like in the out-of-plane ferromagnetic case, the TMR contribution of the transmission through the structure is independent of ϕ_{ref}. Higher order skyrmions and antiskyrmions lack rotational symmetry, but it can still be shown that TMR for the ideal structures remains isotropic with respect to ϕ_{ref}. For general non-collinear structures, this is not the case. After a brief theoretical discussion, this principle is demonstrated through DFT calculations, showing that a skyrmion, the ferromagnetic background, and a bubble (as topologically trivial non-collinear structure) can be distinguished by TMR measurements in MTJs.

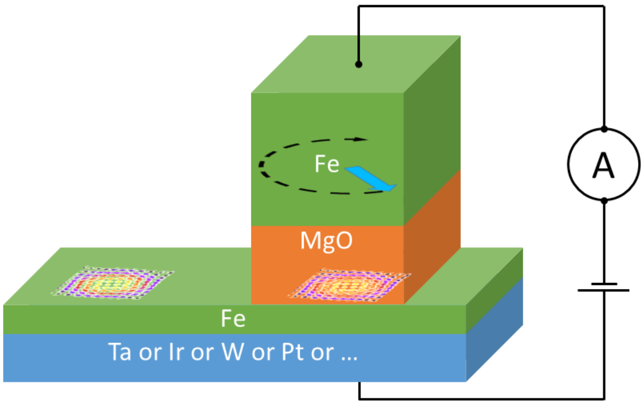

Figure 6.1: The geometrical structure of the system. The skyrmions are located in the xy-plane in the thin iron monolayer. The presence of a non-collinear magnetic structure in the MTJ alters the conductance and can therefore be detected. In general, the conductance depends on the direction of the reference magnetization. This work focuses on an in-plane rotation. Adapted from [O1]. Copyright (2019) by the American Physical Society.

6.1 Theoretical expectation

Let's assume the magnetization in the reference layer lies in the plane

$$\vec{e}_{\text{ref}} \propto \begin{pmatrix} \cos\phi_{\text{ref}} \\ \sin\phi_{\text{ref}} \\ 0 \end{pmatrix}, \tag{6.1}$$

and the magnetization in the iron monolayer points along

$$\vec{S}_{\text{skyr}} \propto \begin{pmatrix} \cos\Phi\sin\Theta \\ \sin\Phi\sin\Theta \\ \cos\Theta \end{pmatrix}. \tag{6.2}$$

Then, in case of pure TMR, the relationship between the tunneling current through the junction and the direction of the reference magnetization is described by [193]

$$\Delta I \propto \vec{S}_{\text{skyr}} \cdot \vec{e}_{\text{ref}} \propto \sin\Theta\cos(\Phi - \phi_{\text{ref}}). \tag{6.3}$$

As in [188, 126, 189], it is assumed that the skyrmionic structures can be described by $\Theta(r)$ and $\Phi(\phi) = \nu\phi + \eta$, given that the skyrmion center is located at the origin of the polar coordinate system. The order of the skyrmion is determined by the vorticity ν, which is an integer number. The parameter η is the helicity. Integration over the entire plane leads to the total current through the barrier:

$$\begin{aligned}
\Delta I_{\text{total}} &= I_{\text{TMR}} \int_0^\infty \mathrm{d}r \int_0^{2\pi} \mathrm{d}\phi \; r \sin\Theta \cos(\Phi - \phi_{\text{ref}}) \\
&= I_{\text{TMR}} \int_0^\infty \mathrm{d}r \; r \sin(\Theta(r)) \int_0^{2\pi} \mathrm{d}\phi \;\; \cos(\nu\phi + \eta - \phi_{\text{ref}}) \\
&= I_{\text{TMR}} C \int_0^{2\pi} \mathrm{d}\phi \;\; \cos(\nu\phi + \eta - \phi_{\text{ref}}) \\
&\propto \begin{cases} 2\pi \cos(\eta - \phi_{\text{ref}}) & \text{, if } \nu = 0 \\ 0 & \text{, if } \nu \in \{\dots, -2, -1, 1, 2, \dots\} \end{cases}
\end{aligned}$$

The possibly complicated behaviour of $\Theta(r)$ only results in a number C, which is independent of ϕ_{ref}. This short analysis shows that the current perpendicular through skyrmionic structures can indeed be expected to be independent of the in-plane magnetization direction of the reference layer. For a topologically trivial structure with $\nu = 0$, this is not the case.

6.2 The TMR system

In the next step, we want to explore this idea more thoroughly by supporting it with DFT calculations. The basic TMR setup used is a Cu/Fe/MgO/Fe/Cu structure, which thus contains two magnetic layers separated by an insulating layer. In this case, the insulating layer is crystalline MgO. The first magnetic layer is an atomic monolayer of iron, containing the magnetic structure with an out-of-plane magnetized background, and it is connected to a copper lead. The second magnetic layer is in-plane magnetized and serves as a reference layer, which is also connected to a copper lead. The insulating MgO and the magnetic reference layer are 3 and 5 monolayers thick, respectively. The atomic positions are the same as in section 3, with the distances documented in table 3.1. As in [194], the copper leads are described by a bcc structure.

6.3 Magnetic structure model

While realistic skyrmions are too large for an ab-initio treatment, we use artificial structures with the correct topological charge to demonstrate the principle. Besides a ferromagnetic structure with out-of-plane magnetization, we consider a Néel skyrmion and a bubble as trivial non-collinear magnetic structure. Both structures are displayed in figure 6.2. The $\Theta(r)$ dependence is the same for both non-collinear structures and is described by the analytical formula 3.2 for a domain wall profile, as in [149].

In the case of the bubble, the angle Φ is set to 0° for all atoms, meaning that the in-plane component of the magnetization always points along $\propto \vec{e}_x$, which corresponds to the [100] direction of the lead material. For the skyrmion, the angle Φ for each atom is chosen so that the in-plane component of the magnetization points directly away from the skyrmion center.

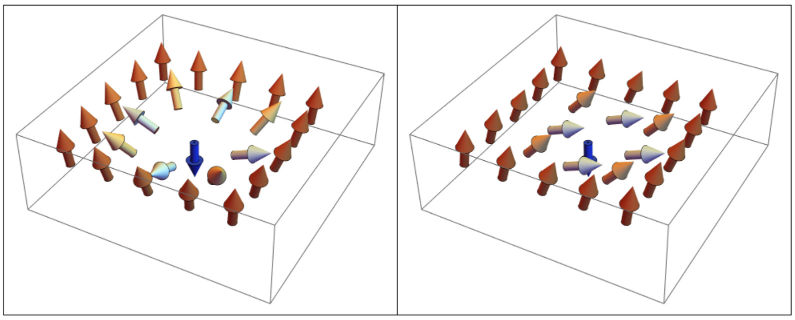

Figure 6.2: The artificial non-collinear structures used in our calculations. On the left is the Néel skyrmion, and on the right is the topologically trivial bubble. Adapted from [O1]. Copyright (2019) by the American Physical Society.

6.4 Results

We calculated the total transmission at the Fermi energy for all three non-collinear structures for different angles ϕ_{ref} with a step size of $\Delta\phi_{\text{ref}} = 1°$. The results in figure 6.3 clearly show a large directional dependence in case of the bubble. In case of the skyrmion and the ferromagnetic structure there is still an anisotropy due to tunneling anisotropic magnetoresistance (TAMR) [25, 195, 142] observable, but it is much smaller in comparison to the bubble. The transmission in case of the skyrmion is slightly larger than the transmission through the ferromagnetic cell, which can be explained by tunneling non-collinear magnetoresistance (TNCMR) [196, 36, 35][O1]. This means that contributions from TMR, TAMR, and TNCMR are observable in this chart.

We thus conclude that non-collinear magnetic structures can indeed be categorized as either trivial or skyrmionic, as long as the skyrmion shape can be described as in [188, 126, 189], by measuring the out-of-plane conductance change in a MTJ when the reference magnetization direction is rotated. Based on these results, we propose a device consisting of a row of several MTJs on a racetrack. As sketched in figure 6.4, the magnetization direction of the reference layer within each MTJ is fixed using shape anisotropy. The magnetic structure could then be moved on the racetrack, passing the TMR junctions. If the conductance through all MTJs is essentially the same, it strongly indicates that the structure is skyrmionic. If the conductance through the MTJs deviates significantly, the structure cannot be skyrmionic.

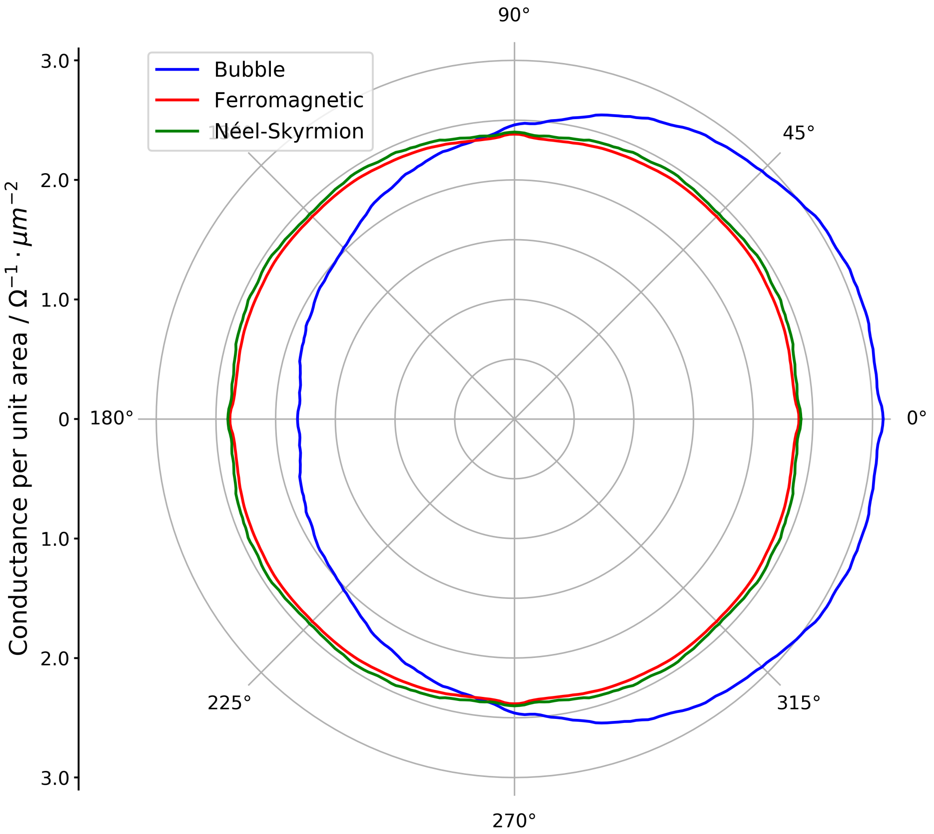

Figure 6.3: The transmission through the MTJ as a function of the magnetization direction of the reference layer for three different magnetic configurations. The magnetization direction is rotated in-plane, with $\phi = 0°$ representing the [100] direction of the lead material.

6.5 Extension to bimerons

Bimerons, which also have topological charge of 1, have some advantages compared to skyrmions, which makes them an interesting research subject. Göbel et al. [29] explained that while bimerons allow the measurement of the pure THE effect, which is not possible for regular out-of-plane skyrmions, their in-plane magnetized racetrack background also produces a smaller stray field, which is helpful for practical applications.

The theoretical argument from subsection 6.1 can be extended to the in-plane version of skyrmions, known as bimerons. As explained in [29], a bimeron can be modeled by rotating all angles of the skyrmion by 90° around an in-plane axis using the rotation matrix $R_x(90°)$:

$$R_x(90^\circ) = \begin{pmatrix} 1 & 0 & 0 \\ 0 & 0 & -1 \\ 0 & 1 & 0 \end{pmatrix} \tag{6.4}$$

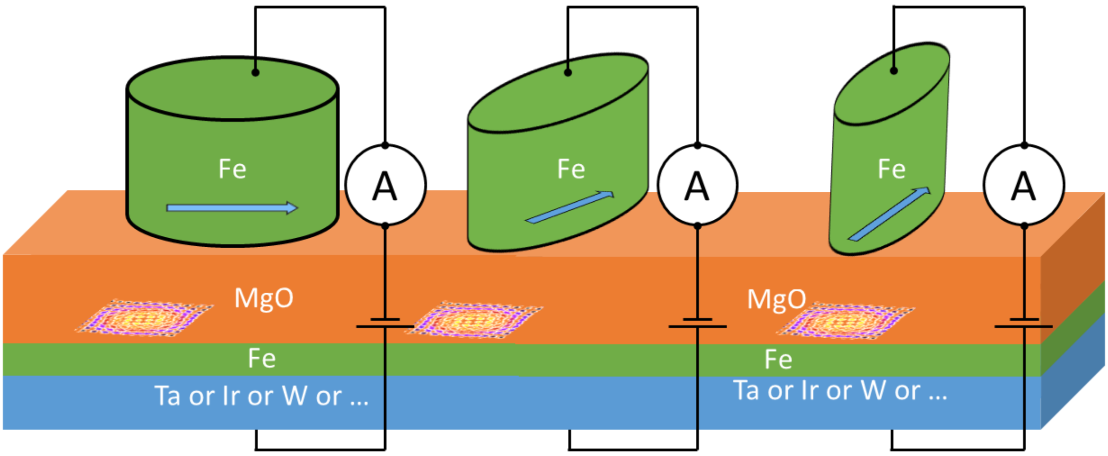

Figure 6.4: The geometrical structure of the proposed device. The skyrmions are located in the xy-plane within the thin iron monolayer. The presence of a skyrmion in the MTJ alters the conductance and can therefore be detected. Adapted from [O1]. Copyright (2019) by the American Physical Society.

This means that the bimeron structure is described by

$$\vec{S}_{\mathrm{bimeron}} = R_x(90^\circ) \cdot \vec{S}_{\mathrm{skyr}} \propto \begin{pmatrix} \cos\Phi \sin\Theta \\ -\cos\Theta \\ \sin\Phi \sin\Theta \end{pmatrix} . \tag{6.5}$$

If we now also rotate the reference magnetization direction in the same way to

$$\vec{e}_{\mathrm{ref}} \propto R_x(90^\circ) \cdot \begin{pmatrix} \cos\phi_{\mathrm{ref}} \\ \sin\phi_{\mathrm{ref}} \\ 0 \end{pmatrix} = \begin{pmatrix} \cos\phi_{\mathrm{ref}} \\ 0 \\ \sin\phi_{\mathrm{ref}} \end{pmatrix} , \tag{6.6}$$

then the scalar product of both magnetization directions will be

$$\vec{e}_{\mathrm{ref}} \cdot \vec{S}_{\mathrm{bimeron}} \propto \cos\phi_{\mathrm{ref}} \cos\Phi \sin\Theta + \sin\phi_{\mathrm{ref}} \sin\Phi \sin\Theta = \sin\Theta cos(\Phi - \phi_{\mathrm{ref}}), \tag{6.7}$$

which is the same result as for the skyrmion in equation 6.3. This implies that within this simplified model, we can roughly expect the same possibility of detecting bimerons as for standard out-of-plane skyrmions. This arrangement is sketched in figure 6.5.

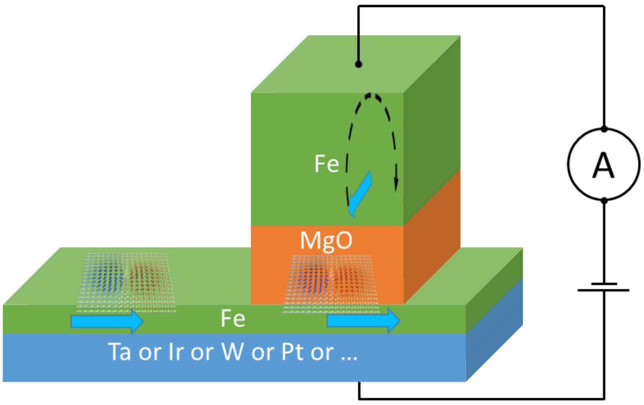

Figure 6.5: The geometrical structure of the proposed device adapted to the detection of bimerons. A rotation of the reference magnetization direction (shown as rotating blue arrow in the iron bulk above the MgO layer) in the plane perpendicular to the magnetization of the ferromagnetic background of the bimeron layer (shown as blue arrows to the right) is not expected to change the conductance if the bimeron is fully located inside the sensor area. A larger image of the bimeron is provided in figure 2.15. Adapted from [O1]. Copyright (2019) by the American Physical Society.

Chapter 7

Summary and outlook

With this work I provide a deeper insight into how MgO-based tunnel junctions can be used to detect non-collinear magnetic structures such as skyrmions or antiferromagnetic skyrmions. Although several approaches already exist, including the topological Hall effect (THE) and spin-polarized scanning tunneling microscopy (SP-STM), ongoing discussions and research [12, 45, 197, 198, 30] indicate that the optimal method for efficient skyrmion detection method is still not clear. This means that there is still a great need for further research in this area.

The calculated results show that when the skyrmion hosting layer is sandwiched between a vanadium lead and an MgO barrier (here V/Fe/MgO/Cu), the presence of a skyrmion can drastically change the transmission function through the insulating MgO barrier. Surprisingly, it turns out that for wide energy ranges, the skyrmion increases the transmission through the V/Fe/MgO/Cu system by a large amount. This intriguing result can be explained by a novel scattering mechanism, which allows coherent electronic states from the vanadium, which are not able to tunnel through the MgO barrier effectively, to scatter at the skyrmion. The scattering overlaps them with Δ_1-like states, enabling a much more efficient tunneling through the MgO barrier.

However, the calculated transmission through V/Fe/MgO/Cu is not increased for all energies by the skyrmion. A deeper analysis of the involved electronic states shows that quantum well states (QWS) in the thin iron layer have a significant influence on the overall transmission through the barrier and are sensitive to magnetic distortions in the barrier. This sensitivity is partially caused by the energy broadening [162] and thereby flattening of the QWS peaks due to perturbation from skyrmions, which are nothing else than a defect in this context. Another contribution from the QWS comes from tunneling anisotropic magnetoresistance (TAMR), which is important in the V/Fe/MgO/Cu system for a specific quantum well state, whose contribution to the transmission is shown to be crucially depending on spin-orbit coupling and, consequently, the magnetization direction. This finding underlines that under the right conditions, a small contribution in the Hamiltonian of a system can lead to large differences in observable effects. From a methodological perspective, this result again proves the value of *ab initio* calculations, which include subtle effects like this, which might otherwise be overlooked when using only simplified model systems.

In summary, depending on the position of the Fermi level in the material and the temperature, it is possible to either increase or decrease the conductance through the barrier with a skyrmion. Either way, the change in conductance can, in principle, be used to detect a skyrmion. We call the overall effect the tunneling non-collinear magnetoresistance effect (TNCMR), as it goes beyond the previously described NCMR [35] or TXMR [36] effect.

It is important not to overlook more exotic topological structures like merons and non-ferromagnetic base materials, as they have some key advantages that prove crucial [199, 29, 200]. While for some time synthetic antiferromagnetic skyrmions [113, 179] were envisioned as the way to go, non-synthetic antiferromagnetic skyrmions and merons have gained more attention due to their intriguing properties [201, 178, 202]. In this work, I showed that the V/X/MgO/Cu type structure not only works for ferromagnetic materials X to detect regular skyrmions, but can also, in principle, be extended to antiferromagnetic materials to detect antiferromagnetic skyrmions, which are even more challenging to detect using other methods. While the calculated TNCMR effect in the assumed model system was not as large as for the comparable V/Fe/MgO/Cu skyrmion system, it still reached a magnitude of about 300% at the Fermi level.

The pure change of conductance, summarized as the TNCMR effect, is not the only way to measure transmission changes. The slope of the transmission can also be measured, as it is the underlying physical quantity behind the Seebeck effect. The change in this due to non-collinear magnetic structures is called tunneling non-collinear magneto Seebeck effect (TNCMS) in this work. However, the analysis in this work demonstrates that the appearance of skyrmions tends to smooth the transmission function by the energy broadening of the peaks, which consequently tends to reduce the absolute magnitude of the Seebeck effect. This is harder to measure than an increase, when the affected area of the sensor is small. The same general behavior of TNCMS is also demonstrated in the analyzed antiferromagnetic system.

Finally, I also explore the topology of skyrmionic structures and how the topological nature can be determined using the tools of magnetic tunnel junctions, irrespective of high spatial resolution. It turns out that a setup of a small number of magnetic tunnel junctions, which are sequentially passed by a magnetic structure on a racetrack, can in combination recognize skyrmionic structures from their measured TMR signals.

To provide an outlook, I want to highlight that the proposed novel scattering mechanism, responsible for the drastic conduction increase due to a skyrmion for most energies through the V/Fe/MgO/Cu system, not only provides a deeper understanding of the underlying physics, but also provides a possible approach for an experimentalist to find suitable materials where a large TNCMR ratio may actually be observed. The mechanism allows us to deduce the following rule of thumb: a material, which will lead to a large positive TNCMR ratio also leads to a large contact resistance in the ferromagnetic case. For example, for the ferromagnetic V/MgO/Fe system the large contact resistance is mentioned in [155]. This could allow for the screening of promising TNCMR materials without needing to create and control skyrmions. However, it may be hard to find a material X that leads to both a large TNCMR effect and the occurrence of skyrmions in a X/Fe/MgO/Cu structure simultaneously.

To simplify the search for suitable materials, it can be helpful to consider the fact that the lead material X_{TNCMR}, which is primarily responsible for TNCMR, is not required to directly contact the skyrmion host layer. Whereas the material X_{DMI}, responsible for the appearance of skyrmions via DMI, must directly touch the magnetic skyrmion layer, but it can potentially be very thin. A combination of both materials in an $X_{\mathrm{TNCMR}}/X_{\mathrm{DMI}}$/Fe/MgO/Cu structure could lead to the desired result, although growing clean interfaces in such a system is probably even more difficult than in X/Fe/MgO/Cu. For example, V/Au/Fe/MgO/Cu is a candidate for this type of system. But even though it is difficult to handle, this type of structural complexity should not be seen as a show stopper, as other similarly complex structures have already been realized. The concept of synthetic antiferromagnetic skyrmions [113, 179, 203] also relies on a complex arrangement of several layers, where two separate ferromagnetic layers are antiferromagnetically exchange-coupled, forming a bilayer system. Another example is the actually fabricated Pt/Co/Fe/Ir multilayer stack [204], where the DMI vectors from the interfaces effectively sum up to generate a larger DMI vector.

Perhaps the ideal tunnel barrier does not even have to be made of MgO. Li et al. [205] proposed a very large non-collinear magnetoresistance effect in a Fe_3GeTe_2-based van der Waals tunnel junction, which, like the effect described in this work, goes beyond changes of the local density of states and utilizes the symmetry of the involved electronic states.

In summary, we can say that the search for materials suitable for actual skyrmionic devices is far from over. It is, in fact, comparable to finding a needle in a haystack of options. Theory based screening guidelines are of great value for gaining an overview. *Ab initio* methods help to discover these guidelines and can evaluate potential material candidates without needing to actually manufacture all of them.

Appendices

Appendix A

Numerical parameters

The quality of computational results in DFT is highly dependent on sufficiently fine numerical parameters. But high numerical parameters lead to higher computational demand and, therefore, increased energy cost. This means that the parameters have to be carefully balanced, which is especially difficult in this work since the unit cells, including the skyrmions are almost prohibitively large. The most critical numerical parameter is the angular momentum cut-off, which I set to $l_{\mathrm{max}} = 2$ for transport calculations. This corresponds to d orbitals and is sufficient for the elements considered in this work. For the self-consistent convergence calculations, I used a cut-off of $l_{\mathrm{max}} = 3$, which leads to a more accurate electron density description used for the potentials.

A.1 Convergence parameters

The self-consistent convergence of the potential was done only for the cells without any non-collinear structure, which is justified by the examination in section B. In all three directions, including the out-of-plane direction, the long unit-cell is repeated infinitely. This means that within the self-consistent calculation, the materials of the two leads directly touch each other at the ends of the long unit cell. To ensure that this inaccuracy has no effect on the transport calculation, I later selected the potential from an atom deeper within each lead of the unit cell as the edge potential used in the decimation step for the transport calculation.

For the reference system, I considered all atoms in a sphere of radius 2.8 a_{Lead}. The energy contour integration path, sketched in figure 2.1, was chosen to start at $E_{\mathrm{B}} = -1$ Ry, encircling $N_{\mathrm{P}} = 10$ Matsubara poles at a temperature of $T = 300$ K . Along the 3 parts of the integration path, I used $N_1 = 10$, $N_2 = 42$, and $N_3 = 10$ sampling points. For the integration in reciprocal space, to evaluate expression 2.61, I divided the Brillouin zone into $N_{kx} = N_{ky} = 64$ and $N_{kz} = 3$ sampling points. The 3 sampling points in the z

direction, which is the out-of-plane direction, only resemble differences occurring from the small supercell effect. In the antiferromagnetic cell of section 5.2, I used a $N_{kx} = N_{ky} = 45$ and $N_{kz} = 3$ sampling.

A.2 Parameters for transport calculations

The majority of the computational effort in this work is not due to the self-consistent convergence of the potentials but rather to the transport calculations. In non-equilibrium transport calculations, the physical quantity must be calculated as close as possible to the real energy axis. This means that zero Matsubara poles are circled, and the artificial temperature was set to only $T = 0.2$ K. Close to the real energy axis, the Green function has a much more rugged structure, requiring a much finer sampling of energy and reciprocal space points. Physically, these rugged features of the Green function typically resemble exactly those peaks we are mostly interested in. To meet the required mesh density in the critical areas of the Brillouin zone of the cells without non-collinear structures, I used adaptive meshes in reciprocal space. In the case of non-collinear structures, the peaks were broadened due to the scattering at those structures. Additionally, the Brillouin zones of the supercells (sc) used to describe the non-collinear structures are already significantly smaller. Here, I used only $N_{kx,\mathrm{sc}} = N_{ky,\mathrm{sc}} = 18$ for the mostly used 5×5 supercell, which is equivalent to $N_{kx} = N_{ky} = 90$ sampling points of the base Brillouin zone. For other supercell sizes, I scaled the mesh density linearly, based on the $N_{kx} = N_{ky} = 90$ sampling for the 1×1 unit cell. Like the adaptive reciprocal space meshes, the energy mesh densities depend on the local roughness of the energy dependent transmittance.

In typical KKR calculations, the tunable size of the real space cluster, which is crucial for screened KKR, is used in two different steps of the calculation. First, it is used when calculating the reference system Green function, which heavily influences the accuracy of the outcome of the decimation technique. Second, it is used to determine the bandwidth of the now banded KKR matrix in equation 2.74 for the band matrix inversion function used in the KKR code. When experimenting with different cluster sizes, it turns out that the accuracy of the overall result is much more sensitive to the cluster size in the first step, compared to the outer parts of the banded KKR matrix that are cut off later in the calculation process. For this reason, I chose a cluster radius of 3.8 a_{Lead} but used only 2.8 a_{Lead} for the considered band width in the computationally expensive inversion step without losing much accuracy.

Appendix B

Model validation and assumption analysis

When preparing the calculations, some assumptions and choices had to be made regarding the skyrmion structure and the underlying potential. First of all, I used two different skyrmion structures. One skyrmion structure is obtained from atomistic spin dynamics simulations and the other from an approximate analytical formula. To verify if they are essentially interchangeable for the calculations in this work, I compare the influence of the two different considered skyrmion structures on the energy dependent transmission through the V/Fe/MgO(3)/Cu structure. The result is displayed in figure B.1, and we can clearly see that their effect on the conductance is very similar.

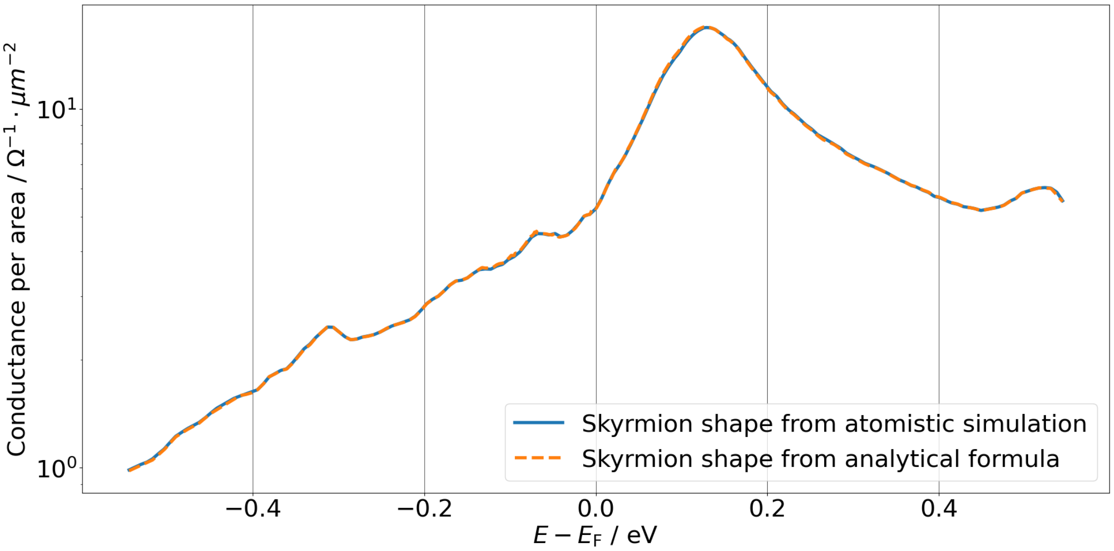

Figure B.1: The energy dependent transmission through the V/Fe/MgO(3)/Cu structure with an analytical skyrmion structure versus the skyrmion from the atomistic spin dynamics simulation. Both are based on the same potential, calculated with very high numerical precision. As expected, both lines are almost indistinguishable.

For simplicity, in most calculations in this work, the skyrmion structure was applied only to the ferromagnetic iron layer. I will indicate this by explicitly stating that the skyrmion is located in a specific layer in the caption of the corresponding graphic. But to explore the influence of this choice, I compared the energy dependent transmission through the V/Fe/MgO(3)/Cu structure in figure B.2 for two situations. In the first situation, the analytical skyrmion is located only in the iron layer. In figure 3.3, we already saw that at least the first underlying vanadium layer is significantly magnetized, so I applied the analytical skyrmion structure to this layer as well. The results clearly show that this change indeed makes some difference, but it is not strong enough to change the overall qualitative result.

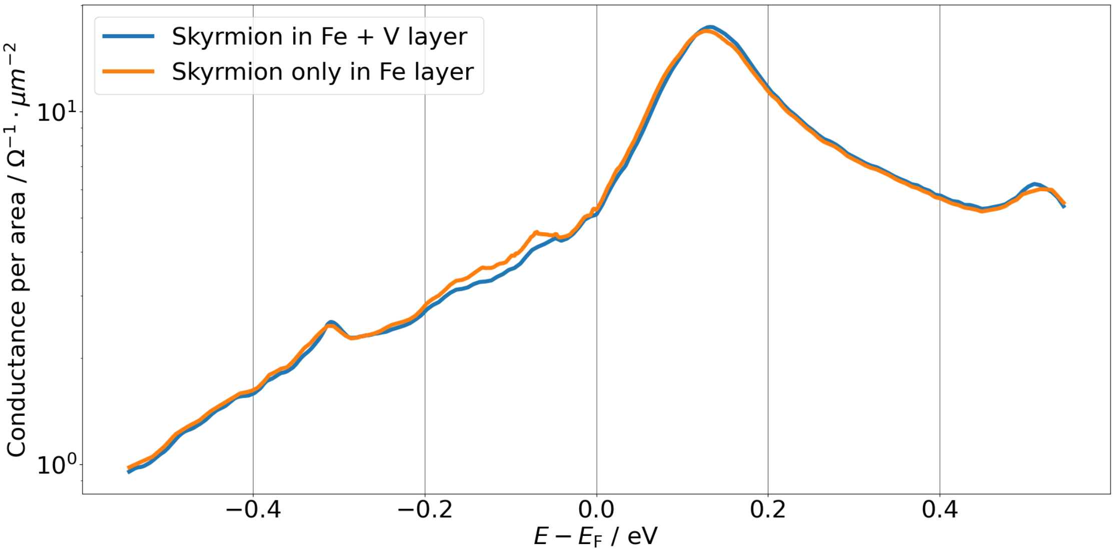

Figure B.2: The energy dependent transmission through the V/Fe/MgO(3)/Cu structure with an analytical skyrmion structure only in the iron layer (orange), and with the same skyrmion structure extended to the first underlying vanadium layer (blue). Tilting of magnetic moments in the first underlying vanadium layer according to the skyrmion structure has some, but not a large influence on the energy dependent transmission.

Another decision which had to be made concerned the self consistent potential. One option was to use a potential that is self-consistently calculated, including the skyrmion structure, but with weaker numerical parameters in terms of angular momentum cut-off, sampling along the energy contour, sampling in reciprocal space, and size of the real space clusters for the repulsive reference system, to make the calculation practically feasible. Alternatively, one could assume that the skyrmion has little influence on the self-consistent potential and instead calculate the potential only for the ferromagnetic state, allowing for much higher accuracy regarding the aforementioned numerical parameters. To validate this choice, I calculated the energy dependent transmission through the V/Fe/MgO(3)/Cu structure with an analytical skyrmion structure twice, using both a potential with very high numerical precision and one with weaker numerical parameters. In both cases, the potential is calculated for the ferromagnetic structure with out-of-plane magnetization.

Third, I calculated the self-consistent potential of the 5x5 cell, including the simulated skyrmion structure, where the magnetization direction was applied to all layers, and used it to calculate the energy dependent transmission through the same V/Fe/MgO(3)/Cu structure. The results, displayed in figure B.3, clearly indicate that the weak numerical parameters, for which a self-consistent potential calculation including the skyrmion structure were practically achievable at that time, led to very different results. The combined effect due to the self-consistent skyrmion potential, the application of the magnetization direction to all layers, and the use of the different skyrmion type, which is summarized in the difference between the orange and blue line, is negligible compared to the effect of the weak numerical parameters. While it might be possible to find a way to tune the parameters to improve the accuracy of the self-consistent potential, including the skyrmion without becoming computationally unfeasible, I decided to go with the more accurate potential of the ferromagnetic structure. This approach was used in all other calculations in this work.

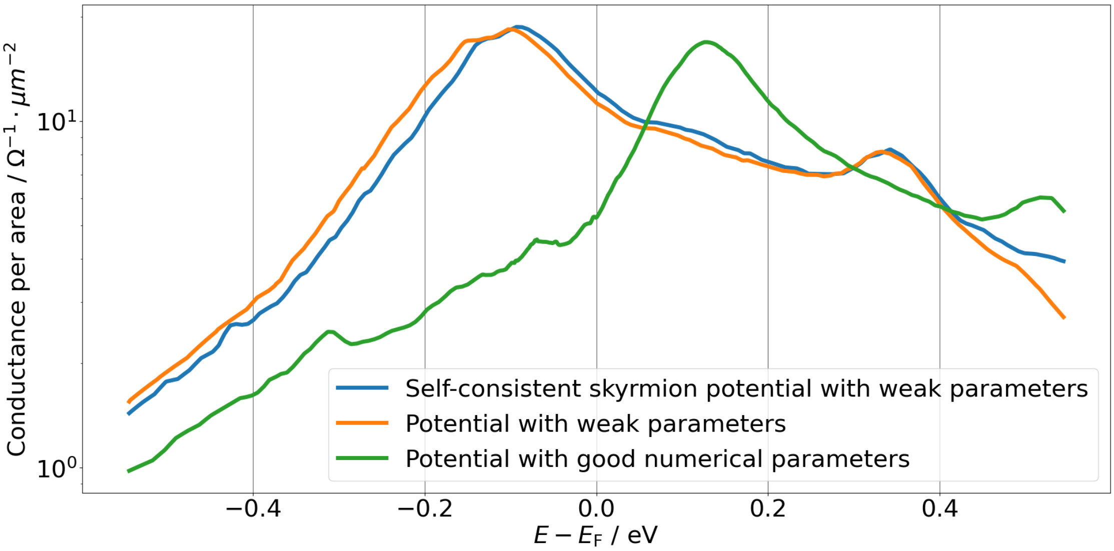

Figure B.3: The energy dependent transmission through the V/Fe/MgO(3)/Cu structure with an analytical skyrmion structure with a potential, calculated with very high numerical precision (green). The same calculation again with an analytical skyrmion, but based on a potential, which was calculated with weak numerical parameters (orange). With a potential, where the simulated skyrmion structure was included in the self-consistency calculation, and where the magnetization direction was applied to all layers in the V/Fe/MgO(3)/Cu structure (blue).

Bibliography

[1] D. Song, J. Nowak, R. Larson, P. Kolbo, and R. Chellew, "Demonstrating a tunneling magneto-resistive read head," *IEEE transactions on magnetics* **36** no. 5, (2000) 2545–2548.

[2] I. Žutić, J. Fabian, and S. D. Sarma, "Spintronics: Fundamentals and applications," *Reviews of modern physics* **76** no. 2, (2004) 323.

[3] Y. Tchoe and J. H. Han, "Skyrmion generation by current," *Physical Review B—Condensed Matter and Materials Physics* **85** no. 17, (2012) 174416.

[4] T. H. R. Skyrme, "A unified field theory of mesons and baryons," *Nuclear Physics* **31** (1962) 556–569.

[5] S. Mühlbauer, B. Binz, F. Jonietz, C. Pfleiderer, A. Rosch, A. Neubauer, R. Georgii, and P. Böni, "Skyrmion lattice in a chiral magnet," *Science* **323** no. 5916, (2009) 915–919.

[6] S. Heinze, K. Von Bergmann, M. Menzel, J. Brede, A. Kubetzka, R. Wiesendanger, G. Bihlmayer, and S. Blügel, "Spontaneous atomic-scale magnetic skyrmion lattice in two dimensions," *nature physics* **7** no. 9, (2011) 713–718.

[7] X. Yu, Y. Onose, N. Kanazawa, J. H. Park, J. Han, Y. Matsui, N. Nagaosa, and Y. Tokura, "Real-space observation of a two-dimensional skyrmion crystal," *Nature* **465** no. 7300, (2010) 901–904.

[8] R. Tomasello, E. Martinez, R. Zivieri, L. Torres, M. Carpentieri, and G. Finocchio, "A strategy for the design of skyrmion racetrack memories," *Scientific reports* **4** (2014) 6784.

[9] S. S. Parkin, M. Hayashi, and L. Thomas, "Magnetic domain-wall racetrack memory," *Science* **320** no. 5873, (2008) 190–194.

[10] K. Baker, "A review of magnetic bubble memories and their applications," *Radio and Electronic Engineer* **51** no. 3, (1981) 105–115.

[11] A. Fert, V. Cros, and J. Sampaio, “Skyrmions on the track,” *Nature nanotechnology* **8** no. 3, (2013) 152.

[12] S. Wang, J. Tang, W. Wang, L. Kong, M. Tian, and H. Du, “Electrical Detection of Magnetic Skyrmions,” *Journal of Low Temperature Physics* (2019) 1–16.

[13] G. Finocchio, F. Büttner, R. Tomasello, M. Carpentieri, and M. Kläui, “Magnetic skyrmions: from fundamental to applications,” *Journal of Physics D: Applied Physics* **49** no. 42, (2016) 423001.

[14] X. Zhang, M. Ezawa, and Y. Zhou, “Magnetic skyrmion logic gates: conversion, duplication and merging of skyrmions,” *Scientific reports* **5** no. 1, (2015) 9400.

[15] S. Li, W. Kang, Y. Huang, X. Zhang, Y. Zhou, and W. Zhao, “Magnetic skyrmion-based artificial neuron device,” *Nanotechnology* **28** no. 31, (2017) 31LT01.

[16] K. M. Song, J.-S. Jeong, *et al.*, “Skyrmion-based artificial synapses for neuromorphic computing,” *Nature Electronics* **3** no. 3, (2020) 148–155.

[17] C. Psaroudaki and C. Panagopoulos, “Skyrmion qubits: A new class of quantum logic elements based on nanoscale magnetization,” *Physical Review Letters* **127** no. 6, (2021) 067201.

[18] J. Xia, X. Zhang, X. Liu, Y. Zhou, and M. Ezawa, “Universal quantum computation based on nanoscale skyrmion helicity qubits in frustrated magnets,” *Physical Review Letters* **130** no. 10, (2023) 106701.

[19] G. Finocchio, M. Ricci, R. Tomasello, A. Giordano, M. Lanuzza, V. Puliafito, P. Burrascano, B. Azzerboni, and M. Carpentieri, “Skyrmion based microwave detectors and harvesting,” *Applied Physics Letters* **107** no. 26, (2015) .

[20] J. S. Moodera, L. R. Kinder, T. M. Wong, and R. Meservey, “Large magnetoresistance at room temperature in ferromagnetic thin film tunnel junctions,” *Physical review letters* **74** no. 16, (1995) 3273.

[21] T. Miyazaki and N. Tezuka, “Giant magnetic tunneling effect in Fe/Al2O3/Fe junction,” *Journal of magnetism and magnetic materials* **139** no. 3, (1995) L231–L234.

[22] W. H. Butler, “Tunneling magnetoresistance from a symmetry filtering effect,” *Science and Technology of Advanced Materials* **9** no. 1, (2008) 014106.

[23] Y. Guang, L. Zhang, *et al.*, “Electrical detection of magnetic skyrmions in a magnetic tunnel junction,” *Advanced Electronic Materials* **9** no. 1, (2023) 2200570.

[24] N. Penthorn, X. Hao, Z. Wang, Y. Huai, and H. Jiang, “Experimental observation of single skyrmion signatures in a magnetic tunnel junction,” *Physical Review Letters* **122** no. 25, (2019) 257201.

[25] C. Gould, C. Rüster, T. Jungwirth, E. Girgis, G. Schott, R. Giraud, K. Brunner, G. Schmidt, and L. Molenkamp, “Tunneling anisotropic magnetoresistance: a spin-valve-like tunnel magnetoresistance using a single magnetic layer,” *Physical review letters* **93** no. 11, (2004) 117203.

[26] B. Binz and A. Vishwanath, “Chirality induced anomalous-Hall effect in helical spin crystals,” *Physica B: Condensed Matter* **403** no. 5-9, (2008) 1336–1340.

[27] A. Neubauer, C. Pfleiderer, B. Binz, A. Rosch, R. Ritz, P. Niklowitz, and P. Böni, “Topological Hall effect in the A phase of MnSi,” *Physical review letters* **102** no. 18, (2009) 186602.

[28] G. Kimbell, C. Kim, W. Wu, M. Cuoco, and J. W. Robinson, “Challenges in identifying chiral spin textures via the topological Hall effect,” *Communications Materials* **3** no. 1, (2022) 19.

[29] B. Göbel, A. Mook, J. Henk, I. Mertig, and O. A. Tretiakov, “Magnetic bimerons as skyrmion analogues in in-plane magnets,” *Physical review B* **99** no. 6, (2019) 060407.

[30] H. Chen, W. Bouckaert, and S. A. Majetich, “Tunnel magnetoresistance detection of skyrmions,” *Journal of Magnetism and Magnetic Materials* **541** (2022) 168552.

[31] X. Zhang, G. Zhao, H. Fangohr, J. P. Liu, W. Xia, J. Xia, and F. Morvan, “Skyrmion-skyrmion and skyrmion-edge repulsions in skyrmion-based racetrack memory,” *Scientific reports* **5** no. 1, (2015) 7643.

[32] K. Zeissler, S. Finizio, *et al.*, “Discrete Hall resistivity contribution from Néel skyrmions in multilayer nanodiscs,” *Nature Nanotechnology* **13** no. 12, (2018) 1161–1166.

[33] D. Maccariello, W. Legrand, N. Reyren, K. Garcia, K. Bouzehouane, S. Collin, V. Cros, and A. Fert, “Electrical detection of single magnetic skyrmions in metallic multilayers at room temperature,” *Nature nanotechnology* **13** no. 3, (2018) 233–237.

[34] H. Lu, J. Robertson, and H. Naganuma, “Comparison of hexagonal boron nitride and MgO tunnel barriers in Fe, Co magnetic tunnel junctions,” *Applied Physics Reviews* **8** no. 3, (2021) .

[35] C. Hanneken, F. Otte, A. Kubetzka, B. Dupé, N. Romming, K. Von Bergmann, R. Wiesendanger, and S. Heinze, “Electrical detection of magnetic skyrmions by

tunnelling non-collinear magnetoresistance," *Nature nanotechnology* **10** no. 12, (2015) 1039.

[36] D. M. Crum, M. Bouhassoune, J. Bouaziz, B. Schweflinghaus, S. Blügel, and S. Lounis, "Perpendicular reading of single confined magnetic skyrmions," *Nature communications* **6** (2015) 8541.

[37] M. Walter, J. Walowski, *et al.*, "Seebeck effect in magnetic tunnel junctions," *Nature materials* **10** no. 10, (2011) 742.

[38] J. Zang, M. Mostovoy, J. H. Han, and N. Nagaosa, "Dynamics of skyrmion crystals in metallic thin films," *Physical review letters* **107** no. 13, (2011) 136804.

[39] G. Chen, "Skyrmion hall effect," *Nature Physics* **13** no. 2, (2017) 112–113.

[40] T. Jungwirth, X. Marti, P. Wadley, and J. Wunderlich, "Antiferromagnetic spintronics," *Nature nanotechnology* **11** no. 3, (2016) 231–241.

[41] V. Baltz, A. Manchon, M. Tsoi, T. Moriyama, T. Ono, and Y. Tserkovnyak, "Antiferromagnetic spintronics," *Reviews of Modern Physics* **90** no. 1, (2018) 015005.

[42] M. N. Potkina, I. S. Lobanov, H. Jónsson, and V. M. Uzdin, "Skyrmions in antiferromagnets: Thermal stability and the effect of external field and impurities," *Journal of Applied Physics* **127** no. 21, (2020) .

[43] J. Barker and O. A. Tretiakov, "Static and dynamical properties of antiferromagnetic skyrmions in the presence of applied current and temperature," *Physical review letters* **116** no. 14, (2016) 147203.

[44] S. Blügel, B. Drittler, R. Zeller, and P. Dederichs, "Magnetic properties of 3 d transition metal monolayers on metal substrates," *Applied Physics A* **49** no. 6, (1989) 547–562.

[45] I. Lima Fernandes, S. Blügel, and S. Lounis, "Spin-orbit enabled all-electrical readout of chiral spin-textures," *Nature communications* **13** no. 1, (2022) 1–10.

[46] W. Kohn, "Nobel Lecture: Electronic structure of matter—wave functions and density functionals," *Reviews of Modern Physics* **71** no. 5, (1999) 1253.

[47] P. Hohenberg and W. Kohn, "Inhomogeneous electron gas," *Physical review* **136** no. 3B, (1964) B864.

[48] W. Kohn and L. J. Sham, "Self-consistent equations including exchange and correlation effects," *Physical review* **140** no. 4A, (1965) A1133.

[49] M. Born and W. Heisenberg, "Zur quantentheorie der molekeln," *Original Scientific Papers Wissenschaftliche Originalarbeiten* (1985) 216–246.

[50] D. R. Hartree, "The wave mechanics of an atom with a non-Coulomb central field. Part I. Theory and methods," in *Mathematical Proceedings of the Cambridge Philosophical Society*, vol. 24, pp. 89–110, Cambridge university press. 1928.

[51] V. Fock, "Näherungsmethode zur Lösung des quantenmechanischen Mehrkörperproblems," *Zeitschrift für Physik* **61** (1930) 126–148.

[52] D. R. Hartree and W. Hartree, "Self-consistent field, with exchange, for beryllium," *Proceedings of the Royal Society of London. Series A-Mathematical and Physical Sciences* **150** no. 869, (1935) 9–33.

[53] J. C. Slater, "A simplification of the Hartree-Fock method," *Physical review* **81** no. 3, (1951) 385.

[54] S. H. Vosko, L. Wilk, and M. Nusair, "Accurate spin-dependent electron liquid correlation energies for local spin density calculations: a critical analysis," *Canadian Journal of physics* **58** no. 8, (1980) 1200–1211.

[55] U. Von Barth and L. Hedin, "A local exchange-correlation potential for the spin polarized case. i," *Journal of Physics C: Solid State Physics* **5** no. 13, (1972) 1629.

[56] L. Hedin and B. I. Lundqvist, "Explicit local exchange-correlation potentials," *Journal of Physics C: Solid state physics* **4** no. 14, (1971) 2064.

[57] J. P. Perdew and Y. Wang, "Accurate and simple analytic representation of the electron-gas correlation energy," *Physical review B* **45** no. 23, (1992) 13244.

[58] J. P. Perdew and W. Yue, "Accurate and simple density functional for the electronic exchange energy: Generalized gradient approximation," *Physical review B* **33** no. 12, (1986) 8800.

[59] J. P. Perdew, "Generalized gradient approximations for exchange and correlation: A look backward and forward," *Physica B: Condensed Matter* **172** no. 1-2, (1991) 1–6.

[60] Y. Wang and J. P. Perdew, "Spin scaling of the electron-gas correlation energy in the high-density limit," *Physical Review B* **43** no. 11, (1991) 8911.

[61] J. Korringa, "On the calculation of the energy of a Bloch wave in a metal," *Physica* **13** no. 6-7, (1947) 392–400.

[62] W. Kohn and N. Rostoker, "Solution of the Schrödinger equation in periodic lattices with an application to metallic lithium," *Physical Review* **94** no. 5, (1954) 1111.

[63] J. Korringa, “Early history of multiple scattering theory for ordered systems,” *Physics Reports* **238** no. 6, (1994) 341–360.

[64] H. Ebert, D. Koedderitzsch, and J. Minar, “Calculating condensed matter properties using the KKR-Green’s function method—recent developments and applications,” *Reports on Progress in Physics* **74** no. 9, (2011) 096501.

[65] J. Zabloudil, R. Hammerling, P. Weinberger, and L. Szunyogh, *Electron Scattering in Solid Matter: a theoretical and computational treatise*. Springer, 2005.

[66] I. Mertig, E. Mrosan, and P. Ziesche, *Multiple scattering theory of point defects in metals. Electronic properties*. 1987.

[67] I. Grattan-Guinness, “George Green, an essay on the mathematical analysis of electricity and magnetism (1828),” in *Landmark Writings in Western Mathematics 1640-1940*, pp. 403–411. Elsevier, 2005.

[68] S. Datta, *Electronic transport in mesoscopic systems*. Cambridge university press, 1997.

[69] M. Czerner, *Beiträge zur Theorie des Elektronentransports in Systemen mit nichtkollinearer magnetischer Ordnung*. PhD thesis, Halle (Saale), Martin-Luther-Universität Halle-Wittenberg, Diss., 2009, 2009.

[70] B. A. Lippmann and J. Schwinger, “Variational principles for scattering processes. I,” *Physical Review* **79** no. 3, (1950) 469.

[71] O. Andersen and R. Kasowski, “Electronic states as linear combinations of muffin-tin orbitals,” *Physical Review B* **4** no. 4, (1971) 1064.

[72] O. K. Andersen, “Linear methods in band theory,” *Physical Review B* **12** no. 8, (1975) 3060.

[73] L. Szunyogh, “Introduction to multiple scattering theory,” `http://newton.phy.bme.hu/~szunyogh/Elszerk/Kkr-slides.pdf`.

[74] R. Zeller, M. Asato, T. Hoshino, J. Zabloudil, P. Weinberger, and P. Dederichs, “Total-energy calculations with the full-potential KKR method,” *Philosophical Magazine B* **78** no. 5-6, (1998) 417–422.

[75] M. Asato, A. Settels, T. Hoshino, T. Asada, S. Blügel, R. Zeller, and P. Dederichs, “Full-potential KKR calculations for metals and semiconductors,” *Physical Review B* **60** no. 8, (1999) 5202.

[76] R. Zeller, P. Dederichs, B. Újfalussy, L. Szunyogh, and P. Weinberger, "Theory and convergence properties of the screened Korringa-Kohn-Rostoker method," *Physical Review B* **52** no. 12, (1995) 8807.

[77] R. Zeller, "Evaluation of the screened Korringa-Kohn-Rostoker method for accurate and large-scale electronic-structure calculations," *Physical Review B* **55** no. 15, (1997) 9400.

[78] P. Zahn, *Screened Korringa-Kohn-Rostoker-Methode für Vielfachschichten.* PhD thesis, Technische Universität Dresden, Dresden, 1998. `https://nbn-resolving.org/urn:nbn:de:swb:14-1119864864984-42479`.

[79] K. Wildberger, "Tight-Binding-Korringa-Kohn-Rostoker-Methode und Grenzflächenreflektivität in magnetischen Schichtsystemen," tech. rep., Publikationen vor 2000, 1997.

[80] R. Zeller, "Conceptual and computational advances in multiple-scattering electronic-structure calculations," *Computational materials science* **10** no. 1-4, (1998) 373–380.

[81] T. Matsubara, "A new approach to quantum-statistical mechanics," *Progress of theoretical physics* **14** no. 4, (1955) 351–378.

[82] N. D. Mermin, "Thermal properties of the inhomogeneous electron gas," *Physical Review* **137** no. 5A, (1965) A1441.

[83] K. Wildberger, P. Lang, R. Zeller, and P. Dederichs, "Fermi-Dirac distribution in ab initio Green's-function calculations," *Physical Review B* **52** no. 15, (1995) 11502.

[84] S. Achilles, M. Czerner, J. Henk, I. Mertig, and C. Heiliger, "Nonequilibrium Green's functions and Korringa-Kohn-Rostoker method: Open planar junctions," *Physical Review B* **88** no. 12, (2013) 125411.

[85] C. Heiliger, M. Czerner, B. Y. Yavorsky, I. Mertig, and M. D. Stiles, "Implementation of a nonequilibrium Green's function method to calculate spin-transfer torque," *Journal of Applied Physics* **103** no. 7, (2008) 07A709.

[86] C. Franz, M. Czerner, and C. Heiliger, "Implementation of non-equilibrium vertex corrections in KKR: transport through disordered layers," *Journal of Physics: Condensed Matter* **25** no. 42, (2013) 425301.

[87] A. N. Chantis, K. D. Belashchenko, D. L. Smith, E. Y. Tsymbal, M. van Schilfgaarde, and R. C. Albers, "Reversal of spin polarization in Fe/GaAs (001) driven by resonant surface states: First-principles calculations," *Physical review letters* **99** no. 19, (2007) 196603.

[88] P. Bose, A. Ernst, I. Mertig, and J. Henk, "Large reduction of the magnetoresistance in Fe/MgO/Fe tunnel junctions due to small oxygen concentrations at a single FeO interface layer: A first-principles study," *Physical Review B* **78** no. 9, (2008) 092403.

[89] V. Drchal, J. Kudrnovskỳ, P. Bruno, P. Dederichs, I. Turek, and P. Weinberger, "Electron transport in magnetic multilayers: Effect of disorder," *Physical Review B* **65** no. 21, (2002) 214414.

[90] M. Czerner, private communication, 2018.

[91] C. E. Mahr, M. Czerner, and C. Heiliger, "Implementation of a method for calculating temperature-dependent resistivities in the KKR formalism," *Physical Review B* **96** no. 16, (2017) 165121.

[92] M. Julliere, "Tunneling between ferromagnetic films," *Physics letters A* **54** no. 3, (1975) 225–226.

[93] C. Heiliger, P. Zahn, and I. Mertig, "Microscopic origin of magnetoresistance," *Materials Today* **9** no. 11, (2006) 46–54.

[94] S. Parkin, K. Roche, *et al.*, "Exchange-biased magnetic tunnel junctions and application to nonvolatile magnetic random access memory," *Journal of Applied Physics* **85** no. 8, (1999) 5828–5833.

[95] R. Sousa, J. Sun, V. Soares, P. Freitas, A. Kling, M. Da Silva, and J. Soares, "Large tunneling magnetoresistance enhancement by thermal anneal," *Applied physics letters* **73** no. 22, (1998) 3288–3290.

[96] W. Butler, X.-G. Zhang, T. Schulthess, and J. MacLaren, "Spin-dependent tunneling conductance of Fe| MgO| Fe sandwiches," *Physical Review B* **63** no. 5, (2001) 054416.

[97] M. Gradhand, C. Heiliger, P. Zahn, and I. Mertig, "Tunneling magnetoresistance with amorphous electrodes," *Phys. Rev. B* **77** (Apr, 2008) 134403.

[98] A. Chantis, K. Belashchenko, E. Tsymbal, and M. van Schilfgaarde, "Tunneling anisotropic magnetoresistance driven by resonant surface states," in *APS March Meeting Abstracts*, pp. P15–008. 2007.

[99] Z. Quan, F. Zhang, Z. Yan, H. Liu, W. Zhang, B. Fang, G. Zhou, Z. Zeng, and X. Xu, "Experimental observation of large tunneling anisotropic magnetoresistance in a magnetic tunnel junction without heavy metals," *Applied Surface Science* **526** (2020) 146716.

[100] S. Blügel, T. Schäpers, Y. Ando, and Y. Mokrousov, *Topological matter-topological insulators, skyrmions and majoranas.* 2017.

[101] A. Aharoni *et al.*, *Introduction to the Theory of Ferromagnetism*, vol. 109. Clarendon Press, 2000.

[102] M. W. Hanna, "Magnetism, A Treatise on Modern Theory and Materials. Volume I. Edited by George T. Rado and Harry Suhl," *Inorganic Chemistry* **4** no. 9, (1965) 1376–1376.

[103] W. Heisenberg, "Zur Theorie des Ferromagnetismus, 1928," *Z. Phys* **49** 619.

[104] T. Moriya, "Anisotropic superexchange interaction and weak ferromagnetism," *Physical review* **120** no. 1, (1960) 91.

[105] T. Moriya, "New mechanism of anisotropic superexchange interaction," *Physical Review Letters* **4** no. 5, (1960) 228.

[106] I. Dzyaloshinsky, "A thermodynamic theory of "weak" ferromagnetism of antiferromagnetics," *Journal of physics and chemistry of solids* **4** no. 4, (1958) 241–255.

[107] D. Krause, "Über die magnetische Anisotropieenergie kubischer Kristalle," *physica status solidi (b)* **6** no. 1, (1964) 125–134.

[108] B. D. Cullity and C. D. Graham, *Introduction to magnetic materials.* John Wiley & Sons, 2009.

[109] C. Robert and O. Handley, "Modern magnetic materials: principles and applications," *Ed. John Wiley & Sons, Inc., New York* (2000) 184–188.

[110] T. Maruyama, Y. Shiota, *et al.*, "Large voltage-induced magnetic anisotropy change in a few atomic layers of iron," *Nature nanotechnology* **4** no. 3, (2009) 158–161.

[111] J. Zhu, J. Katine, *et al.*, "Voltage-induced ferromagnetic resonance in magnetic tunnel junctions," *Physical review letters* **108** no. 19, (2012) 197203.

[112] X. Wang, W. L. Gan, J. Martinez, F. N. Tan, M. Jalil, and W. S. Lew, "Efficient skyrmion transport mediated by a voltage controlled magnetic anisotropy gradient," *Nanoscale* **10** no. 2, (2018) 733–740.

[113] W. Legrand, D. Maccariello, F. Ajejas, S. Collin, A. Vecchiola, K. Bouzehouane, N. Reyren, V. Cros, and A. Fert, "Room-temperature stabilization of antiferromagnetic skyrmions in synthetic antiferromagnets," *Nature materials* **19** no. 1, (2020) 34–42.

[114] B. D. Cullity and C. D. Graham, *Introduction to magnetic materials.* John Wiley & Sons, 2009.

[115] C. Denker, S. Nielsen, E. Lage, M. Römer-Stumm, H. Heyen, Y. Junk, J. Walowski, K. Waldorf, M. Münzenberg, and J. McCord, "Size and density control of skyrmions with picometer CoFeB thickness variations—observation of zero-field skyrmions and skyrmion merging," *Journal of Physics D: Applied Physics* **56** no. 49, (2023) 495302.

[116] A. Butenko, A. Leonov, U. Rößler, and A. Bogdanov, "Stabilization of skyrmion textures by uniaxial distortions in noncentrosymmetric cubic helimagnets," *Physical Review B* **82** no. 5, (2010) 052403.

[117] J. Gallagher, K. Meng, J. Brangham, H. Wang, B. Esser, D. McComb, and F. Yang, "Robust zero-field skyrmion formation in FeGe epitaxial thin films," *Physical review letters* **118** no. 2, (2017) 027201.

[118] A. Kartsev, M. Augustin, R. F. Evans, K. S. Novoselov, and E. J. Santos, "Biquadratic exchange interactions in two-dimensional magnets," *npj Computational Materials* **6** no. 1, (2020) 150.

[119] R. Singer, F. Dietermann, and M. Fähnle, "Spin Interactions in bcc and fcc Fe beyond the Heisenberg Model," *Physical Review Letters* **107** no. 1, (2011) 017204.

[120] L. Landau and E. Lifshitz, "On the theory of the dispersion of magnetic permeability in ferromagnetic bodies," *Phys. Z. Sowjetunion* **8** no. 153, (1935) 101–114.

[121] W. F. Brown, *Magnetostatic principles in ferromagnetism.* North-Holland Publishing Company, 1962.

[122] T. L. Gilbert, "A Lagrangian formulation of the gyromagnetic equation of the magnetization field," *Phys. Rev.* **100** (1955) 1243.

[123] J.-V. Kim and J. Mulkers, "On quantifying the topological charge in micromagnetics using a lattice-based approach," *IOP SciNotes* **1** no. 2, (2020) 025211.

[124] S. Kandukuri, V. S. N. Murthy, and P. Thiruvikraman, "Isolated skyrmion, skyrmion lattice and antiskyrmion lattice creation through magnetization reversal in Co/Pd nanostructure," *Scientific Reports* **11** no. 1, (2021) 18945.

[125] X. Zhang, Y. Zhou, K. M. Song, T.-E. Park, J. Xia, M. Ezawa, X. Liu, W. Zhao, G. Zhao, and S. Woo, "Skyrmion-electronics: writing, deleting, reading and

processing magnetic skyrmions toward spintronic applications," *Journal of Physics: Condensed Matter* **32** no. 14, (2020) 143001.

[126] N. Nagaosa and Y. Tokura, "Topological properties and dynamics of magnetic skyrmions," *Nature nanotechnology* **8** no. 12, (2013) 899.

[127] X. Zhang, Y. Zhou, and M. Ezawa, "Antiferromagnetic skyrmion: stability, creation and manipulation," *Scientific reports* **6** no. 1, (2016) 24795.

[128] A. K. Nayak, V. Kumar, T. Ma, P. Werner, E. Pippel, R. Sahoo, F. Damay, U. K. Rößler, C. Felser, and S. S. Parkin, "Magnetic antiskyrmions above room temperature in tetragonal Heusler materials," *Nature* **548** no. 7669, (2017) 561–566.

[129] Z. Wang, Y. Su, S.-Z. Lin, and C. D. Batista, "Meron, skyrmion, and vortex crystals in centrosymmetric tetragonal magnets," *Physical Review B* **103** no. 10, (2021) 104408.

[130] Y. Kharkov, O. Sushkov, and M. Mostovoy, "Bound states of skyrmions and merons near the Lifshitz point," *Physical review letters* **119** no. 20, (2017) 207201.

[131] C. G. Allan Jr, R. Dashen, and D. J. Gross, "A mechanism for quark confinement," *Physics Letters B* **66** no. 4, (1977) 375–381.

[132] M. Ezawa, "Compact merons and skyrmions in thin chiral magnetic films," *Physical Review B* **83** no. 10, (2011) 100408.

[133] B. Göbel, I. Mertig, and O. A. Tretiakov, "Beyond skyrmions: Review and perspectives of alternative magnetic quasiparticles," *Physics Reports* **895** (2021) 1–28.

[134] M. Hoffmann, B. Zimmermann, G. P. Müller, D. Schürhoff, N. S. Kiselev, C. Melcher, and S. Blügel, "Antiskyrmions stabilized at interfaces by anisotropic Dzyaloshinskii-Moriya interactions," *Nature communications* **8** no. 1, (2017) 308.

[135] W. Jiang, G. Chen, K. Liu, J. Zang, S. G. Te Velthuis, and A. Hoffmann, "Skyrmions in magnetic multilayers," *Physics Reports* **704** (2017) 1–49.

[136] S. Mühlbauer, B. Binz, F. Jonietz, C. Pfleiderer, A. Rosch, A. Neubauer, R. Georgii, and P. Böni, "Skyrmion lattice in a chiral magnet," *Science* **323** no. 5916, (2009) 915–919.

[137] A. Crépieux and C. Lacroix, "Dzyaloshinsky–Moriya interactions induced by symmetry breaking at a surface," *Journal of magnetism and magnetic materials* **182** no. 3, (1998) 341–349.

[138] S. Huang, C. Zhou, G. Chen, H. Shen, A. K. Schmid, K. Liu, and Y. Wu, "Stabilization and current-induced motion of antiskyrmion in the presence of anisotropic Dzyaloshinskii-Moriya interaction," *Physical Review B* **96** no. 14, (2017) 144412.

[139] T. Wang, Y. Li, K. J. Lee, J. Cho, D. Kim, S. Noh, and Y. Kim, "Influence of interface state in Fe/MgO/Fe magnetic tunnel junction system: C modified interfaces—a first principle study," *Journal of Applied Physics* **109** no. 8, (2011) 083714.

[140] X. Feng, O. Bengone, M. Alouani, I. Rungger, and S. Sanvito, "Interface and transport properties of Fe/V/MgO/Fe and Fe/V/Fe/MgO/Fe magnetic tunneling junctions," *Physical Review B* **79** no. 21, (2009) 214432.

[141] M. Czerner and C. Heiliger, "Influence of interface termination on the magneto-Seebeck effect in MgO based tunnel junctions," *Journal of Applied Physics* **111** no. 7, (2012) 07C511.

[142] M. Khan, J. Henk, and P. Bruno, "Anisotropic magnetoresistance in Fe/MgO/Fe tunnel junctions," *Journal of Physics: Condensed Matter* **20** no. 15, (2008) 155208.

[143] L. Wang, Y. Ga, Q. Cui, P. Li, J. Liang, Y. Zhou, S. Wang, and H. Yang, "Oxidization engineered Dzyaloshinskii-Moriya interaction and topological magnetism at Fe/MgO bilayers," *Physical Review B* **108** no. 21, (2023) 214404.

[144] H. Ebert, H. Freyer, A. Vernes, and G.-Y. Guo, "Manipulation of the spin-orbit coupling using the Dirac equation for spin-dependent potentials," *Physical Review B* **53** no. 12, (1996) 7721.

[145] M. Czerner, private communication, 2016.

[146] C. Heiliger, P. Zahn, B. Y. Yavorsky, and I. Mertig, "Influence of the interface structure on the bias dependence of tunneling magnetoresistance," *Physical Review B* **72** no. 18, (2005) 180406.

[147] S. Yuasa, T. Nagahama, A. Fukushima, Y. Suzuki, and K. Ando, "Giant room-temperature magnetoresistance in single-crystal Fe/MgO/Fe magnetic tunnel junctions," *Nature materials* **3** no. 12, (2004) 868–871.

[148] B. Hamad and J. Khalifeh, "On the magnetism of iron–vanadium systems," *Surface science* **470** no. 1-2, (2000) 149–154.

[149] N. Romming, A. Kubetzka, C. Hanneken, K. von Bergmann, and R. Wiesendanger, "Field-dependent size and shape of single magnetic skyrmions," *Physical review letters* **114** no. 17, (2015) 177203.

[150] R. Chen, X. Wang, *et al.*, “Large Dzyaloshinskii-Moriya interaction and room-temperature nanoscale skyrmions in CoFeB/MgO heterostructures,” *Cell Reports Physical Science* **2** no. 11, (2021) .

[151] S. S. Parkin, C. Kaiser, A. Panchula, P. M. Rice, B. Hughes, M. Samant, and S.-H. Yang, “Giant tunnelling magnetoresistance at room temperature with MgO (100) tunnel barriers,” *Nature materials* **3** no. 12, (2004) 862–867.

[152] D. D. Djayaprawira, K. Tsunekawa, M. Nagai, H. Maehara, S. Yamagata, N. Watanabe, S. Yuasa, Y. Suzuki, and K. Ando, “230% room-temperature magnetoresistance in CoFeB/ MgO/ CoFeB magnetic tunnel junctions,” *Applied physics letters* **86** no. 9, (2005) .

[153] A. Greer, A. Gray, *et al.*, “Observation of boron diffusion in an annealed Ta/CoFeB/MgO magnetic tunnel junction with standing-wave hard x-ray photoemission,” *Applied Physics Letters* **101** no. 20, (2012) .

[154] C. Franz, *An ab initio approach to spin transport in magnetic tunnel junctions with disorder.* PhD thesis, Justus-Liebig-Universität, Otto-Behaghel-Str. 8, 35394 Gießen, 2015. `http://geb.uni-giessen.de/geb/volltexte/2016/11984`.

[155] I. Martínez, P. Högl, *et al.*, “Interfacial spin-orbit coupling: new platform for superconducting spintronics,” *arXiv preprint arXiv:1812.08090* (2018) .

[156] N. Romming, A. Kubetzka, C. Hanneken, K. von Bergmann, and R. Wiesendanger, “Field-dependent size and shape of single magnetic skyrmions,” *Physical review letters* **114** no. 17, (2015) 177203.

[157] P.-J. Zermatten, G. Gaudin, G. Maris, M. Miron, A. Schuhl, C. Tiusan, F. Greullet, and M. Hehn, “Experimental evidence of interface resonance states in single-crystal magnetic tunnel junctions,” *Physical Review B* **78** no. 3, (2008) 033301.

[158] F. Himpsel, “Fe on Au (100): Quantum-well states down to a monolayer,” *Physical Review B* **44** no. 11, (1991) 5966.

[159] S. Chandrashekhar Koli, H. Zhou, J. Zhou, B. Dupé, and W. Zhao, “Impact of Spin-Orbit Coupling on Quantum Transport in Magnetic Tunnel Junction with an anti-ferromagnetic Capping Layer,” *arXiv e-prints* (2021) arXiv–2109.

[160] S. Miwa, J. Fujimoto, P. Risius, K. Nawaoka, M. Goto, and Y. Suzuki, “Strong bias effect on voltage-driven torque at epitaxial Fe-MgO interface,” *Physical Review X* **7** no. 3, (2017) 031018.

[161] M. K. Niranjan, C.-G. Duan, S. S. Jaswal, and E. Y. Tsymbal, "Electric field effect on magnetization at the Fe/MgO (001) interface," *Applied Physics Letters* **96** no. 22, (2010) .

[162] T.-C. Chiang, "Photoemission studies of quantum well states in thin films," *Surface Science Reports* **39** no. 7-8, (2000) 181–235.

[163] T. J. Seebeck, *Ueber den Magnetismus der galvanischen Kette*. 1822.

[164] H. C. Ørsted, "New experiments by Dr. Seebeck on electromagnetic effects," in *Annales de chimie et de physique*, vol. 22, pp. 199–201. 1823.

[165] M. Czerner, M. Bachmann, and C. Heiliger, "Spin caloritronics in magnetic tunnel junctions: Ab initio studies," *Physical Review B* **83** no. 13, (2011) 132405.

[166] C. Heiliger, C. Franz, and M. Czerner, "Ab initio studies of the tunneling magneto-Seebeck effect: Influence of magnetic material," *Physical Review B* **87** no. 22, (2013) 224412.

[167] U. Sivan and Y. Imry, "Multichannel Landauer formula for thermoelectric transport with application to thermopower near the mobility edge," *Physical review b* **33** no. 1, (1986) 551.

[168] N. Liebing, S. Serrano-Guisan, K. Rott, G. Reiss, J. Langer, B. Ocker, and H. Schumacher, "Tunneling magnetothermopower in magnetic tunnel junction nanopillars," *Physical Review Letters* **107** no. 17, (2011) 177201.

[169] T. Kuschel, M. Czerner, J. Walowski, A. Thomas, H. W. Schumacher, G. Reiss, C. Heiliger, and M. Münzenberg, "Tunnel magneto-Seebeck effect," *Journal of Physics D: Applied Physics* (2018) .

[170] L. Gravier, S. Serrano-Guisan, F. Reuse, and J.-P. Ansermet, "Thermodynamic description of heat and spin transport in magnetic nanostructures," *Physical Review B* **73** no. 2, (2006) 024419.

[171] Y. Apertet, H. Ouerdane, C. Goupil, and P. Lecoeur, "Thermoelectric internal current loops inside inhomogeneous systems," *Physical Review B—Condensed Matter and Materials Physics* **85** no. 3, (2012) 033201.

[172] D. Fu, A. Levander, R. Zhang, J. Ager III, and J. Wu, "Electrothermally driven current vortices in inhomogeneous bipolar semiconductors," *Physical Review B—Condensed Matter and Materials Physics* **84** no. 4, (2011) 045205.

[173] S. Masoumi, K. Zhussupbekov, N. Prochukhan, M. A. Morris, and A. Pakdel, "A comprehensive investigation into thermoelectric properties of PEDOT: PSS/Bi 0.5 Sb 1.5 Te 3 composites," *Journal of Materials Chemistry C* **12** no. 36, (2024) 14314–14329.

[174] H. S. Kousar, D. Srivastava, A. J. Karttunen, M. Karppinen, and G. C. Tewari, "p-type to n-type conductivity transition in thermoelectric CoSbS," *APL Materials* **10** no. 9, (2022) .

[175] K. Everschor-Sitte, J. Masell, R. M. Reeve, and M. Kläui, "Perspective: Magnetic skyrmions—Overview of recent progress in an active research field," *Journal of Applied Physics* **124** no. 24, (2018) 240901.

[176] C. Jin, C. Song, J. Wang, and Q. Liu, "Dynamics of antiferromagnetic skyrmion driven by the spin Hall effect," *Applied Physics Letters* **109** no. 18, (2016) 182404.

[177] S. Guan, Y. Liu, Z. Hou, D. Chen, Z. Fan, M. Zeng, X. Lu, X. Gao, M. Qin, and J.-M. Liu, "Optically controlled ultrafast dynamics of skyrmion in antiferromagnets," *Physical Review B* **107** no. 21, (2023) 214429.

[178] O. Amin, S. Poole, *et al.*, "Antiferromagnetic half-skyrmions electrically generated and controlled at room temperature," *Nature Nanotechnology* **18** no. 8, (2023) 849–853.

[179] X. Zhang, Y. Zhou, and M. Ezawa, "Magnetic bilayer-skyrmions without skyrmion Hall effect," *Nature communications* **7** no. 1, (2016) 1–7.

[180] H.-A. Zhou, T. Xu, H. Bai, and W. Jiang, "Efficient spintronics with fully compensated ferrimagnets," *Journal of the Physical Society of Japan* **90** no. 8, (2021) 081006.

[181] S. Woo, K. M. Song, *et al.*, "Current-driven dynamics and inhibition of the skyrmion Hall effect of ferrimagnetic skyrmions in GdFeCo films," *Nature communications* **9** no. 1, (2018) 959.

[182] P. M. Buhl, F. Freimuth, S. Blügel, and Y. Mokrousov, "Topological spin Hall effect in antiferromagnetic skyrmions," *physica status solidi (RRL)–Rapid Research Letters* **11** no. 4, (2017) 1700007.

[183] N. Djavid and R. K. Lake, "Electron transport through antiferromagnetic spin textures and skyrmions in a magnetic tunnel junction," *Physical Review B* **102** no. 2, (2020) 024419.

[184] H. Sadeghi, "Discriminating Seebeck sensing of molecules," *Physical Chemistry Chemical Physics* **21** no. 5, (2019) 2378–2381.

[185] K. Palotás, L. Rózsa, E. Simon, L. Udvardi, and L. Szunyogh, "Spin-polarized scanning tunneling microscopy characteristics of skyrmionic spin structures exhibiting various topologies," *Physical Review B* **96** no. 2, (2017) 024410.

[186] L. Camosi, N. Rougemaille, O. Fruchart, J. Vogel, and S. Rohart, "Micromagnetics of antiskyrmions in ultrathin films," *Physical Review B* **97** no. 13, (2018) 134404.

[187] B. Dupé, C. N. Kruse, T. Dornheim, and S. Heinze, "How to reveal metastable skyrmionic spin structures by spin-polarized scanning tunneling microscopy," *New Journal of Physics* **18** no. 5, (2016) 055015.

[188] L. Rózsa, K. Palotás, A. Deák, E. Simon, R. Yanes, L. Udvardi, L. Szunyogh, and U. Nowak, "Formation and stability of metastable skyrmionic spin structures with various topologies in an ultrathin film," *Physical Review B* **95** no. 9, (2017) 094423.

[189] S.-Z. Lin and S. Hayami, "Ginzburg-Landau theory for skyrmions in inversion-symmetric magnets with competing interactions," *Physical Review B* **93** no. 6, (2016) 064430.

[190] J. S. Moodera, L. R. Kinder, T. M. Wong, and R. Meservey, "Large magnetoresistance at room temperature in ferromagnetic thin film tunnel junctions," *Physical review letters* **74** no. 16, (1995) 3273.

[191] W. Legrand, N. Ronceray, N. Reyren, D. Maccariello, V. Cros, and A. Fert, "Modeling the shape of axisymmetric skyrmions in magnetic multilayers," *Physical Review Applied* **10** no. 6, (2018) 064042.

[192] A. N. Bogdanov and C. Panagopoulos, "Physical foundations and basic properties of magnetic skyrmions," *Nature Reviews Physics* **2** no. 9, (2020) 492–498.

[193] J. C. Slonczewski, "Conductance and exchange coupling of two ferromagnets separated by a tunneling barrier," *Physical Review B* **39** no. 10, (1989) 6995.

[194] C. Heiliger, C. Franz, and M. Czerner, "Ab initio studies of the tunneling magneto-Seebeck effect: Influence of magnetic material," *Physical Review B* **87** no. 22, (2013) 224412.

[195] A. Matos-Abiague and J. Fabian, "Anisotropic tunneling magnetoresistance and tunneling anisotropic magnetoresistance: Spin-orbit coupling in magnetic tunnel junctions," *Physical Review B* **79** no. 15, (2009) 155303.

[196] A. Kubetzka, C. Hanneken, R. Wiesendanger, and K. von Bergmann, "Impact of the skyrmion spin texture on magnetoresistance," *Physical Review B* **95** no. 10, (2017) 104433.

[197] I. Labrie-Boulay, T. B. Winkler, D. Franzen, A. Romanova, H. Fangohr, and M. Kläui, “Machine learning-based spin structure detection,” *arXiv preprint arXiv:2303.16905* (2023) .

[198] F. Meng, A. Yang, K. Du, F. Jia, X. Lei, T. Mei, L. Du, and X. Yuan, “Measuring the magnetic topological spin structure of light using an anapole probe,” *Light: Science & Applications* **11** no. 1, (2022) 287.

[199] L. Shen, J. Xia, X. Zhang, M. Ezawa, O. A. Tretiakov, X. Liu, G. Zhao, and Y. Zhou, “Current-induced dynamics and chaos of antiferromagnetic bimerons,” *Physical review letters* **124** no. 3, (2020) 037202.

[200] L. Shen, X. Li, J. Xia, L. Qiu, X. Zhang, O. A. Tretiakov, M. Ezawa, and Y. Zhou, “Dynamics of ferromagnetic bimerons driven by spin currents and magnetic fields,” *Physical review b* **102** no. 10, (2020) 104427.

[201] A. Aldarawsheh, I. L. Fernandes, S. Brinker, M. Sallermann, M. Abusaa, S. Blügel, and S. Lounis, “Emergence of zero-field non-synthetic single and interchained antiferromagnetic skyrmions in thin films,” *Nature Communications* **13** no. 1, (2022) 7369.

[202] A. Aldarawsheh, M. Sallermann, M. Abusaa, and S. Lounis, “Intrinsic Néel Antiferromagnetic Multimeronic Spin Textures in Ultrathin Films,” *The journal of physical chemistry letters* **14** no. 40, (2023) 8970–8978.

[203] R. Juge, N. Sisodia, *et al.*, “Skyrmions in synthetic antiferromagnets and their nucleation via electrical current and ultra-fast laser illumination,” *Nature Communications* **13** no. 1, (2022) 4807.

[204] A. Soumyanarayanan, M. Raju, *et al.*, “Tunable room-temperature magnetic skyrmions in Ir/Fe/Co/Pt multilayers,” *Nature materials* **16** no. 9, (2017) 898–904.

[205] D. Li, S. Haldar, and S. Heinze, “Proposal for all-electrical skyrmion detection in van der Waals tunnel junctions,” *Nano Letters* **24** no. 8, (2024) 2496–2502.

My Publications

[O1] J. F. Schäfer-Richarz, P. Risius, M. Czerner, and C. Heiliger, “Magnetic tunnel junctions: An efficient way for electrical skyrmion detection investigated by ab initio theory,” *Physical Review B* **100** no. 21, (2019) 214413.

Acknowledgement

First and foremost, I wish to express my gratitude to my supervisor Prof. Dr. Christian Heiliger for providing me the opportunity to explore solid state physics and writing this thesis in his group. He not only allowed me to attend a large variety of physics conferences where I had the chance to get to know several researchers from the field, he also allowed me to profit from his experience and great knowledge in countless discussions.

Special mention goes to my colleages and friends from the Institute for Theoretical Physics for the valuable discussions, the support, and the great times we had. Of these, I mostly want to thank Dr. Michael Czerner for his introduction to the KKR code, explaining to me the tricks and intricacies of the method, for providing the basic geometry of the barrier structure, his derivation and implementation of the code for decomposing specular and diffusive transport, and all the advice and insight I got from him in the many discussions we had. Next I want to mention Dr. Carsten Mahr, Dr. Marcel Giar, and Dr. Michael Feldmann who introduced me to the art of high performance computing and gave me a lot of valuable advice throughout the years. Furthermore, I want to mention Dr. Alex Fabian and Philipp Risius, with whom it was a great pleasure to share the office and who together with Dr. Juan M. Guerra were the best colleagues one could ask for.

Finally, I want to thank my wife without whose constant support I would have never been able to finish this work.

„Ich erkläre: Ich habe die vorgelegte Dissertation selbstständig und ohne unerlaubte fremde Hilfe und nur mit den Hilfen angefertigt, die ich in der Dissertation angegeben habe. Alle Textstellen, die wörtlich oder sinngemäß aus veröffentlichten Schriften entnommen sind, und alle Angaben, die auf mündlichen Auskünften beruhen, sind als solche kenntlich gemacht. Ich stimme einer evtl. Überprüfung meiner Dissertation durch eine Antiplagiat-Software zu. Bei den von mir durchgeführten und in der Dissertation erwähnten Untersuchungen habe ich die Grundsätze guter wissenschaftlicher Praxis, wie sie in der „Satzung der Justus-Liebig-Universität Gießen zur Sicherung guter wissenschaftlicher Praxis“ niedergelegt sind, eingehalten.“

Angaben zu auf künstlicher Intelligenz (KI) basierender Hilfen wie ChatGPT oder SchulKI von OpenAI oder Gemini von Google zur Erstellung meiner Dissertation (Zutreffendes angekreuzt):

☐ Ich habe bei der Erstellung dieses Textes kein KI-Tool verwendet.

☒ Ich habe ein KI-Tool in den folgenden Bereichen eingesetzt (Mehrfachnennungen möglich):

- ☐ Ideen finden, meine Kreativität anregen
- ☐ Verstehen von Konzepten, Recherche von Fakten und Definitionen
- ☒ Optimierung eines von mir verfassten Textes
- ☐ Erstellen ganzer Textpassagen nach meinen Vorgaben

Folgende KI-Tools habe ich verwendet, damit aufgeführte Teile meines Textes von dem Tool wie folgt profitiert haben:

Ich habe ChatGPT genutzt um den Text nach dessen Erstellung auf Rechtschreib- und Grammatikfehler zu prüfen. Ich habe keine Änderungsvorschläge ungeprüft übernommen.

Datum: ________________ Unterschrift: ____